

Copyright  
by  
Katheryne Elizabeth Wilson  
2012

**The Dissertation Committee for Katheryne Elizabeth Wilson Certifies that this is  
the approved version of the following dissertation:**

**Biomedical Photoacoustics Beyond Thermal Expansion:  
Photoacoustic nanoDroplets**

**Committee:**

---

Stanislav Emelianov, Supervisor

---

J. Brian Fowlkes

---

Mark Hamilton

---

Konstantin Sokolov

---

Robert Williams III

**Biomedical Photoacoustics Beyond Thermal Expansion:  
Photoacoustic nanoDroplets**

**by**

**Katheryne Elizabeth Wilson, B.S.BioE; M.S.E.**

**Dissertation**

Presented to the Faculty of the Graduate School of

The University of Texas at Austin

in Partial Fulfillment

of the Requirements

for the Degree of

**Doctor of Philosophy**

**The University of Texas at Austin**

**May 2012**

## **Dedication**

*To my parents, grandparents, and husband.*

*For their never-ending encouragement and incredible belief in me.*

## **Acknowledgements**

First and foremost, I must thank my advisor, Dr. Stanislav Emelianov. I have learned so much from him, including how to be an engineer. Stas allowed me the freedom in research to explore what was interesting to me, allowing my Ph.D. experience to be one of intrigue and discovery. Thank you for the years of mentorship, teaching, support, and quiet encouragement.

I would also like to thank my committee members, Dr. Brian Fowlkes, Dr. Mark Hamilton, Dr. Konstantin Sokolov, and Dr. Robert Williams III for being enthusiastic about my project, asking insightful questions, and providing helpful guidance to shape the overall directions of its research.

The people who make up the Ultrasound Imaging and Therapeutics Research Laboratory deserve my endless gratitude. First, my thanks go to Dr. Suengsoo Kim for developing a new image acquisition algorithm specifically for me, to Geoff Luke, Dr. Mohammad Mehrmohammadi, and Pieter Kruizinga for their hours of help with imaging setups, and to Dr. Wolfgang Frey, Dr. Salavat Agylamov, Dr. Andrei Karpouk, Dr. Iulia Graf, Dr. Srivalleesha Mallidi, Dr. Carolyn Bayer, Dr. Richard Bouchard, Dr. Bo Wang, Dr. Jimmy Su, Yun-Sheng Chen, Jason Cook, Alex Hannah, Sueng Yun Nam, Min Qu, Soon Joon Yoon, Doug Yeager, Ryan Truby, and Erika Cooley-Vreeland for numerous helpful conversations, discussions, listening to my many presentations, editing of papers and dissertation, and consumption of baked goods. Thank you to Tera Sherrard and Juili Kelvekar for their positive attitudes and superior helpfulness. Finally, a special thanks to Dr. Kimberly Homan for four years of mentorship, encouragement, support, friendship, and being a fantastic role model.

My undergraduate research assistants deserve special thanks for their hard work and patience over the years, and for allowing me to practice my mentorship skills on them. Miloš Marinković and Omer Mirza were my first undergrads joining me in summer, 2009. Besides being incredibly hard working and inquisitive, both have significantly helped me in this research. Miloš was still working for me for a year after he graduated even with his full time job. Omer researched with me for a total of nine semesters winning three Undergraduate Research Fellowships, bringing \$3,000 to the project. Without them, it would have taken potentially years longer to complete this work. Lance Hansen joined me in summer 2010 and was a pleasure to research with and brought joy to at times tedious research. Finally, Brock Webberman joined me in summer 2011. He has an uncanny ability to make gold nanorods, most likely due to his incredible precision and detail-oriented-ness which will serve him well in the future. To all of you guys, a big thank you!

So much gratitude goes towards my “behind the scenes” support system, my family. My parents (my mother, Beth, the perpetual academic, and my father, Dave, the pragmatic thinker), grandparents, aunt, and brother have been there for me since day one, and never let me forget it. Without them, I would have never had the strength or courage to overcome the challenges that have occurred in my life and persist. Also, to Dr. Chris Neils and Kerri Keiger, for without them, I would not have started my graduate education in the first place. Thanks for being on “Team Katie.” And finally, but certainly not least, I want to express my appreciation for my husband, Igor Karpov. He is my sage, my rock, and my best friend, and for his unconditional love and support, I am forever grateful.

# **Biomedical Photoacoustics Beyond Thermal Expansion: Photoacoustic nanoDroplets**

Katheryne Elizabeth Wilson, Ph. D.

The University of Texas at Austin, 2012

Supervisor: Stanislav Y. Emelianov

The recent increase in survival rates of most cancers is due to early detection greatly aided by medical imaging modalities. Combined ultrasound and photoacoustic imaging provide both morphological and functional/molecular information which can help to detect and diagnose cancer in its earliest stages. However, both modalities can benefit from the use of contrast agents. The objective of this thesis was to design, synthesize, and test a nano-sized, dual contrast agent for combined ultrasound and photoacoustic imaging named Photoacoustic nanoDroplets. This agent consists of liquid perfluorocarbon nanodroplets with encapsulated plasmonic nanoparticles. These dual contrast agents utilize optically triggered vaporization for photoacoustic signal generation, providing significantly higher signal amplitude than that from the traditionally used mechanism, thermal expansion. Upon pulsed laser irradiation, liquid perfluorocarbon undergoes a liquid-to-gas phase transition generating giant photoacoustic transients from these dwarf nanoparticles. Once triggered, the gaseous phase provides ultrasound contrast enhancement. Demonstrated in this work are the design, synthesis, characterization, and testing of Photoacoustic nanoDroplets in phantom and animal studies, and preliminary work into adapting these agents into targeted, drug delivery vehicles for simultaneous detection, diagnosis, and treatment of diseases.

## Table of Contents

List of Figures .....	xiii
Chapter 1: Introduction .....	1
1.1 Medical Imaging .....	2
1.2 Ultrasound Imaging .....	3
1.3 Ultrasound Contrast Agents .....	4
1.4 Photoacoustic Imaging .....	6
1.5 Photoacoustic Contrast Agents .....	9
1.6 Multifunctional Contrast Agents .....	12
1.7 Overall Research Goals and Dissertation Organization .....	13
1.8 References .....	14
Chapter 2: Design, Synthesis, and Characterization of Photoacoustic nanoDroplets (PAnDs) .....	22
2.1 PAnD Components .....	23
2.1.1 Perfluorocarbon Droplets .....	23
2.1.2 Shell .....	25
2.1.3 Plasmonic Nanoparticles .....	27
2.1.4 Targeting and Drug Encapsulation .....	28
2.2 PAnD Functionality .....	29
2.3 Potential Limitations .....	31
2.4 Final Synthesis Procedure .....	33
2.4.1 Materials .....	33
2.4.2 Synthesis of Gold Nanorods .....	34
2.4.3 Gold Nanorod Phase Transfer .....	34
2.4.4 PAnD Emulsion .....	35
2.4.5 Sizing and Sterilization .....	35
2.4.6 Characterization .....	36
2.4.6.1 Ultraviolet-visible spectrophotometry, Cryo-Transmission Electron Microscopy, and Dynamic Light Scattering .....	36

2.4.6.2 Ambient Temperature Stability.....	37
2.5 Results and Discussion .....	37
2.5.1 Synthesis .....	37
2.5.2 Ultraviolet-Visible Spectrophotometry, Cryo-Transmission Electron Microscopy, and Dynamic Light Scattering .....	39
2.5.3 Ambient Temperature Stability.....	41
2.6 Alternate Encapsulations and Modifications .....	42
2.6.1 Octadecylamine Phase Transfer.....	42
2.6.2 Perfluorodecanethiol Phase Transfer .....	44
2.7 Conclusions.....	46
2.8 References.....	46
Chapter 3: Preliminary Testing of Combined Ultrasound and Photoacoustic Contrast Enhancement.....	
3.1 Tissue Mimicking Phantoms.....	51
3.2 Photoacoustic and Ultrasound Imaging Systems.....	53
3.2.1 WP64 by WinProbe .....	53
3.2.2 Vevo2100 by Visual Sonics.....	54
3.2.3 Lasers .....	55
3.3 Data Analysis.....	55
3.3.1 Photoacoustic and Ultrasound Image Processing .....	56
3.3.2 Photoacoustic and Ultrasound Frame Reference .....	56
3.3.3 Frame Comparison and Graph Production .....	57
3.4 Methods.....	58
3.4.1 Characteristic Signal of Photoacoustic nanoDroplets.....	58
3.4.2 Selective Optical Triggering of Photoacoustic nanoDroplets.....	60
3.4.3 Photoacoustic nanoDroplets Efficiency.....	61
3.4.4 Signal Contrast in Tissue .....	62
3.5 Results and Discussion .....	63
3.5.1 Characteristic Signal of Photoacoustic nanoDroplets.....	63
3.5.2 Selective Optical Triggering of Photoacoustic nanoDroplets.....	66
3.5.3 Photoacoustic nanoDroplets Efficiency.....	68

3.5.4 Signal in a Tissue Environment .....	69
3.6 Conclusions.....	71
3.7 References.....	72
Chapter 4: Exploring Mechanisms Behind Photoacoustic nanoDroplets .....	73
4.1 Photoacoustic Phenomena .....	73
4.2 Photoacoustic Signal Generation Through Thermal Expansion.....	74
4.3 Photoacoustic nanoDroplet Functionality.....	75
4.4 Materials and Methods.....	79
4.4.1 PAnD Characteristic Signal Corresponding to Photoacoustic Phenomena.....	80
4.4.2 Optical Triggering Mechanism .....	81
4.5 Results and Discussion .....	81
4.5.1 PAnD Characteristic Signal Corresponding to Photoacoustic Phenomena.....	82
4.5.2 Optical Triggering Mechanism .....	83
4.6 Conclusions.....	86
4.7 References.....	87
Chapter 5: <i>In Vivo</i> Testing of Photoacoustic nanoDroplets.....	88
5.1 Introduction.....	88
5.2 Methods.....	89
5.2.1 Direct Intrapancreatic Injection Study .....	90
5.2.1.1 Contrast Agent Preparation.....	90
5.2.1.2 Imaging Procedure .....	90
5.2.1.3 Ultrasound Guided Intrapancreatic Injection.....	91
5.2.1.4 Gold Nanorod Control Animal .....	92
5.2.1.5 Animal Sacrifice and Dissection.....	92
5.2.1.6 Data Processing and Image Reconstruction.....	93
5.2.2 Tail Vein Injection Study.....	93
5.2.2.1 Subcutaneous Tumor Model .....	93
5.2.2.2 Contrast Agent Preparation.....	94

5.2.2.3 Imaging Procedure .....	94
5.2.2.4 Tail Vein Injection .....	95
5.2.2.5 Animal Sacrifice and Dissection.....	96
5.3 Results and Discussion .....	96
5.3.1 Intrapancreatic Injection .....	96
5.3.2 Tail Vein Injection .....	99
5.4 Conclusions.....	102
5.5 References.....	104
Chapter 6: Photoacoustic nanoDroplet Cellular Interactions.....	107
6.1 Introduction.....	107
6.2 Methods.....	109
6.2.1 Photoacoustic nanoDroplet Cytotoxicity .....	110
6.2.2 Passive Targeting Via Bovine Serum Albumin .....	111
6.2.3 Cellular Response to Vaporization of Photoacoustic nanoDroplets .....	112
6.3 Results and Discussion .....	114
6.3.1 Photoacoustic nanoDroplet Cytotoxicity .....	114
6.3.2 Passive Targeting Via Bovine Serum Albumin .....	115
6.3.3 Cellular Response to Vaporization of Photoacoustic nanoDroplets .....	116
6.4 Conclusions.....	124
6.5 References.....	124
Chapter 7: Molecular and Therapeutic Modifications of Photoacoustic nanoDroplets .....	128
7.1 Introduction.....	128
7.2 Methods.....	132
7.2.1 Molecular Targeting via a Biotin – Avidin Bridge .....	132
7.2.2 Molecular Targeting via an Avidin – Biotin Bridge .....	133
7.2.3 Drug Loading Synthesis – Paclitaxel.....	134
7.2.4 Passive Paclitaxel Drug Release .....	135
7.3 Results and Discussion .....	136

7.3.1 Molecular Targeting via a Biotin – Avidin Bridge .....	136
7.3.2 Molecular Targeting via a Avidin – Biotin Bridge .....	137
7.2.3 Drug Loading Synthesis – Paclitaxel .....	138
7.2.4 Passive Paclitaxel Drug Release .....	140
7.4 Conclusions .....	142
7.5 References .....	143
Chapter 8: Conclusions and Future Work .....	146
8.1 Motivation .....	146
8.2 Summary of Conclusions .....	148
8.2.1 Photoacoustic nanoDroplet Synthesis and Characterization .....	148
8.2.2 Cellular Interactions and Cytotoxicity .....	149
8.2.3 PAnD Functionality and Physical Responses .....	150
8.2.4 Contrast Enhancing Abilities of PAnDs .....	150
8.2.5 Therapeutic and Molecular Modifications of PAnDs .....	152
8.3 Future Directions for PAnDs .....	153
8.4 Summary of Contributions to the Field .....	156
8.5 References .....	158
References .....	161
Vita	179

## List of Figures

- Figure 1.1 Comparison between optical absorption properties of endogenous chromophores in tissue (left) and those of plasmonic noble metal nanoparticles of different shapes and sizes (right).....11
- Figure 2.1: Diagram depicting the dual-contrast agent concept – Photoacoustic nanoDroplets - consisting of plasmonic nanoparticles suspended in encapsulated PFC (a super-heated liquid at body temperature) and capped with a BSA shell. PAnDs may further contain therapeutic cargo and be surface functionalized for molecular targeting and cell-particle interactions. ....24
- Figure 2.2: (a) Cryogenic transmission electron microscopy (cTEM) image of PAnDs. Scale bar, 100 nm. (b) Extinction spectra of as-prepared nanorods (red, dashed line) and nanorods with a modified surface (blue, solid line). (c-e) cTEM images of unloaded PAnD and PAnDs with varying compositions including (d,e) loading with gold nanorods with various sizes (200 nm in panel c and d and 400 nm in panels e and f). (f) Traditional TEM image of PAnDs dried on carbon grid. Scale bars in c,d, 100 nm. Scale bars in e,f, 200 nm. ....40
- Figure 2.3: Natural size distribution of PAnDs made with 0.2mg/ml BSA in water before passage through the miniextruder. A majority of the particles will be naturally size below 1 micrometer due to the concentration of the BSA. The use of the miniextruder removes any larger particles and shifts the spectrum to the left.....41

Figure 2.4: (a) Photograph of phase transferred gold nanospheres (20 nm) with the octadecylamine method. (b) Photograph of phase transferred silver spheres. (c) Photograph of PAnDs with encapsulated silver spheres (left), gold nanospheres (right), and empty (center). .....43

Figure 2.5: (a) cTEM image of a PAnD loaded with gold nanorods phase transferred using the dodecanethiol method. (b) cTEM image of a PAnD loaded with gold nanorods phase transferred with the perfluorodecanethiol method. (c) Gold nanorods phase transferred with the perfluorodecanethiol method (1). PAnDs without nanoparticles loading (2). PAnDs loaded with gold nanorods phase transferred using the dodecanethiol method (3). PAnDs loaded with gold nanorods capped with perfluorodecanethiol (4). .....45

Figure 3.1: Depiction of experimental set up. The PAA phantom has been prepared with a horizontal, cylindrical inclusion. It is placed in a water bath with an optical window. A laser air-beam intersects the inclusion perpendicularly. The US transducer sits above the phantom, in the same plane as the air-beam perpendicular to the inclusion. The air-beam interacts with only half of the inclusion.....60

Figure 3.2: Left: US image of the phantom before laser irradiation showing boundaries of the inclusion containing the contrast agent. The shaded trapezoid indicated the approximate path of the laser beam. Center: US image of the inclusion after laser irradiation. Right, top: Optical microscopy images of the photoacoustic droplets within the PAA phantom. Right, bottom: Vaporized contrast agent. Each ultrasound image is 3 cm tall by 1 cm. ....64

Figure 3.3: (a and l) Ultrasound images before and after laser irradiation of inclusion containing the nanocarrier contrast agent. Green shape represents approximate air beam path. (b-k) Consecutive PA signal captured over 30 seconds .....	65
Figure 3.4: Analysis of photoacoustic signal intensity. In each PA frame, the total summed PA intensity is represented, and decays over time. ....	66
Figure 3.5: Position 1 through 16 and final represent the progression of applied laser positions within the phantom. As PAnDs are activated, they “write” the letters “U” and “T”. The corresponding photoacoustic signals (vaporization and TE panels) represent signals from the initial vaporization and the long term thermal expansion. ....	67
Figure 3.6: Graph showing the signal difference between gold nanorods (red line) and PAnDs (blue line) loaded with the same concentration of gold nanorods .....	68
Figure 3.7: Left and middle, Photoacoustic images of peak vaporization signal and prolonged thermal expansion signal of PAnDs. The white dashes outline the spleen, however most signal is seen above the spleen. Right, graph showing decrease in photoacoustic intensity with continued pulsed laser irradiation correlating with the characteristic signal of PAnDs .....	70
Figure 3.8: Top: Representative waveform of photoacoustic signal from the initial vaporization frame (8 <sup>th</sup> ). Bottom: Representative waveform of photoacoustic signal from nanoparticle mediated thermal expansion at the 100 <sup>th</sup> frame. ....	70

Figure 3.9: Left and middle, Ultrasound images before and after laser activation of injected PAnDs. Right, graph showing increase in ultrasound intensity with continued pulsed laser irradiation. Images are from circled frames. ....	71
Figure 4.1: Step-by-step diagram of remote activation of PAnDs, providing photoacoustic signal via two mechanisms: vaporization of PAnDs (steps 2-3) and thermal expansion caused by plasmonic nanoparticles (steps 4-5). The resulting gas microbubble of PFC (step 6) provides ultrasound contrast due to increased acoustic impedance mismatch. ....	77
Figure 4.2: Characteristic signal produced by PAnDs including initial peak signal due to vaporization of the liquid perfluorocarbon droplet and prolonged tail signal due to thermal expansion from the expelled gold nanoparticles. ....	78
Figure 4.3: Heating profiles in change in temperature ( $^{\circ}$ C) over distance (in radii of the sphere) and time for a 16 nm gold sphere in perfluorocarbon and water. Courtesy of Dr. Wolfgang Frey. ....	79
Figure 4.4: Graphs comparing signal trends of the peak signal (vaporization, left) and tail signal (thermal expansion, right) for the thermal expansion linear dependencies on nanoparticle concentration (top), and fluence (middle). Asterisks indicate values that are statistically significantly different from other conditions. ....	83

Figure 4.5: Top: ultrasound images from the first and last laser pulses (corresponding with the first and last ultrasound images), and a graph displaying the ultrasound signal increase over time. Bottom: ultrasound images from before the continuous laser was turned on and the last frame taken and a graph displaying the ultrasound signal increase over time. ....85

Figure 4.6: Graphs of photoacoustic signal over time for irradiation with a pulsed laser (left) and a continuous wave laser (right). ....86

Figure 5.1: (Left) The Visual Sonics Vevo2100 small animal imaging ultrasound system with transducer coupled with optical fibers to the SpectraPhysics Nd:YAG OPO laser system. (Right) Animal health was maintained with warming pad and injection guidance system. Picture courtesy of VisualSonics. ....91

Figure 5.2: Photoacoustic contrast enhancement *in vivo*. (a) Graph depicting the average photoacoustic intensity within the region of interest corresponding to the injected PAnDs, indicated by boxes in panel b and panel c. (b) Image of the peak photoacoustic signal generated from the rapid phase transition of the PAnDs. (c) Image representing photoacoustic signal generated from expelled gold nanorods and endogenous chromophores. Each frame is 20.4 mm wide by 12.8 mm tall. ultrasound is in 20-dB scale. In this experimental setup, ~50% of the droplets are disrupted by the 60th laser pulse. (d) Graph displaying changes of photoacoustic signals during continued pulsed laser irradiation of only gold nanorods. The green circles represent photoacoustic signal of the endogenous photoabsorbers in the mouse tissues. Blue circles represent the photoacoustic signal owing to thermal expansion caused by both the endogenous photoabsorbers and the injected gold nanorods. (e, f) Combined photoacoustic and ultrasound images of mouse cross-section and injection site of gold nanorods immediately after the laser was turned on (first laser pulse) and at the end of the laser pulsing (last laser pulse). Each image is 12.2 mm wide by 10.8 mm tall. ultrasound image is displayed using 20-dB scale. .98

Figure 5.3: Ultrasound contrast enhancement *in vivo*. (a) US image of a mouse before injection of PAnDs displaying the location of the spleen and pancreas. (b) US image after the direct injection and laser activation of PAnDs. Boxes in both images identify the region of interest where PAnDs were injected. Panels are 13.5 mm wide by 18.1 mm tall, and are in 20-dB scale. ....99

Figure 5.4: Photoacoustic and ultrasound images and corresponding signals over time of a tumor 4 hours after tail vein injection. The results indicate no accumulation of PAnDs in the tumor region; however, faulty tail vein injections cloud the interpretation of these results.....100

Figure 5.5: Photoacoustic and ultrasound images and corresponding signal over time of a tumor 24 hours after tail vein injection. The results indicate no accumulation of PAnDs in the tumor region; however, faulty tail vein injections cloud the interpretation of these results.....102

Figure 6.1: Relativity viability of A431 and MDA-MB-231 cells incubated with varying concentrations of PAnDs, PEGylated gold nanorods, and empty perfluorocarbon droplets for 30 hours as compared to control cells.115

Figure 6.2: Bright field microscopy images of cells (A431 and MD-MBA-231) incubated with PAnDs. ....116

Figure 6.3: Composite bright field and three color fluorescence images of cells which were exposed to vaporization of PAnDs at high and low concentrations or exposed to pulsed laser irradiation while surrounded by either gold nanorods or empty perfluorocarbon droplets. Spatially co-registered red and green signal appear yellow in the composite images. ....119

Figure 6.4: Relative levels as compared to untreated controls of “alive” stain, calcein/green, and “dead” stain, ethidium bromide/red, in two cell types after exposure to pulsed laser induced vaporization of PAnDs and their components. ....121

Figure 6.5: Immediate and long term cell viability assay results of MDA-MB-231 and A431 cells that underwent pulsed laser irradiation and close proximity vaporization of PAnD. ....123

Figure 7.1: Bright field and fluorescent microscopy images of PAnDs with biotin incorporated into the shell and fluorescent avidin attached to complete the bridge. Each scale bar represents 50  $\mu\text{m}$ . ....137

Figure 7.2: Bright field and florescent microscopy images of PAnDs with avidin incorporated into the shell with fluorescent biotin attached to complete the bridge. Each scale bar represents 50  $\mu\text{m}$ . ....138

Figure 7.3: Mass spectroscopy readings of three samples from left to right: Paclitaxel in chloroform, Paclitaxel in PAnDs, supernatant from PAnDs. Paclitaxel reads at 876.17 and 877.07. Notice different scale on y-axis. ....139

Figure 7.4: Bright field and fluorescent microscopy images of PAnDs loading with fluorescent Paclitaxel. Droplet position change is due to sample flow. White scale bar represents 50  $\mu\text{m}$ . ....140

Figure 7.5: Passive Paclitaxel drug release as a percent of total drug encapsulation from PAnDs over a 72 hour time period resulting in less than 3% release. At the 76 hour time point, the droplets were destroyed by heating to 60  $^{\circ}\text{C}$ , releasing approximately 76% of the drug. ....142

Figure 8.2: Diagram showing the proposed clinical use of PAnDs for treatment of triple-negative breast cancer through imaging diagnosis, imaged guided therapy, and treatment monitoring. ....155

## Chapter 1: Introduction

Cancer affects one-half of all men and one-third of all women in their lifetimes<sup>1</sup>. Fortunately, it has been shown that early detection of cancer dramatically increases survival rates<sup>1</sup>. Advances in medical imaging have allowed for early detection of cancers, but no imaging modality is without limitations. Computed tomography (CT), X-ray imaging, nuclear imaging, and magnetic resonance imaging (MRI) are the most common types of medical imaging employed by clinicians. However, these modalities use ionizing radiation or are not cost effective, and cannot provide high resolution and functional information simultaneously<sup>2</sup>. Another commonly used clinical imaging modality, ultrasound imaging, has been recently combined with a preclinical imaging modality called photoacoustic imaging<sup>3-8</sup> to provide a dual modality imaging scheme which provides morphological, functional, and molecular data<sup>9,10</sup> in a biologically noninvasive, real-time, and cost effective manner. Combined ultrasound and photoacoustic imaging can provide morphological and functional data solely from the intrinsic acoustic and optical contrasts within the body. However, to provide significantly higher contrast and extend molecular specificity, nanoparticle contrast agents must be used. As ultrasound and photoacoustic imaging modalities use different contrast phenomena (acoustic impedance and optical absorption, respectively), no single agent has yet been developed to provide contrast utilizing both of these mechanisms simultaneously.

The overall hypothesis of this work is the successful development of a nano-scale dual contrast agent that works concurrently for ultrasound and photoacoustic imaging. This novel and patented contrast agent, entitled Photoacoustic nanoDroplet, is designed, synthesized, and characterized in this dissertation<sup>11,12</sup>. The described work encompasses

the development from bench-top design to *in vivo* animal testing, with the goals of demonstrating feasibility for clinical research.

Chapter 1 introduces medical imaging in general. Ultrasound and photoacoustic imaging are reviewed specifically, with mention of the current contrast agents for these individual modalities. Furthermore, multifunctional nanoparticle contrast agents as therapeutic delivery systems are discussed. Finally, the research goals for this dissertation are outlined.

## **1.1 MEDICAL IMAGING**

Medical imaging creates images of what is inside the human body to help detect, diagnose, and treat disease. By 2010, over 5 billion medical imaging studies had been carried out worldwide<sup>13</sup>. The categories of medical imaging include x-ray and computed tomography (CT), nuclear imaging such as positron emission tomography (PET) and single-photon emission computed tomography (SPECT), magnetic resonance imaging (MRI), ultrasound imaging, and optical imaging (optical coherence tomography (OCT)). X-rays and computed tomography use electromagnetic radiation with wavelengths ranging from 0.1 to 10 nm, called x-rays, which pass through the body in different ways based on tissue density, and show a two-dimensional density projection. When several 2D slices are gathered, 3D images can be reconstructed. X-rays and CT scans are among the most commonly used medical imaging techniques due to their ability to rapidly scan large areas, great penetration depth, and high spatial resolution (down to 0.01 mm). However, the use of this modality must be limited due to the radiation dosage received during the procedure. In the last 10 years, almost 50% of the total radiation humans received was due to x-ray based imaging technologies<sup>14</sup>. Nuclear imaging uses radioactive decay to construct images of the body. This requires the injection of

radiopharmaceuticals into the patient. Nuclear imaging can provide information about tissue metabolic uptake, but has limited resolution (several mm) and also exposes the patient to ionizing radiation. MRI imaging uses a combination of strong magnets and RF signals to excite specific types of atoms into releasing RF signals, which are detected and then reconstructed into high-resolution (tens of micrometers) images of large volumes, as well as functional imaging of blood flow. Though MRI imaging does not use ionizing radiation, the size and costs associated with operating an MRI machine prohibit its use in many locations. Finally, optical imaging methods provide extremely high resolution images (sub-micrometer), but have very low penetration depth and imaging field. An ideal imaging modality would be real-time, cost-effective and portable with high resolution and penetration depth providing images of morphological and functional data.

## 1.2 ULTRASOUND IMAGING

Ultrasound imaging is a non-invasive, real-time, and cost-effective imaging modality that primarily images tissue morphology through the reflection and scattering of acoustic waves at tissue boundaries<sup>15</sup>. Different types of tissues exhibit acoustic impedances ( $Z$ ) described by the following equation

$$Z = \rho c \quad (1.1)$$

where  $\rho$  is the density ( $\text{kg/m}^3$ ) and  $c$  is the speed of sound ( $\text{m/s}$ ) in that tissue. At a tissue boundary where the acoustic impedances do not match, part of the wave is reflected, the amount scaled by the difference between the tissue impedances. Beyond acoustic reflection, scattering occurs when waves interact with objects smaller than the acoustic wavelength. These interactions give ultrasound images their characteristic speckle.

Ultrasound images are reconstructed by collecting the transmitted and reflected wave with transducers which traditionally use piezoelectric crystals to convert pressure

waves into electric charge. These radiofrequency (RF) signals are ordered by adjusting for differences in the time-of-flight and then summing individual signals from each element. This process is known as beamforming. Then a Hilbert transform, or enveloping function, is applied to the signal and presented in a logarithmic scale to enhance the signal of interest over scattering and sources with low reflectivity. The axial resolution of ultrasound images is directly related to the frequency of the transducers, but there is a tradeoff between resolution and imaging depth. High frequency transducers yield images with high axial resolution, but they penetrate tissue poorly. Diagnostic ultrasound is usually in the 3 to 15 MHz range<sup>15</sup>. Biological tissues have similar impedances owing to their large water content (excluding bone) so ultrasound imaging can benefit greatly from contrast agents.

### **1.3 ULTRASOUND CONTRAST AGENTS**

Exogenous contrast agents have been designed and developed for ultrasound contrast enhancement. The earliest used agents were perfluorocarbon (PFC) gas microbubbles, whose boiling point is below body temperature, and they have long been used in diagnostic ultrasound imaging as highly sensitive, cost effective, and biocompatible contrast agents<sup>16</sup>. Due to their highly scattering acoustic properties and nonlinear interactions with incident ultrasound, microbubbles are used in many clinical applications including assessment of coronary artery disease, hyperlipidaemia, angiogenesis, inflammation, and tumor formation. Microbubbles can also be used to assess therapeutic strategies and to facilitate delivery and release of therapeutic agents based on physical interactions of microbubbles with ultrasound<sup>17-19</sup>. Current research is focused on adapting the microbubbles, through surface modifications, cargo encapsulation or attachment, to allow for therapeutic applications<sup>20-27</sup>. Therefore,

microbubbles are a sensitive contrast agent that has vascular diagnostic and therapeutic effects. Beyond their uses in ultrasound contrast, perfluorocarbons have a long history in biomedical applications. They have been used as blood substitutes due to their ability to dissolve large quantities of oxygen and carbon dioxide<sup>28</sup>. The biocompatibility of PFC has been demonstrated in trials, and clinical doses are eliminated from the body through exhalation with a half life of approximately three days<sup>28</sup>.

Microbubbles do have limitations, however. Rapid gas diffusion and biological clearance significantly limit their intact circulation time and therefore, any potential therapeutic effects through cellular targeting and chemical or physical treatment<sup>29</sup>. Furthermore, due to their size ( $> 1$  micrometer), microbubble effects are limited to the vascular system. The invention of phase-shift PFC liquid droplets and acoustic droplet vaporization (ADV) has provided a method to solve these problems<sup>30,31</sup>. Liquid droplets of PFCs, often stabilized with albumin, lipids, or polymers, make for a long circulating, triggerable contrast agent. The boiling point below body temperature ( $37^{\circ}\text{C}$ ) cause these agents to become superheated in the body, and they easily vaporize in the presence of pulsed ultrasound with pressures in the sub-therapeutic range<sup>32</sup>. However, for tumor imaging, molecular diagnosis, and therapy, these particles must extravasate into the tumor interstitial space where cellular interactions could take place. To facilitate these cellular interactions, the phase change agents need to be smaller than the known endothelial gap junction sizes of up to 800 nm in tumor vasculature. The gap junction size depends strongly on tumor type and location, but sizes between 300 nm to 800 nm have been suggested, and thus, passive accumulation of nanoparticles in tumors, entitled the enhanced permeability and retention effect<sup>33</sup> (EPR), can occur with nanoparticles smaller than the junction size<sup>34-36</sup>.

While nanoscale PFC droplets can be easily synthesized, their inherent acoustic contrast is minimal (contrast enhancement through Rayleigh scattering of sound)<sup>37</sup>. Significant acoustic contrast from these droplets occurs only when they undergo a phase transition into a gaseous state. Studies have revealed that ADV requires increased acoustic input as the diameter of the droplets decreases (due to increased surface tension<sup>32</sup> and increased boiling point<sup>38</sup>) and the frequency of the transducer decreases<sup>31</sup>. The extra acoustic input energy is required for ADV because smaller droplets have significantly higher surface tension to overcome in order to vaporize. Combined with surface stabilizing agents (protein, lipids, and polymers) these particles are rendered them difficult to vaporize with typical diagnostic ultrasound frequencies and pressures<sup>32</sup>. Therefore, acoustic nanodroplet vaporization (AnDV) may require acoustic frequencies and pressures that will also cause unwanted bioeffects<sup>32</sup>. Hence, a methodology to activate PFC nanodroplets without unwanted bioeffects is desired.

#### **1.4 PHOTOACOUSTIC IMAGING**

In ultrasound imaging, acoustic transients propagate into the tissue, reflect based on impedance mismatch at structural boundaries, and return to the same transducer that emits them. Photoacoustic imaging is based on the photoacoustic phenomenon, where light energy is transformed into sound energy. A light source irradiates tissue, and acoustic transients are emitted based on the optical absorption properties of the sample, which are then collected by an ultrasound transducer. Because both imaging modalities used shared equipment for data collection, integration of photoacoustics with current ultrasound systems is usually straightforward. Though they utilize complementary equipment, these modalities provide significantly different information. Ultrasound imaging provides morphological data based on tissue composition boundaries.

Photoacoustic imaging provides information about the optical absorption of tissues, and thus can be correlated with chemical composition, providing functional/molecular information. The combination of photoacoustic and ultrasound imaging provides high spatial resolution images at traditionally ultrasonic depths, a potential benefit for medical imaging<sup>4,7,39,40</sup>.

The generation of sound from the interaction of light with a material is aptly named photoacoustics, a well described physical phenomenon<sup>41</sup>. Photoacoustic signal can be generated through four mechanisms, including thermal (also called thermoelastic) expansion<sup>42,43</sup>, vaporization<sup>42,43</sup>, photochemical processes<sup>43,44</sup> and optical breakdown<sup>42,43</sup>. These four processes produce photoacoustic signal from least to most efficiently in the order listed, but also require relative amounts of optical absorption in that order<sup>43,42</sup>. In biomedical applications of photoacoustic imaging and sensing, the only utilized and biologically safe mechanism to date is thermal expansion, because tissue can only withstand low levels of laser irradiation without undergoing irreversible damage<sup>45</sup>. Unfortunately, thermal expansion is the least efficient of the mechanisms of light–sound energy conversion and produces low amplitude acoustic waves<sup>43</sup>. Furthermore, the endogenous absorbers within tissues (melanin, hemoglobin and other porphyrins) have low optical absorption, limiting the overall contrast in photoacoustic imaging.

In thermal expansion-based photoacoustic imaging, sufficiently short laser pulses (5-10 ns) are absorbed by tissue chromophores, causing localized volume heating, leading to rapid expansion and generation of broadband acoustic pressure waves. These pressure transients are detected by an ultrasound transducer, and an image can be reconstructed from the time of flight and amplitude of the signals. Thermal expansion peak pressure generation ( $p_0$ ) can be described by the following equation

$$p_0 = \Gamma \mu_a F \quad (1.2)$$

where  $\Gamma$  is the Grüneisen coefficient (a dimensionless scale),  $\mu_a$  is the optical absorption coefficient of the absorber ( $\text{m}^{-1}$ ), and  $F$  is the laser fluence ( $\text{J}/\text{m}^2$ ). The Grüneisen coefficient is described as follows

$$\Gamma = \frac{\beta c^2}{C_p} \quad (1.3)$$

where  $\beta$  is the volume expansion coefficient ( $\text{K}^{-1}$ ),  $c$  is the speed of sound ( $\text{m}/\text{s}$ ), and  $C_p$  is the specific heat capacity ( $\text{J}/(\text{kg K})$ )<sup>46-48</sup>. However, thermal expansion occurs most efficiently when two conditions are met: thermal and stress confinement. Thermal confinement (1.4) occurs when the thermal diffusion is slower than the laser pulse duration (heat deposition). Stress confinement (1.5) occurs when the laser pulse duration is shorter than the acoustic wave propagation through the optical absorber. These conditions are defined mathematically as

$$\tau_0 \ll d_c^2 \frac{\rho C_p}{\chi} \quad (1.4)$$

$$\tau_0 \ll \frac{d_c}{c} \quad (1.5)$$

where  $\tau_0$  is the laser pulse duration (s),  $d_c$  is the characteristic dimension of the heated region (m),  $\rho$  is the mass density ( $\text{kg}/\text{m}^3$ ),  $C_p$  is the specific heat capacity at constant pressure ( $\text{J}/(\text{kg K})$ ),  $\chi$  is the thermal conductivity ( $\text{W}/(\text{m K})$ ), and  $c$  is the speed of sound ( $\text{m}/\text{s}$ )<sup>47,48</sup>.

Other photoacoustic phenomena are more efficient at converting optical energy to acoustic transients, but they require biologically unsafe levels of energy absorption<sup>45</sup>. Vaporization is the conversion of liquid to the gaseous state. Photochemical processes are the initiation of chemical reactions upon laser irradiation, and optical breakdown is the degradation of compounds via optical irradiation<sup>43</sup>. Vaporization is traditionally an

unwanted mechanism in tissues due to its potentially destructive properties, but it is possible to utilize this technique by the vaporization of an introduced agent. Conveniently, ultrasound contrast agents are routinely vaporized in a biologically safe manner and FDA approved for use in clinical applications<sup>30,49,50</sup>. The coupling of photoacoustic imaging with the vaporization of a traditionally ultrasound based contrast agent is utilized in this work, representing the first time photoacoustic imaging via vaporization has occurred safely in a living animal. The safety and efficacy of vaporization as a photoacoustic mechanism described more in Chapter 3 and Chapter 4.

## **1.5 PHOTOACOUSTIC CONTRAST AGENTS**

Photoacoustic imaging of native tissues can be accomplished by measuring their optical absorption. Tissue chromophores include blood (oxygenated and deoxygenated absorption properties differ widely in the visible range), melanin, fat, and water<sup>51</sup>. The optical absorption properties of these tissues are shown in Fig. 1.1. These components can be used to identify tissue types, and even provide functionality such as blood oxygenation. However, compared to exogenous contrast agents, endogenous absorbers have low absorption coefficients, which limits the overall sensitivity of photoacoustic imaging<sup>52</sup>. Furthermore, all absorption of tissues dramatically decreases between 600 and 1264 nm promoting what is known as a tissue “optical window”. Exogenous agents that absorb in these wavelengths provide even higher contrast.

Exogenous agents can produce photoacoustic contrast with several-fold higher magnitude than intrinsic endogenous contrast alone. Plasmonic noble metal nanoparticles, primarily made from gold<sup>9,53–55</sup> and silver<sup>55,56</sup>, are the most frequently used agents. The superior optical absorption properties of plasmonic nanoparticles arise from their ability to undergo local surface plasmon resonance. When an electromagnetic wave

interacts with a plasmonic nanoparticle, which has a wavelength and size of similar magnitude, the free surface electrons oscillate with the polarity of the inciting wave. The energy from the electromagnetic wave is absorbed, causing oscillation of the electrons, and is released as heat, resulting in high attenuation (absorption) of the incident electromagnetic wave. Multiple absorption peaks at different wavelengths arise from the different orientations in which the nanoparticle could interact with the inciting wave. Plasmonic nanoparticles are highly optically absorbing, and their optical absorption can be increased by shape/composition modifications, owing to surface area and volume effects<sup>57</sup>. The synthesis of these nanoparticles can be easily tuned to produce a variety of different shapes, including nanospheres<sup>9,53</sup>, nanoshells<sup>57,58</sup>, nanorods<sup>54,59</sup>, and nanocages<sup>56,60</sup>. Also, the peak absorption wavelength may be varied by changing synthesis conditions to control the size and shape of the nanoparticle, as shown in Fig. 1.1. A strong optical absorption in the near infrared region (NIR) around 1064 nm often allows for deep imaging within biological tissues due to the low optical absorption and scattering properties of tissue's constituents at this wavelength<sup>10</sup>. Research on gold nanoparticles has advanced to the *in vivo* clinical trial stage<sup>61</sup>. Previous studies have examined the *in vitro* cytotoxicity of nanoparticles<sup>62</sup>, many of which can be used as contrast agents for photoacoustic imaging. As with most biomedical nanoparticle applications, the size, shape and surface properties affect the biodistribution and efficacy of nanoparticle contrast agents *in vivo*<sup>63,64</sup>.

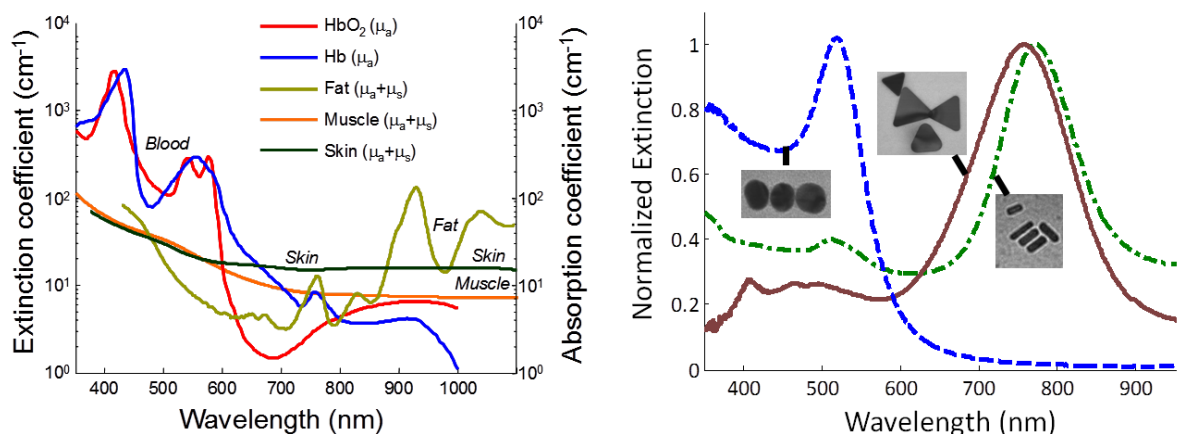


Figure 1.1 Comparison between optical absorption properties of endogenous chromophores in tissue (left) and those of plasmonic noble metal nanoparticles of different shapes and sizes (right).

Plasmonic nanoparticles can also be used for therapeutic applications. The strong optical absorption of a contrast agent can, if using a continuous wave laser, produce a thermal heating effect by nanoparticles that could cause cell injury – an effect that can be used for photothermal therapy<sup>65–67</sup>. Applications of exogenous contrast agents for photoacoustic imaging take advantage of the unique targeting capabilities of nanoparticles. Diseases such as cancer<sup>52,68</sup> and atherosclerosis<sup>69</sup> may be imaged more effectively using a photoacoustic contrast agent. Imaging of specific tumor cell types using targeted nanoparticles<sup>68,70</sup> and of the metastasis of tumor cells<sup>71</sup> have been demonstrated.

Organic dyes, such as indocyanine green<sup>60,72</sup> and Evan's blue<sup>73</sup>, also have distinct absorption properties, and can provide exogenous contrast. However, these dyes are prone to photobleaching, which limits their ability to produce sustained photoacoustic transients. Fluorescent proteins also allow for photoacoustic imaging of cellular phenomenon *in vivo*<sup>74</sup>.

## 1.6 MULTIFUNCTIONAL CONTRAST AGENTS

Interestingly, both ultrasound and photoacoustic contrast agents are now synthesized in the nanoscale. Research in nanotechnology and its implications for biomedical imaging and therapy have dramatically increased over the past ten years<sup>75</sup>. One finding is that material properties change depending on whether a material is in bulk or in the nanoscale<sup>76</sup>. For example, nano-gold undergoes plasmon resonance, allowing it to be a contrast agent for photoacoustic imaging, whereas bulk gold does not. In ultrasound contrast agents, the boiling points of perfluorocarbons change as the volume of the droplet varies<sup>18</sup>. In addition, nano scale technologies also have the ability to interact with biological systems on the scale of reactions, DNA, and cells when synthesized in the nano scale. Therefore, much attention has been focused on developing multifunctional nanoparticles that can detect, diagnose, and even treat disease within a single nanovector<sup>26,77,78</sup>. Nanoscale contrast agents have been the focus of molecular targeting and drug delivery. When using nanoscale vectors for therapeutic delivery, researchers can limit damage to non-diseased tissues via site-specific delivery and optimal drug dosages for those applications. Both of these abilities make current chemotherapeutic drugs more efficient at killing cancer cells due to higher dosages at a specific site, while simultaneously reducing systemic side effects that lower the patient's quality of life.

Ultrasound contrast agents provide an excellent opportunity to encapsulate chemotherapeutics and other compounds due to their large size and dual environments of their organic interiors and aqueous exteriors. Currently, these particles have been synthesized for treating atherosclerosis<sup>23,79</sup>, delivery of chemotherapy drugs (paclitaxel<sup>80-82</sup>, gemcitabine<sup>83,84</sup>, and docirubicin<sup>85,86</sup>) to solid tumors<sup>87</sup>, delivering gene therapies<sup>49,88-90</sup>, and delivering antibiotics<sup>49</sup>. Furthermore, ultrasound contrast agents are easily

targetable using molecular attachments such as monoclonal antibodies and small molecules<sup>91-94</sup>. Photoacoustic contrast agents can also be conjugated with targeting moieties<sup>95-97</sup> and drugs<sup>98</sup>. Therefore, a combined contrast agent based on micro droplets and plasmonic nanoparticles has excellent abilities to be targeted, drug delivery vectors.

## **1.7 OVERALL RESEARCH GOALS AND DISSERTATION ORGANIZATION**

The overall goal of this project is to design, synthesize, and test a dual contrast agent for combined ultrasound and photoacoustic imaging. In order to accomplish this goal several research directions were taken to ensure its feasibility. First, design, synthesis, and characterization of the dual contrast agent were undertaken. Next, the agent was tested in phantom experiments to determine the mechanism of dual-modality contrast enhancement and characteristic enhancement capabilities. Then, the contrast agent needed to demonstrate feasibility to be used in living systems through *in vivo* mouse experiments. How this contrast agent interacts with cells, both passively and actively needed to be studied. Finally, multiple functionality of the contrast agent as a targeted drug delivery vehicle was explored. These research directions will aid in achieving the creation of a dual contrast agent for combined ultrasound and photoacoustic imaging.

This dissertation is organized in the following manner. Chapter 1 reviews background information on ultrasound and photoacoustic imaging, their current contrast agents, and how they differ from current medical imaging techniques. In Chapter 2, the dual contrast agent, Photoacoustic nanoDroplets (PAnDs), are designed, synthesized and characterized. In Chapters 3 and 4, the characteristic signal enhancement and functionality of the agents are explored. Chapter 5 shows PAnD usage in mouse models. Chapter 6 explores how PAnDs interact and affect cells both passively and when

activated. In Chapter 7, targeting and drug release are explored. Finally, in Chapter 8 the overall conclusion of the work, future directions, and contribution to the field are discussed.

## 1.8 REFERENCES

1. Hayat, M.J., Howlader, N., Reichman, M.E. & Edwards, B.K. Cancer Statistics, Trends, and Multiple Primary Cancer Analyses from the Surveillance, Epidemiology, and End Results (SEER) Program. *Oncologist* **12**, 20-37 (2007).
2. Hendee E. Russell, W.R.R. *Medical Imaging Physics*. 512 (Wiley\_Liss, Inc.: New York, 2002).
3. Oraevsky, A.A., Jacques, S.L. & Tittel, F.K. Determination of tissue optical properties by time-resolved detection of laser-induced stress waves. *Proc. SPIE* **1882**, 86-101 (1993).
4. Oraevsky, A.A., Jacques, S.L., Esenaliev, R.O. & Tittel, F.K. Time-Resolved Optoacoustic Imaging in Layered Biological Tissues. *Advances in Optical Imaging and Photon Migration* **21**, 161-165 (1994).
5. Oraevsky, A.A., Esenaliev, R.O., Jacques, S.L., Thomsen, S.L. & Tittel, F.K. Lateral and z-axial resolution in laser optoacoustic imaging with ultrasonic transducers. *Proc. SPIE* **2389**, 198-208 (1995).
6. Oraevsky, A.A., Jacques, S.L. & Tittel, F.K. Measurement of tissue optical properties by time-resolved detection of laser-induced transient stress. *Appl Opt* **36**, 402-415 (1997).
7. Kruger, R.A. Photoacoustic ultrasound. *Med Phys* **21**, 127-131 (1994).
8. Kruger, R.A., Liu, P., Fang, Y.R. & Appledorn, C.R. Photoacoustic ultrasound (PAUS)--reconstruction tomography. *Med Phys* **22**, 1605-1609 (1995).
9. Mallidi, S., Larson, T., Aaron, J., Sokolov, K. & Emelianov, S. Molecular specific optoacoustic imaging with plasmonic nanoparticles. *Opt Express* **15**, 6583-6588 (2007).
10. Homan, K. *et al.* Prospects of molecular photoacoustic imaging at 1064 nm wavelength. *Opt. Lett.* **35**, 2663-2665 (2010).
11. Emelianov, S., Wilson, K. & Homan, K. Nanocarriers for Imaging and Therapy Applications. (2011).at  
<<http://www.wipo.int/patentscope/search/en/detail.jsf?docId=WO2011035279>>

12. Wilson, K., Homan, K. & Emelianov, S. Biomedical photoacoustics beyond thermal expansion using triggered nanodroplet vaporization for contrast-enhanced imaging. *Nature Communications* **3**, 618 (2012).
13. Roobottom, C.A., Mitchell, G. & Morgan-Hughes, G. Radiation-reduction strategies in cardiac computed tomographic angiography. *Clinical Radiology* **65**, 859-867 (2010).
14. Medical Radiation Exposure Of The U.S. Population Greatly Increased Since The Early 1980s. at <http://www.sciencedaily.com/releases/2009/03/090303125809.htm>
15. Christensen, D.A. *Ultrasonic Bioinstrumentation*. (John Wiley & Sons, Inc.: New York, 1988).
16. Yokoyama, M. & Nishihara, M. Perfluorocarbon emulsions and ultrasonic contrast agents containing the same. 13pp. (2010).
17. Kawabata, K., Asami, R., Azuma, T. & Umemura, S. Acoustic response of microbubbles derived from phase-change nanodroplet. *Jpn. J. Appl. Phys.* **49**, 07HF18/1-07HF18/9 (2010).
18. Nam, K.-H., Christensen, D.A., Kennedy, A.M. & Rapoport, N. Acoustic Droplet Vaporization, Cavitation, and Therapeutic Properties of Copolymer-Stabilized Perfluorocarbon Nanoemulsions. *AIP Conf. Proc.* **1113**, 124-128 (2009).
19. Stride, E.P. & Coussios, C.C. Cavitation and contrast: the use of bubbles in ultrasound imaging and therapy. *Proc Inst Mech Eng H* **224**, 171-191 (2010).
20. Lanza, G. *et al.* Targeted Perfluorocarbon Nanoparticles for Diagnosis and Therapy. *Mater. Res. Soc. Symp. Proc.* **1019E**, No pp. given, Paper #: 1019-FF02-04 (2007).
21. Wickline, S.A. Perfluorocarbon nanoemulsions for molecular imaging and therapy. FLUO-019 (2007).
22. Ferrara, K., Pollard, R. & Borden, M. Ultrasound microbubble contrast agents: fundamentals and application to gene and drug delivery. *Annu. Rev. Biomed. Eng.* **9**, 415-447 (2007).
23. Caruthers, S.D., Cyrus, T., Winter, P.M., Wickline, S.A. & Lanza, G.M. Anti-angiogenic perfluorocarbon nanoparticles for diagnosis and treatment of atherosclerosis. *Wiley Interdiscip. Rev.: Nanomed. Nanobiotechnol.* **1**, 311-323 (2009).
24. Chen, D. & Wu, J. An in vitro feasibility study of controlled drug release from encapsulated nanometer liposomes using high intensity focused ultrasound. *Ultrasonics* **50**, 744-749 (2010).

25. Eisenbrey, J.R. *et al.* Development and optimization of a doxorubicin loaded poly(lactic acid) contrast agent for ultrasound directed drug delivery. *J. Controlled Release* **143**, 38-44 (2010).
26. Ferrante, E.A., Pickard, J.E., Rychak, J., Klibanov, A. & Ley, K. Dual targeting improves microbubble contrast agent adhesion to VCAM-1 and P-selectin under flow. *J. Controlled Release* **140**, 100-107 (2009).
27. Kaneda, M.M., Caruthers, S., Lanza, G.M. & Wickline, S.A. Perfluorocarbon nanoemulsions for quantitative molecular imaging and targeted therapeutics. *Ann Biomed Eng* **37**, 1922-1933 (2009).
28. Flaim, S.F. Pharmacokinetics and Side Effects of Perfluorocarbon-Based Blood Substitutes. *Artificial Cells, Blood Substitutes and Biotechnology* **22**, 1043-1054 (1994).
29. Dijkmans, P.A. *et al.* Microbubbles and ultrasound: from diagnosis to therapy. *European Journal of Echocardiography* **5**, 245-246 (2004).
30. Correas, J.M. & Quay, S.D. EchoGen emulsion: a new ultrasound contrast agent based on phase shift colloids. *Clinical radiology* **51 Suppl 1**, 11-14 (1996).
31. Kripfgans, O.D., Fowlkes, J.B., Miller, D.L., Eldevik, O.P. & Carson, P.L. Acoustic droplet vaporization for therapeutic and diagnostic applications. *Ultrasound Med Biol* **26**, 1177-1189 (2000).
32. Sheeran, P.S., Luois, S., Dayton, P.A. & Matsunaga, T.O. Formulation and Acoustic Studies of a New Phase-Shift Agent for Diagnostic and Therapeutic Ultrasound. *Langmuir* **27**, 10412-10420 (2011).
33. Matsumura, Y. & Maeda, H. A new concept for macromolecular therapeutics in cancer chemotherapy: mechanism of tumoritropic accumulation of proteins and the antitumor agent smancs. *Cancer Research* **46**, 6387-6392 (1986).
34. Hobbs, S.K. *et al.* Regulation of transport pathways in tumor vessels: Role of tumor type and microenvironment. *Proceedings of the National Academy of Sciences* **95**, 4607-4612 (1998).
35. Brigger, I., Dubernet, C. & Couvreur, P. Nanoparticles in cancer therapy and diagnosis. *Adv Drug Deliv Rev* **54**, 631-651 (2002).
36. Campbell, R.B. Tumor Physiology and Delivery of Nanopharmaceuticals. *Anti-Cancer Agents in Medicinal Chemistry (Formerly Current Medicinal Chemistry* **6**, 10 (2006).
37. Couture, O. *et al.* A model for reflectivity enhancement due to surface bound submicrometer particles. *Ultrasound in Medicine & Biology* **32**, 1247-1255 (2006).

38. Rapoport, N.Y., Efros, A.L., Christensen, D.A., Kennedy, A.M. & Nam, K.H. Microbubble Generation in Phase-Shift Nanoemulsions used as Anticancer Drug Carriers. *Bubble Sci Eng Technol* **1**, 31-39 (2009).
39. Bowen, T. Radiation-Induced Thermoacoustic Soft Tissue Imaging. *1981 Ultrasonics Symposium* 817-822 (1981).
40. Xu, M. & Wang, L.V. Photoacoustic imaging in biomedicine. *Review of Scientific Instruments* **77**, 41101 (2006).
41. Bell, A.G. Production of sound by radiant energy. *Journal of Franklin Institute* **111**, 401-426 (1881).
42. Lyamshev, L.M. Optoacoustic sources of sound. *SOV PHYS USPEKHI* **24**, 977–995 (1981).
43. Sigrist, M.W. Laser generation of acoustic waves in liquids and gases. *Journal of Applied Physics* **60**, R83-R122 (1986).
44. Chen, H. & Diebold, G. Chemical generation of acoustic waves: a giant photoacoustic effect. *Science* **v270**, p963(4) (1995).
45. ANSI Orlando: Laser Institute of America . *American National Standard for Safe use of Lasers, ANSI Z136.1* (2000).
46. Li, C. & Wang, L.H.V. Photoacoustic tomography and sensing in biomedicine. *Physics in Medicine and Biology* **54**, R59 (2009).
47. Wang, L.V., Wu, H.-I. & Masters, B.R. Biomedical Optics, Principles and Imaging. *Journal of Biomedical Optics* **13**, 049902 (2008).
48. Oraevsky, A. & Karabutov, A. Optoacoustic tomography. (2003).
49. Bekerredjian, R., Grayburn, P.A. & Shohet, R.V. Use of ultrasound contrast agents for gene or drug delivery in cardiovascular medicine. *Journal of the American College of Cardiology* **45**, 329-335 (2005).
50. Kiessling, F., Huppert, J. & Palmowski, M. Functional and molecular ultrasound imaging: concepts and contrast agents. *Curr. Med. Chem.* **16**, 627-642 (2009).
51. Emelianov, S.Y. *et al.* Combined ultrasound, optoacoustic, and elasticity imaging. *Proceedings of the SPIE Photonics West* **5320**, 101-112 (2004).
52. Copland, J.A. *et al.* Bioconjugated gold nanoparticles as a molecular based contrast agent: implications for imaging of deep tumors using optoacoustic tomography. *Mol Imaging Biol* **6**, 341-349 (2004).
53. Oraevsky, A.A., Karabutov, A.A. & Savateeva, E.V. Enhancement of optoacoustic tissue contrast with absorbing nanoparticles. *European Conference on Biomedical Optics, Proc. SPIE* **4434**, 60-69 (2001).

54. Eghtedari, M. *et al.* High sensitivity of in vivo detection of gold nanorods using a laser optoacoustic imaging system. *Nano Lett* **7**, 1914-1918 (2007).
55. Wilson, K., Homan, K. & Emelianov, S. Synthesis of a dual contrast agent for ultrasound and photoacoustic imaging. *Photonics West* **7576**, 75760M (2010).
56. Homan, K. *et al.* Combined ultrasound and photoacoustic imaging of pancreatic cancer using nanocage contrast agents. *SPIE Photonics West* **7177**, 71771M (2009).
57. Lu, W. *et al.* Photoacoustic imaging of living mouse brain vasculature using hollow gold nanospheres. *Biomaterials* **31**, 2617-2626 (2010).
58. Wang, Y.W. *et al.* Photoacoustic tomography of a nanoshell contrast agent in the in vivo rat brain. *Nano Letters* **4**, 1689-1692 (2004).
59. Li, P.C. *et al.* Multiple targeting in photoacoustic imaging using bioconjugated gold nanorods. **6086**, 60860M (2006).
60. Yang, X.M., Skrabalak, S.E., Li, Z.Y., Xia, Y.N. & Wang, L.H.V. Photoacoustic tomography of a rat cerebral cortex in vivo with au nanocages as an optical contrast agent. *Nano Letters* **7**, 3798-3802 (2007).
61. Goel, R., Shah, N., Visaria, R., Paciotti, G.F. & Bischof, J.C. Biodistribution of TNF-alpha-coated gold nanoparticles in an in vivo Model System. *Nanomedicine* **4**, 401-410 (2009).
62. Lewinski, N., Colvin, V. & Drezek, R. Cytotoxicity of nanoparticles. *Small* **4**, 26-49 (2008).
63. Phillips, M.A., Gran, M.L. & Peppas, N.A. Targeted nanodelivery of drugs and diagnostics. *Nano Today* **5**, 143-159
64. Owens III, D.E. & Peppas, N.A. Opsonization, biodistribution, and pharmacokinetics of polymeric nanoparticles. *International Journal of Pharmaceutics* **307**, 93-102 (2006).
65. Pitsillides, C.M., Joe, E.K., Wei, X., Anderson, R.R. & Lin, C.P. Selective cell targeting with light-absorbing microparticles and nanoparticles. *Biophys J* **84**, 4023-4032 (2003).
66. Gobin, A.M. *et al.* Near-infrared resonant nanoshells for combined optical imaging and photothermal cancer therapy. *Nano Lett* **7**, 1929-1934 (2007).
67. Joshi, P., Chen, Y.-S., Kim, S., Shah, J. & Emelianov, S. Molecular Therapeutic Agents for Noninvasive Photoacoustic Image-guided Photothermal Therapy. *31st Annual International IEEE The Engineering in Medicine and Biology Conference (EMBC) Proceedings* **1158**, (2009).

68. Mallidi, S. *et al.* Multiwavelength Photoacoustic Imaging and Plasmon Resonance Coupling of Gold Nanoparticles for Selective Detection of Cancer. *Nano Lett* (2009).doi:10.1021/nl802929u
69. Wang, B. *et al.* Plasmonic intravascular photoacoustic imaging for detection of macrophages in atherosclerotic plaques. *Nano Letters* **9**, 2212–2217 (2009).
70. Eghtedari, M.A. *et al.* Bioconjugated gold nanoparticles as a contrast agent for optoacoustic detection of small tumors. *Biomedical Optoacoustics Iv* **4960**, 76-85 (2003).
71. Galanzha, E.I. *et al.* In vivo fiber-based multicolor photoacoustic detection and photothermal purging of metastasis in sentinel lymph nodes targeted by nanoparticles. *Journal of Biophotonics* **2**, 528-539 (2009).
72. Ku, G. & Wang, L.H.V. Deeply penetrating photoacoustic tomography in biological tissues enhanced with an optical contrast agent. *Optics Letters* **30**, 507-509 (2005).
73. Yao, J., Maslov, K., Hu, S. & Wang, L.H.V. Evans blue dye-enhanced capillary-resolution photoacoustic microscopy in vivo. *Journal of Biomedical Optics* **14**, 54049 (2009).
74. Razansky, D. *et al.* Multispectral opto-acoustic tomography of deep-seated fluorescent proteins in vivo. *Nat Photon* **3**, 412-417 (2009).
75. Youtie, J., Shapira, P. & Porter, A.L. Nanotechnology publications and citations by leading countries and blocs. *Journal of Nanoparticle Research* **10**, 981-986 (2008).
76. Eustis, S. & El-Sayed, M.A. Why gold nanoparticles are more precious than pretty gold: Noble metal surface plasmon resonance and its enhancement of the radiative and nonradiative properties of nanocrystals of different shapes. *Chemical Society Reviews* **35**, 209-217 (2006).
77. Soman, N.R., Marsh, J.N., Lanza, G.M. & Wickline, S.A. New mechanisms for non-porative ultrasound stimulation of cargo delivery to cell cytosol with targeted perfluorocarbon nanoparticles. *Nanotechnology* **19**, 185102/1-185102/7 (2008).
78. Nishihara, M., Imai, K. & Yokoyama, M. Preparation of perfluorocarbon/fluoroalkyl polymer nanodroplets for cancer-targeted ultrasound contrast agents. *Chem. Lett.* **38**, 556-557 (2009).
79. Winter, P.M. *et al.* Endothelial alpha(v)beta3 integrin-targeted fumagillin nanoparticles inhibit angiogenesis in atherosclerosis. *Arteriosclerosis, thrombosis, and vascular biology* **26**, 2103-9 (2006).
80. Azouz, S.M. *et al.* Prevention of local tumor growth with paclitaxel-loaded microspheres. *J Thorac Cardiovasc Surg* **135**, 1014-1021 (2008).

81. Soga, O. *et al.* Thermosensitive and biodegradable polymeric micelles for paclitaxel delivery. *Journal of Controlled Release* **103**, 341-353 (2005).
82. Tartis, M.S. *et al.* Therapeutic effects of paclitaxel-containing ultrasound contrast agents. *Ultrasound Med Biol* **32**, 1771-1780 (2006).
83. Immordino, M.L. *et al.* Preparation, characterization, cytotoxicity and pharmacokinetics of liposomes containing lipophilic gemcitabine prodrugs. *J Control Release* **100**, 331-346 (2004).
84. Castelli, F., Sarpietro, M.G., Ceruti, M., Rocco, F. & Cattel, L. Characterization of Lipophilic Gemcitabine Prodrug-Liposomal Membrane Interaction by Differential Scanning Calorimetry. *Mol. Pharm. FIELD Full Journal Title:Molecular Pharmaceutics* **3**, 737-744 (2006).
85. Escoffre, J.M., Piron, J., Novell, A. & Bouakaz, A. Doxorubicin Delivery into Tumor Cells with Ultrasound and Microbubbles. *Mol. Pharmaceutics* **8**, 799-806 (2011).
86. Ta, T., Convertine, A.J., Reyes, C.R., Stayton, P.S. & Porter, T.M. Thermosensitive Liposomes Modified with Poly(N-isopropylacrylamide-co-propylacrylic acid) Copolymers for Triggered Release of Doxorubicin. *Biomacromolecules* **11**, 1915-1920 (2010).
87. Rowinsky, E.K. & Donehower, R.C. Paclitaxel (taxol). *N Engl J Med* **332**, 1004-1014 (1995).
88. Frenkel, V. Ultrasound mediated delivery of drugs and genes to solid tumors. *Adv Drug Deliv Rev* **60**, 1193-1208 (2008).
89. Suzuki, R. *et al.* Cancer gene therapy by IL-12 gene delivery using liposomal bubbles and tumoral ultrasound exposure. *J. Controlled Release* **142**, 245-250 (2010).
90. Yoon, C.S. & Park, J.H. Ultrasound-mediated gene delivery. *Expert Opin. Drug Delivery* **7**, 321-330 (2010).
91. Waters, E.A. *et al.* Detection of targeted perfluorocarbon nanoparticle binding using <sup>19</sup>F diffusion weighted MR spectroscopy. *Magn. Reson. Med.* **60**, 1232-1236 (2008).
92. Wickline, S.A. & Lanza, G.M. Nanotechnology for molecular imaging and targeted therapy. *Circulation* **107**, 1092-1095 (2003).
93. Dayton, P.A. *et al.* Application of ultrasound to selectively localize nanodroplets for targeted imaging and therapy. *Mol Imaging* **5**, 160-174 (2006).
94. Rapoport, N., Gao, Z. & Kennedy, A. Multifunctional nanoparticles for combining ultrasonic tumor imaging and targeted chemotherapy. *J. Natl. Cancer Inst.* **99**, 1095-1106 (2007).

95. Eghtedari, M., Liopo, A.V., Copland, J.A., Oraevsky, A.A. & Motamedi, M. Engineering of Hetero-Functional Gold Nanorods for the in vivo Molecular Targeting of Breast Cancer Cells. *Nano Lett* **9**, 287-291 (2009).
96. Eck, W. *et al.* PEGylated gold nanoparticles conjugated to monoclonal F19 antibodies as targeted labeling agents for human pancreatic carcinoma tissue. *ACS Nano* **2**, 2263-2272 (2008).
97. Agarwal, A. *et al.* Targeted gold nanorod contrast agent for prostate cancer detection by photoacoustic imaging. *Journal of Applied Physics* **102**, 64701 (2007).
98. Bergen, J.M., von Recum, H.A., Goodman, T.T., Massey, A.P. & Pun, S.H. Gold nanoparticles as a versatile platform for optimizing physicochemical parameters for targeted drug delivery. *Macromol Biosci* **6**, 506-516 (2006).

## **Chapter 2: Design, Synthesis, and Characterization of Photoacoustic nanoDroplets (PAnDs)**

The overall objective of this research project is to design and synthesize a nano-sized, dual contrast agent for combined ultrasound and photoacoustic imaging that is capable of enhancing the contrast of both modalities simultaneously. The design, synthesis, and physical characterization of the contrast agent, termed Photoacoustic nanoDroplets (PAnDs), are explained in detail in this chapter. Each material component as a design element is discussed. Furthermore, the synthesis procedure is outlined here. In the absence of any specific modifications noted throughout the dissertation, the methods for synthesis of PAnDs as described in this chapter were employed. Finally, the results of the physical characterization are shown.

PAnDs, as illustrated in Fig. 2.1, are comprised of two previously developed contrast agents, perfluorocarbon droplets for ultrasound imaging and plasmonic noble metal nanoparticles for photoacoustic imaging modified into a novel, dual contrast agent. These agents comprise a nanosize droplet of perfluorocarbon (a super-heated liquid at body temperature), a bovine serum albumin (BSA) shell to provide stability, and plasmonic gold nanorods for acting as wavelength-tunable, photoacoustic contrast and as a “fuse” to vaporize the perfluorocarbon into its active, ultrasound contrast-enhancing state. The resulting agent, however, is more than the sum of its parts providing, overall, three forms of contrast and enabling vaporization to be used as a contrast mechanism in a biological system for the first time (discussed more in Chapters 3 and 4). However, several other design factors were considered during this process including a reduction in size to the nano scale, the use of nontoxic components, the ability to act as a platform for delivering therapeutics, and a means to be surface functionalized to allow for molecular targeting strategies.

## **2.1 PAND COMPONENTS**

The components used in designing and synthesizing PAnDs are discussed in detail here, including brief histories of their use in biomedical applications and specific design criteria met by their inclusion.

### **2.1.1 Perfluorocarbon Droplets**

PAnD's main component, a perfluorocarbon (PFC) droplet, has a long history as an exogenous contrast agent for ultrasound contrast enhancement as explored in Chapter 1. These agents, however, started as gas microbubbles due to PFC's boiling point below body temperature, and have long been used in diagnostic ultrasound imaging as highly sensitive, cost effective, and biocompatible contrast agents<sup>1</sup>. Due to their highly scattering acoustic properties and nonlinear interactions with incident ultrasound, microbubbles are used in many clinical applications. However, gas diffusion and biological clearance significantly limit their circulation time and size inhibits their extravasations out of the vascular system<sup>2</sup>. Phase change, ultrasound activated, contrast agents were introduced to increase circulation time and stability, but decreasing the size to the nanoscale presents an activation challenge<sup>3</sup>. In PAnDs we use an optical activation strategy (explained further in section 2.2 and Chapters 3 and 4).

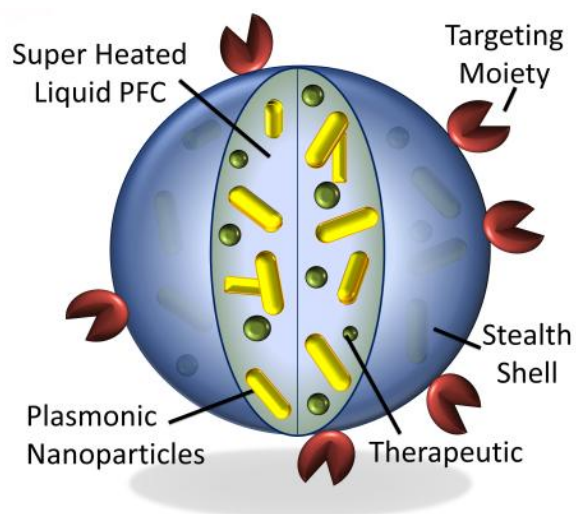


Figure 2.1: Diagram depicting the dual-contrast agent concept – Photoacoustic nanoDroplets - consisting of plasmonic nanoparticles suspended in encapsulated PFC (a super-heated liquid at body temperature) and capped with a BSA shell. PAnDs may further contain therapeutic cargo and be surface functionalized for molecular targeting and cell-particle interactions.

The choice of which specific perfluorocarbon would be used in this research was determined by examining several factors including historical usage, boiling temperature, ease of handling, and cost; the most important of these being boiling temperature. In order to become super heated in the body to allow for triggered vaporization, the boiling temperature had to be below body temperature at 37 °C. However, to avoid any special requirements for handling the PFC and to synthesize a liquid droplet, the boiling temperature should be above room temperature of approximately 21 °C. Since the boiling temperature increases with the number of carbons in the backbone, only one PFC could be considered, perfluoropentane (5 carbons, boiling point at 27 °C), as perfluorobutane (4 carbons) has a boiling point of -1.7 °C and perfluorohexane (6 carbons) has a boiling point of 57 °C. For these reasons, a majority of phase change contrast agents are made with perfluoropentane, minus a few exceptions requiring special synthesis methods at

cold temperature or condensation reactions<sup>3</sup>. Finally, perfluoropentane is readily available from Fluoromed Inc. in Round Rock, Texas. Therefore, perfluoropentane was chosen as the perfluorocarbon to be used in this research.

### 2.1.2 Shell

Due to their nano scale size, droplets of perfluorocarbon are inherently unstable. This instability is due to the high Laplace pressure, the difference in pressure between the inside and outside of a droplet. The Laplace pressure can be represented with the following equation derived from the Young-Laplace equation for a sphere:

$$\Delta P = P_{inside} - P_{outside} = \frac{2\gamma}{R},$$

where  $\Delta P$  is the Laplace pressure,  $P_{inside}$  is the pressure on the inside of the droplet,  $P_{outside}$  is the pressure of the environment on the outside of the droplet,  $\gamma$  is the surface tension on the droplet, and  $R$  is the droplet radius. Therefore, the smaller the radius of the particle, the higher the Laplace pressure becomes, increasing the chances of vaporization and/or coalescence between droplets. In order to prevent destabilization, a dramatic decrease in the surface tension is required to maintain a nano-sized droplet in a favorable manner. Stabilization is usually facilitated with the inclusion of a surfactant, capping agent, or shell. Shell molecules limit surface tension by decreasing the interfacial resistance between the droplet and the surrounding aqueous environment<sup>4</sup>. Furthermore, this shell can prevent vaporization of the droplet at environmental temperatures lower than the boiling point of the PFC. This shell allows the droplet to become super heated without vaporizing, and more readily triggerable as a ultrasound contrast agent.

For ultrasound contrast agents, three types of shells are typically used including lipid, polymer, and protein shells. Lipid shells primarily comprise of phospholipid

bilayers that can also include cholesterol to aid in stability. Lipid shells around PFC droplets are easy to synthesize, bioinert<sup>5</sup>, stable, and are easy to functionalize with targeting moieties and therapeutic cargoes<sup>6</sup>. One interesting ability of lipid shells is to deliver cargoes via “contact facilitated lipid exchange” where the lipid bilayer actually merges with a cell membrane to incorporate their contents within the cytoplasm<sup>7-9</sup>. Lipid shells also have a few disadvantages including low degradation in the body and a shell elasticity that makes vaporization more difficult<sup>10</sup>. Furthermore, targeting moieties have to be added after particle synthesis due to the pressure required to size the particles through an extruder. Polymer shells typically are made of a biodegradable material like poly(lactic-co-glycolic acid)<sup>11-14</sup>. The main characteristic of polymer shells, beyond their biocompatibility and ability to facilitate targeting and encapsulated cargoes, is their stability<sup>11,15,16</sup>. These shells are the most resistant to sonication, as compared to lipid or protein shells<sup>15</sup>. However, for the purpose of PAnDs, vaporization is a key property to control, as well as the relatively complicated synthesis procedures required to make these particles<sup>11,14</sup>. Finally, protein shells are traditionally made with bovine serum albumin<sup>17,18</sup>. Bovine serum albumin is known as one of the most robust proteins, withstanding denaturing at temperature up to 69 °C<sup>19</sup> and pHs between 4.0 and 8.5<sup>20</sup>. Albumin is the most populous protein in blood serum, making it biologically useful and nontoxic. Furthermore, albumin is known to have passive targeting effects toward the surface of cells. The first phase change particles were made with BSA shells as the synthesis method is by far the most simple of all the nanoemulsions. Furthermore, BSA does not interfere with the vaporization process, providing only enough stability to prevent passive vaporization. BSA shells are also easily functionalized with biotin/avidin bridges connected to monoclonal antibodies or other small molecule targeting strategies (see Chapter 7 for more discussion). Each shell type has its advantages and

disadvantages, but when comparing properties for a dual contrast agent that is based on vaporization, bovine serum albumin has the least restriction on vaporization, facile synthesis mechanisms (size is easily controlled by BSA concentration), is biologically compatible, and has the ability to be molecularly targeted and encapsulate therapeutic cargoes. For these reasons, bovine serum albumin was chosen as the shell for PAnDs.

### **2.1.3 Plasmonic Nanoparticles**

While the endogenous contrast resulting from the optical absorption of tissue components allows for photoacoustic imaging contrast (as discussed in Chapter 1), introduction of exogenous contrast agents can produce photoacoustic contrast which is orders of magnitude higher than the intrinsic contrast alone if used in sufficient quantities (as described in Chapter 1). Plasmonic noble metal nanoparticles, primarily made from gold<sup>21–26</sup> and silver<sup>27,28</sup>, are the most frequently used exogenous contrast agents. The localized surface plasmon resonance may be varied by changing synthesis conditions and finely tuning the absorption characteristics, which are determined from the size and shape of the nanoparticle. The synthesis of these nanoparticles is easily controllable to produce a variety of different shapes, including, but not limited to, nanospheres<sup>29–31</sup>, nanoshells<sup>23,31</sup>, nanorods<sup>32–35</sup>, and nanocages<sup>28,36</sup>.

While there are myriad types of plasmonic nanoparticles, one specific type of nanoparticle has been the focus of much research, gold nanorods. This focus is due to the relative biologically inert properties, facile and well developed synthesis methods, peak absorption falling within the near infrared region, application specific tunability allowing for maximum light penetration into the tissues, and the ability to change the functional capping ligands on the surface to control solubility<sup>32,34,37–40</sup>. Beyond the reasons for gold nanorod popularity, they are specifically suited to be used in PAnDs due to their small

size (approximately 40 nm) compared to a perfluorocarbon droplet (approximately 100's of nm), allowing many nanorods to be encapsulated per droplet. Furthermore, to synthesize PAnDs, plasmonic nanoparticles must be dispersed in PFC. Fortunately, several ligand exchange protocols for modification of the surface properties of nanorods have been reported<sup>39,40</sup> that facilitate PFC dispersion. For these reasons, gold nanorods were chosen as the nanoparticle of focus for this research project, although other nanoparticles were examined as mentioned in Section 2.6.

#### **2.1.4 Targeting and Drug Encapsulation**

Beyond PAnD's use as a dual contrast agent, the dual environments provided by the emulsion design allows for further development of the PAnDs system into a targeted, therapeutic cargo delivery vector. In general, PAnDs provide an organic environment in which to encapsulate organically soluble drugs. Some chemotherapeutics, for example, while highly effective *in vitro*, are known for their intense side effects when delivered *in vivo*<sup>41,42</sup>. These negative attributes are not due to the drug itself, but the mechanism for solubilizing them for *in vivo* delivery. Therefore, delivery vectors have been explored that are aqueous in nature, tremendously reducing negative side effects<sup>42-45</sup>. Furthermore, some of these chemotherapeutics show high efficacy when encapsulated within delivery vectors. Specific therapeutic cargoes, namely Paclitaxel, are explored in depth in this work in Chapter 7.

PAnDs can also be functionalized with targeting moieties. The ability to be molecularly specific expands the applications of PAnDs in several ways. First, site specific targeting increases accumulation in diseased tissues allowing for greater concentration and contrast enhancement by PAnDs. Second, site specific targeting allows for combined photoacoustic and ultrasound imaging to be specific to a cell type or

compound, allowing these imaging modalities to aid in noninvasive diagnosis. Third, with targeted drug delivery, negative side effects are shown to be minimized since the drug preferentially accumulates in diseased cells, sparing many surrounding healthy cells<sup>46</sup>. While many strategies could be employed with PAnDs, the targeting strategy explored in this work is a biotin-avidin bridge attached to the BSA surface to link monoclonal antibodies onto PAnDs. These studies are discussed in detail in Chapter 7. PAnD's dual environments allow for further development of their functionality into the targeting, therapeutic cargo delivery realm, making PAnDs multifunctional for detection, diagnosis, and treatment of disease.

## **2.2 PAND FUNCTIONALITY**

The contrast-enhancing functionality and mechanisms of PAnDs' activation are briefly described here. A more in depth study of the physics and characteristic signal produced by PAnDs is discussed in Chapters 3 and 4. PAnDs are a nano-sized agent consisting of a BSA shell and liquid PFC core in which specially capped plasmonic noble metal nanoparticles have been encapsulated (Fig. 2.1) PAnDs are stable because while their nanoscale size increases Laplace pressure, the BSA shell dramatically lowers the surface tension and limits coalescence, thus preventing premature vaporization of superheated PFC from both clinically relevant imaging ultrasound fields and elevated temperatures (up to 50°C for 200 nm diameter droplets as determined by a stability study described in section 2). Therefore, pulsed laser irradiation is used to activate this contrast agent, i.e., to remotely trigger the phase transition of PFC. The PAnDs are vaporized when the encapsulated gold nanorods absorb electromagnetic energy from the laser, providing localized heating and pressure. The photoacoustic transient produced via vaporization is substantially larger than subsequent transients produced from the expelled

plasmonic nanoparticles which undergo thermal expansion under continued pulsed laser irradiation. Furthermore, the resulting gaseous phase also provides increased acoustic impedance mismatch between gas bubbles and the surrounding medium, providing, in essence, optically triggered, ultrasonic contrast enhancement. Overall, PAnDs provide several types of contrast for two imaging modalities: vaporization and thermal expansion contrast mechanisms for photoacoustic imaging and gas-tissue acoustic impedance mismatch for ultrasound imaging contrast.

The clinical usage of PAnDs could be through combined passive and active accumulation effects in oncological applications. First, an intravenous injection would be given to the patient which included PAnDs targeted to a specific tumor type. The particles would be allowed to circulate and accumulate in the tumor interstitial space. Those tumors which have matching receptors would have high retention of the particles, and hence larger contrast. The area with accumulated particles could be imaged as the characteristic signal could be detected from the photoacoustic imaging as well as a morphological localization of the tumor from ultrasound contrast enhancement. These contrast agents could help visualize and diagnose a specific cancer while providing several therapeutic options, including drug delivery, photothermal therapy, and occlusion therapy. Due to PAnDs biocompatibility, they would have limited side effects with their original materials. Perfluorocarbon is exhaled through the lungs with a half life of 72 hours. Bovine serum albumin could potentially cause an immune response, but this could be avoided by using a human serum albumin. Albumin is then broken down in the liver, like other serum proteins, and has a half life of 20 days. Gold has been shown to be non-toxic in several studies<sup>47</sup>, stating that while it does accumulate eventually in the liver and spleen, this accumulation shows limited long term effects on the surrounding tissues.

Overall, PAnDs should be a easy to use and biocompatible contrast agent for both photoacoustic and ultrasound imaging.

### **2.3 POTENTIAL LIMITATIONS**

While many design considerations went into the development of PAnDs, not every limitation was able to be addressed due to the inherent nature of these particles. The first of these limitations is the minimal size of the PAnDs. While PAnDs have been sized down to 100 nm during synthesis, using this small size has a few limitations. First, as we are using gold nanorods that are 40 nm in length, only very few nanorods could be encapsulated into a single droplet. While this is not a concern for the vaporization of the particles (most PAnDs contain less than 10 nanorods each) it is a concern for any potential photothermal therapies or delivery that may be intended to occur. Any additional decrease in the size may also adjust the stability of these particles and make them practically impossible to vaporize through an optical method. Second, the smaller the size of the droplet, the smaller the vaporization signal and the impedance mismatch, limiting two forms of contrast enhancement. While the ultrasound contrast is easily remedied by coalescence of droplets within a sample, the initial vaporization photoacoustic signal is limited by the size. However, 200 nm PAnDs have been used *in vivo* (Chapter 5) and the signal produced was well over the endogenous contrast and easily detectable. Furthermore, it is hypothesized that one would want to used PAnDs under 200 nm due to the limited passive accumulation in tumor interstitial space that would be experienced. It has been shown that particles that are too small, much less than 100 nm, are cleared too quickly to effectively accumulate in tumors. Therefore, the minimal size restriction on PAnDs seems to be of minimal concern for extravasation into

tumor tissues, and above the size restriction that would inhibit any functionality of the particles, and therefore, is not of large concern.

The second limitation is imposed by the use of bovine serum albumin as the shell of the PAnD. Using bovine serum albumin has been shown at times to cause an immune response in humans. However, bovine serum albumin particles have already been approved by the FDA for use in ultrasound contrast agents as the dosage tends to be below the response causing level. Also, bovine albumin could easily be replaced by a human albumin, and no immune response would occur. Therefore, the use of bovine serum albumin induces only minimal limitations, if any.

The final limitation is the ability to load gold nanorods within PAnDs. Using the described method of phase transferring the gold nanorods using a hydrocarbon-thiol chain, only a few (between 5 and 10) gold nanorods will be encapsulated into each nanodroplet. This small loading ability could limit any potential therapies, such as photothermal, that could be employed using PAnDs. However, alternate phase transfer methods, mainly using fluorinated hydrocarbon-thiols as capping agents (Section 2.6), have been developed that greatly increase the gold nanorod loading within each individual droplet, only being limited by the overall size of the droplet and how many gold nanorods can physically fit within one droplet. While this excessive loading will no doubt alter the vaporization and thermal expansion properties of the particles, loading can now be easily adjusted for more therapeutic purposes. Overall, PAnDs are a highly flexible contrast vector that can be adjusted to fit most applications with very few limitations.

## **2.4 FINAL SYNTHESIS PROCEDURE**

The synthesis procedure that is described here is the same method that is followed for every preparation of PAnDs throughout this work. If any modifications were made, perhaps in sizing or sterilization, they are noted specifically in the text. PAnDs are synthesized in several steps. First, gold nanorods with the desired absorption peak were synthesized through a seed-mediated growth mechanism. Next, the gold nanorods underwent a two step ligand exchange to replace the surface ligands so that they could be suspended into the perfluorocarbon phase. Next, the PAnDs were synthesized through an emulsion technique. Finally, the prepared PAnDs were sized using a lipid mini extruder and sterilized via UV light exposure. All these synthesis steps are described in detail below.

### **2.4.1 Materials**

For ease of tracking, all materials will be listed in this subsection with their purchasing vendors. All chemicals were used without additional purification and were at least at ACS grade. Hydroauric acid ( $\text{HAuCl}_4$ ), silver nitrate, ascorbic acid, sodium borohydride, tetrahydrofuran (THF), dodecanethiol, ethanol, bovine serum albumin, and chloroform were purchased from Sigma Aldrich Inc. Poly(ethylene glycol) (mPEG-SH, 5000 Da) was purchased from Laysan Bio. Perfluoropentane was purchased from Fluoromed, Inc. Cetyltrimethylammonium bromide (CTAB) was purchased from Amresco. Polycarbonate sizing membranes and the lipid mini extruder were purchased from Avanti Polar Lipids. Nanopure water was sourced in lab from a Barnstead Nanopure filtration system purchased from Thermo Scientific (18.2 M $\Omega$ -cm).

### **2.4.2 Synthesis of Gold Nanorods**

The first step in synthesis of PAnDs is to make gold nanorods. This procedure was followed for all gold nanorods described in this work. First, the following chemical solutions were prepared. A 0.2 M solution of CTAB in water (11.663 g CTAB in 160 ml of water), a 10 mM solution of gold acid (102 mg  $\text{HAuCl}_4$  in 30 ml water), a 4 mM solution of silver nitrate (10.3 mg of  $\text{AgNO}_3$  in 15 ml of water), a 78.8 mM solution of ascorbic acid (69.5 mg ascorbic acid in 5 ml of water), and a 10 mM solution of sodium borohydride (5.7 mg in 15 ml of water) were all prepared. The CTAB solution was heated to 35 °C to help in dissolution. The gold acid solution should not come into any contact with metal during its preparation. Silver nitrate is light sensitive and was covered in foil. Finally, the sodium borohydrate was kept ice-cold.

First, the growth solution was prepared by adding 80 ml of the CTAB solution, 5.2 ml of the silver nitrate solution, 12 ml of the gold acid solution, 68 ml of water, and 2.0 ml of the ascorbic acid solution, in that order. Next, the seed solution is prepared by mixing 2.5 ml of the CTAB solution with 1.5 ml of a 1 mM dilution of the gold acid solution, and 0.6 ml of the sodium borohydride solution drop-wise. This solution is stirred for exactly 2 minutes at 1200 rpm. Then, 1.6 ml of the seed solution was added to the growth solution and allowed to stir at 400 rpm for 2 minutes only. The gold nanorod solution is left to age overnight.

### **2.4.3 Gold Nanorod Phase Transfer**

To make the gold nanorods soluble in an perfluorocarbon environment, a two-step ligand exchange method<sup>39</sup> was adopted with slight modifications. Specifically, 5 ml of thiolated poly (ethylene glycol) in water (2.0 mg/ml) and 5 ml of as synthesized gold nanorods were sonicated for 2 minutes and left to react at room temperature for 2 hours. The solution was centrifuged at 10,000 rcf for 10 minutes and the supernatant was

removed. The nanorods were redispersed in 5 ml of tetrahydrofuran. Next, 5 ml of ethanolic dodecanethiol (1.0 mg/ml) was added to the THF-nanorod solution and sonicated at room temperature for 30 minutes. The temperature was increased to 50 °C for an additional 60 minutes of sonication. The solution was then left to rest overnight. The solution was centrifuged the next day at 14,000 rcf for 10 minutes and the supernatant was discarded. The dodecanethiol capped nanorods were resuspended in chloroform.

#### **2.4.4 PAnD Emulsion**

To synthesize photoacoustic droplets, first 1 ml of as prepared gold nanorods in chloroform were placed into a 7 ml glass scintillation vial. The organic solvent was completely evaporated, leaving dried nanorods on the bottom of a glass vial. Then, 0.25 ml of liquid perfluoropentane was added to the vial and sonicated for 2 minutes using a bath sonicator. Next, 2 ml of BSA in saline was added (0.2 mg/ml), and the two solutions were sonicated to produce a colored (pink), opaque emulsion of the PAnDs in the water phase.

#### **2.4.5 Sizing and Sterilization**

PAnDs were sized with two methods. First the concentration of BSA in solution was kept at 0.2 mg/ml, as BSA concentration directly affects droplet size. Second, after the synthesis described above, a lipid mini-extruder (Avanti Polar Lipids) was used in correlation with polycarbonate membranes with pore sizes corresponding to the desired final size. Briefly, four filter supports and a membrane were pre-wetted using a buffer solution, and placed into the mini extruder. The unit was assembled as directed by Avanti, and 1 ml of buffer solution was used to fill the empty space in the extruder. Next, 1 ml of as synthesized PAnDs was pushed through the extruder 11 times, making sure to

remove the droplets on the clean side of the extruder. To sterilize PAnDs for use in animals or cells, they were placed under a UV lamp (Longwave , B 100AP) for 20 min.

#### **2.4.6 Characterization**

Several methods and tools were used to characterize the optical and physical properties of PAnDs. First ultraviolet to visible spectrophotometry (UV-Vis) was used to monitor optical absorption properties. Next, transmission electron microscopy (TEM) and cryo transmission electron microscopy (cTEM) were used to quantify nanoparticle loading and location. Additionally, dynamic light scattering was used to determine the size distribution of PAnDs. A water bath heating experiment was used to test stability. The combination of these characterization techniques yielded important information about the optical and physical properties of PAnDs.

##### ***2.4.6.1 Ultraviolet-visible spectrophotometry, Cryo-Transmission Electron Microscopy, and Dynamic Light Scattering***

Three main methods were used to characterize the PAnDs. First, ultraviolet to visible spectrophotometry (UV-Vis, DU640, Beckman Coulter) was used to study the optical extinction of the PAnDs and incorporated plasmonic nanoparticles. PAnDs were synthesized as described above, diluted and optical density was measured in a 1 cm plastic cuvette. Second, dynamic light scattering (DLS, DelsaNano C, Beckman Coulter) was used to determine the size distribution of the nanocarrier agent. PAnDs at synthesized concentration were measured and the resulting size distribution correlated with the pore size of the extruder filter used to size the PAnDs, 200 nm for most experiments. Finally, both transmission electron microscopy (TEM, Hitachi S5500) cryogenic TEM (cTEM, FEI Tecnai G2 F20) were used to image the PAnDs. For traditional TEM the PAnDs were diluted 100 times and then placed on the grid or fixed

with a 2.5% w/v overall concentration of glutaraldehyde for 2 hours, and then rinsed, and place on a TEM grid. For a more accurate image of PAnDs, cryoTEM was used. This method allows visualization of an intact PAnD and the metal nanoparticles within. As prepared PAnDs were diluted by 100 times and placed on holey carbon grids and vitrified in liquid ethane using a Vitrobot™ (FEI) with a 1.0 second blotting time. Samples were rapidly transferred to liquid nitrogen and stored until imaging. Nanoparticle encapsulation was verified by sample stage rotation to view the sample at 0, 45, and -45 degrees. These three forms of nanocarrier contrast agent characterization allowed for study of both physical and optical characteristics.

#### ***2.4.6.2 Ambient Temperature Stability***

To determine at which temperatures PAnDs were stable, a temperature stability study was done. PAnDs were synthesized as described above and placed into 2 ml centrifuge tubes. These tubes were held in a stirred water bath while the temperature was increased slowly over time from 25 to 60 °C. Spectrophotometry readings were taken every 2.5 degrees, and changes in the scattering signal were monitored as indication of particle degradation.

## **2.5 RESULTS AND DISCUSSION**

Design, synthesis, and characterization of PAnDs are all discussed in this chapter. Results are presented from all parts of the synthesis method and characterization of PAnDs through UV-Vis spectrophotometry, cTEM, DLS, and an ambient temperature stability study.

### **2.5.1 Synthesis**

The first step in PAnD synthesis was preparation of gold nanorods. The synthesis procedure was modified from Nikoobakht et. al.<sup>48</sup> and yielded 160 ml of a gold nanorod

solution with the approximate size of 40 nm length by 10 nm diameter (peak absorption at 780 nm) with an optical density of approximately 5 and an overall concentration of  $10^{12}$  nanorods/ml of solution. This synthesis protocol was very sensitive to reaction conditions and small deviations from the method can create large changes in shape and optical absorption properties. It is of vital importance that all reagents be prepared directly before the reaction. Furthermore, the solution would blue shift approximately 30 nm with the overnight rest period. However, these gold nanorods are stable for several months after one rinse. The phase transfer method was a relatively simple and productive method of synthesizing large quantities of gold nanorods.

The second step in the synthesis method was to phase transfer the gold nanorods from the aqueous form as synthesized to the organic phase so that they may be suspended in perfluorocarbons. The described method successfully phase transferred gold nanorods into the organic phase without altering the optical properties (Fig. 2.2b). Therefore, this method is a highly robust procedure to allow gold nanorods to be encapsulated into PAnDs.

The next step was to create the PAnDs via an “oil in water” emulsion technique. This procedure yielded 2 ml of PAnDs with a concentration of  $10^8$  PAnDs/ml of solution. Gold nanorod loading was on average 5 nanorods per droplet as determined by TEM analysis for an overall concentration of  $10^9$  nanorods/ml solution. The final concentrations of components were 0.2 mg/ml bovine serum albumin, 203.75 mg/ml perfluoropentane, and on the order of ng/ml of gold. If the particles were not sized to a specific diameter using a lipid mini extruder, the average size of the particles was approximately 600 nm, with particles going up to several micrometers as determined by DLS. This initial sizing dependence was correlated to the BSA concentration in solution. The lower the concentration of BSA, the smaller the particles were on average. In

general, this synthesis is a facile method to create large quantities of PAnDs and can be up scaled as needed.

Finally, the sizing and sterilization of PAnDs was described. The lipid mini extruder was used to size the PAnDs and results of this process were variable unless two conditions were well controlled. First, the extruder must be very well cleaned with first acetone and then water. The needles must not be bent in any way, and the syringes need to have a good seal. Secondly, if the BSA used in the synthesis of the PAnDs was not relatively fresh, within approximately 2 weeks, the PAnDs did not always survive extrusion. While temperamental in nature, the mini extruder was, in general, an effective sizing method.

### **2.5.2 Ultraviolet-Visible Spectrophotometry, Cryo-Transmission Electron Microscopy, and Dynamic Light Scattering**

After synthesis of PAnDs via an oil-in-water emulsion technique (see methods), several approaches were used to characterize PAnDs. First, cryogenic transmission electron microscopy (cTEM) illustrates the spherical PFC droplets containing plasmonic gold nanorods with an overall size, controlled to approximately 200 nm using an extruding technique (Fig. 2.2a). cTEM imaging also confirmed that the overall diameter and extent of nanoparticle loading can be controlled during the synthesis process. Fig. 2.2c displays a 200 nm PAnD purposefully without any nanoparticle loading, while Fig. 2.2d displays a 200 nm droplet designed to have a lesser extent of gold nanorod loading. Fig. 2.2e displays a PAnD sized to 400 nm with gold nanorod loading. Furthermore, different types of nanoparticles including iron-oxide particles, gold nanospheres, or silver nanoplates, and dyes can be incorporated into PAnDs. A comparison between the cTEM and the glutaraldehyde-fixed TEM samples is shown in Fig. 2.2f. cTEM images show a

much more clear and accurate image of PANDs, but fixed TEM images are useful for their easy of capture and minimal time expenditure.

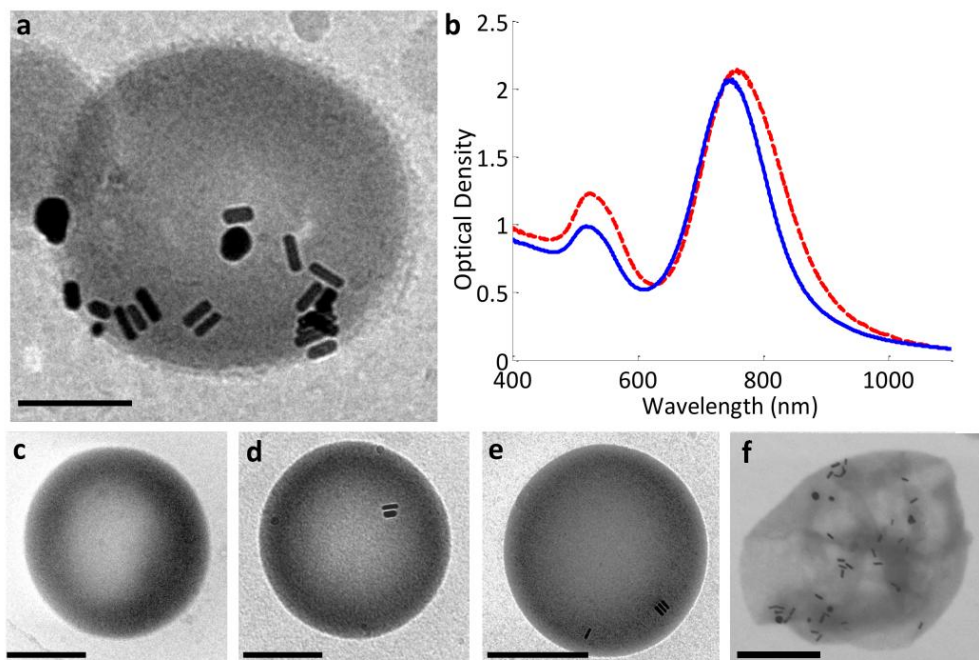


Figure 2.2: (a) Cryogenic transmission electron microscopy (cTEM) image of PANDs. Scale bar, 100 nm. (b) Extinction spectra of as-prepared nanorods (red, dashed line) and nanorods with a modified surface (blue, solid line). (c-e) cTEM images of unloaded PANd and PANds with varying compositions including (d,e) loading with gold nanorods with various sizes (200 nm in panel c and d and 400 nm in panels e and f). (f) Traditional TEM image of PANds dried on carbon grid. Scale bars in c,d, 100 nm. Scale bars in e,f, 200 nm.

Second, spectrophotometry was used to ensure that the surface modification process did not alter the specifically tuned optical properties of the gold nanorods. The “as prepared” and “modified” gold nanorod spectra indicated only very small differences, and therefore the optical properties were not significantly altered during the ligand exchange process. Finally, dynamic light scattering (DLS) was used to confirm sizing

diameters. It was found that the size distributions closely corresponded with the size of the extruder membranes used, for example a 200 nm extruder filter produced PANdS with a size distribution mainly between 200 and 250 nm. A sample size distribution is given in Fig. 2.3 from a light microscopy and analysis via image J software. For a particular imaging or therapeutic application, PANdS can be customized allowing for adjustments of size, loading, and surface functionalization.

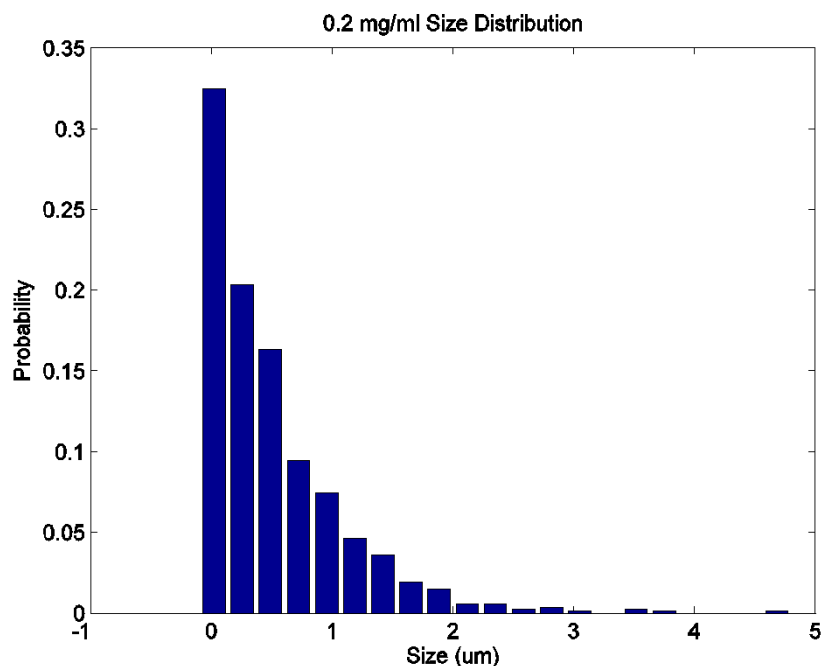


Figure 2.3: Natural size distribution of PANdS made with 0.2mg/ml BSA in water before passage through the miniextruder. A majority of the particles will be naturally size below 1 micrometer due to the concentration of the BSA. The use of the miniextruder removes any larger particles and shifts the spectrum to the left.

### 2.5.3 Ambient Temperature Stability

To determine under which temperatures PANdS are stable, a heated water bath experiment was done. By monitoring the scattering signal as read by the UV-Vis, it was easy to determine changes in concentration and sizing of the PANdS being heated. All

temperatures below 50 °C showed no change in scattering signal, and therefore indicate PAnD stability. Above 50 °C, the scattering signal started to decay, indicating a loss of stability of PAnDs. Therefore, PAnDs are stable in temperatures that would include human body temperature.

## **2.6 ALTERNATE ENCAPSULATIONS AND MODIFICATIONS**

The methods of synthesis described above were followed for all of the experiments used in this dissertation (any exceptions were specifically described in the text). However, other nanoparticles (including gold nanospheres, silver seeds, silver nanoplates, and iron oxide particles) and capping methods (octadecylamine and perfluorodecanethiol) were explored during this process. A few of them are described here along with their limitations.

### **2.6.1 Octadecylamine Phase Transfer**

When initial studies began on PAnDs, a simple phase transfer method from Kumar et. al. (2003)<sup>40</sup> was used to do a single-step ligand exchange on gold nanospheres by attaching a fatty hydrocarbon chain via an amide linkage. All materials were purchased from Sigma. Gold nanospheres were prepared using an ascorbic acid reduction method described by Kumar et. al. (2008)<sup>49</sup>. Silver seeds were prepared in a similar fashion as described by Zou et. al.<sup>50</sup>. Next, a 0.2 mM solution of octadecylamine (ODA) in hexane, 0.539 mg of ODA in 10 ml of hexane, was prepared. Then, in a 7 ml glass scintillation vial 1 ml of as synthesized gold nanospheres or silver seeds was added. Finally, 1 ml of the ODA solution was added on top. The vials were shaken until the nanoparticles moved from the aqueous to the organic phase, as depicted in Fig. 2.3. These particles were washed several times in ethanol and resuspended in hexane.

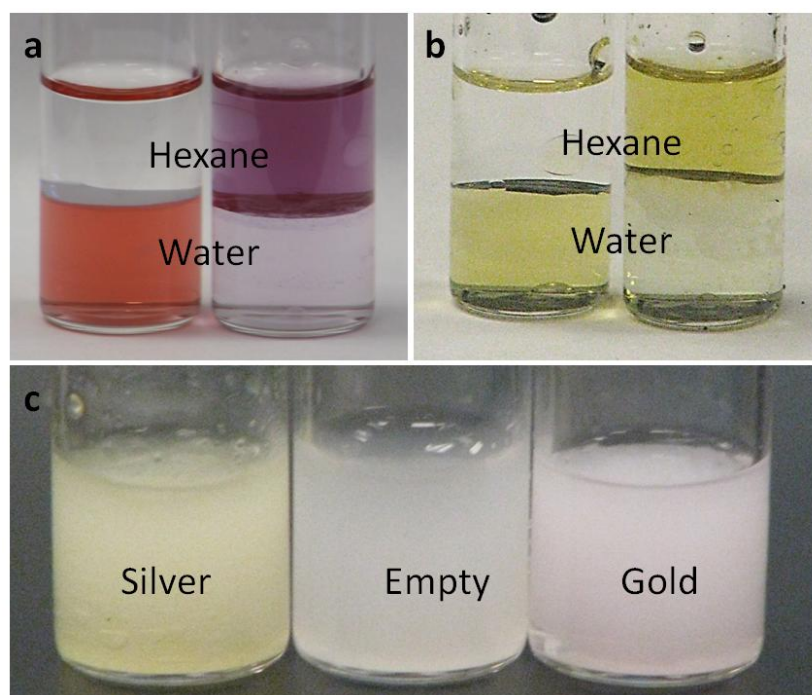


Figure 2.4: (a) Photograph of phase transferred gold nanospheres (20 nm) with the octadecylamine method. (b) Photograph of phase transferred silver spheres. (c) Photograph of PANs with encapsulated silver spheres (left), gold nanospheres (right), and empty (center).

While this method did produce phase transferred nanoparticles, this method was only found to work on relatively stable shapes of nanoparticles, such as spheres. It is shown in Fig. 2.4 that the optical properties did not change upon phase transfer of the spheres. However, a gentler, two-step ligand exchange protocol was needed for gold nanorods or silver nanoplates, as these particles aggregated or dissolved during the single-step phase transfer method. Furthermore, an amide bond is not as strong of a bond as a thiol bond. Therefore, the ODA capping protocol was not the most robust, although it did work for nanospheres particles.

### **2.6.2 Perfluorodecanethiol Phase Transfer**

One of the goals of PANDs was to be able to deliver nanoparticles to provide sufficient passive (thermal expansion) contrast and to aid in therapies such as photothermal. With the above describe hydrocarbon-thiol ligand exchange however, gold nanorod encapsulation was limited to under 10 gold nanorods per droplet. Therefore, a new method to incorporate gold nanorods into perfluorocarbon was developed. Following the same procedure as the hydrocarbon-thiol, a fluorinated hydrocarbon (perfluorodecanethiol) was substituted for the dodecanethiol at a higher concentration of 2 mg/ml. This capping agent led to a successful phase transfer of the gold nanorods into an organic phase, mainly hexane.

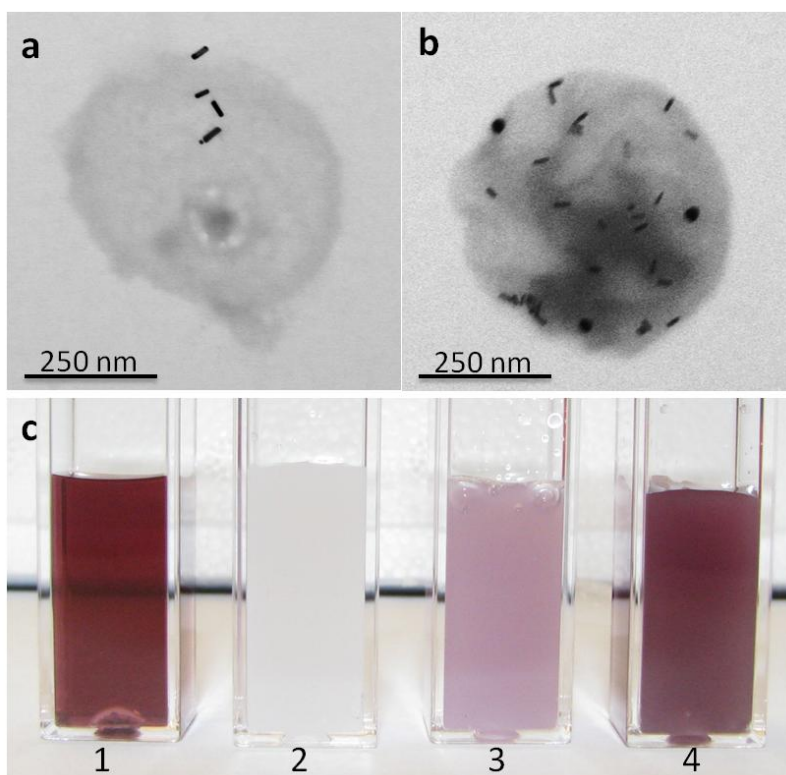


Figure 2.5: (a) cTEM image of a PANd loaded with gold nanorods phase transferred using the dodecanethiol method. (b) cTEM image of a PANd loaded with gold nanorods phase transferred with the perfluorodecanethiol method. (c) Gold nanorods phase transferred with the perfluorodecanethiol method (1). PANds without nanoparticles loading (2). PANds loaded with gold nanorods phase transferred using the dodecanethiol method (3). PANds loaded with gold nanorods capped with perfluorodecanethiol (4).

This procedure dramatically increased the ability to load gold nanorods into PANds. It is hypothesized that the hydrocarbon capping agent was favorable to neither the aqueous or halogenated environment, but slightly favored the perfluorocarbon, so limited loading was achieved. However, the fluorinated hydrocarbon was readily soluble in perfluoropentane, and therefore large amounts of gold nanorods were able to be encapsulated, as shown in Fig. 2.5. When tested for photoacoustic and ultrasound contrast, however, it seems that over loading PANds effectively prevents their

vaporization due to exclusion of PFC. With fine tuning of the gold nanorod concentration added, the fluorinated gold nanorods would all for superior loading ability and would eliminate excess nanoparticle waste.

## 2.7 CONCLUSIONS

Photoacoustic nanoDroplets were designed to be a dual contrast agent for combined photoacoustic and ultrasound imaging, to be biologically compatible and/or bioinert, and to have a straight-forward and easily characterized synthesis. In the end, PAnDs provide a biocompatible design using FDA approved perfluorocarbon droplets and heavily tested gold plasmonic particles. A rapid, straight-forward, and repeatable synthesis method was developed. Furthermore, through characterization it was determined that PAnDs are stable up to 50 °C, are sizeable on the nano scale, and can encapsulate multiple types of nanoparticles. The flexibility of the PAnD platform design allows for easy adaptation to a specific imaging or biological sensing application. In the next chapter, the dual contrast enhancing abilities of PAnDs will be explored.

## 2.8 REFERENCES

1. Yokoyama, M. & Nishihara, M. Perfluorocarbon emulsions and ultrasonic contrast agents containing the same. 13pp. (2010).
2. Dijkmans, P.A. *et al.* Microbubbles and ultrasound: from diagnosis to therapy. *European Journal of Echocardiography* **5**, 245-246 (2004).
3. Sheeran, P.S., Luois, S., Dayton, P.A. & Matsunaga, T.O. Formulation and Acoustic Studies of a New Phase-Shift Agent for Diagnostic and Therapeutic Ultrasound. *Langmuir* **27**, 10412-10420 (2011).
4. Rosen, M.J. *Surfactants and Interfacial Phenomena. Surfactants and Interfacial Phenomena* i-xiii (John Wiley & Sons, Inc.: 2004).doi:10.1002/0471670561
5. Flaim, S.F. Pharmacokinetics and Side Effects of Perfluorocarbon-Based Blood Substitutes. *Artificial Cells, Blood Substitutes and Biotechnology* **22**, 1043-1054 (1994).

6. Unger, E. & Matsunaga, T.O. Lipid coated microbubbles and nanodroplets as tools for biomedical nanotechnology. *Pan Stanford Ser. Biomed. Nanotechnol.* **1**, 749-786 (2011).
7. Crowder, K.C. *et al.* Sonic activation of molecularly-targeted nanoparticles accelerates transmembrane lipid delivery to cancer cells through contact-mediated mechanisms: implications for enhanced local drug delivery. *Ultrasound Med Biol* **31**, 1693-1700 (2005).
8. Wickline, S.A. & Lanza, G.M. Molecular imaging, targeted therapeutics, and nanoscience. *Journal of cellular biochemistry. Supplement* **39**, 90-7 (2002).
9. Winter, P.M. *et al.* Endothelial alpha(v)beta3 integrin-targeted fumagillin nanoparticles inhibit angiogenesis in atherosclerosis. *Arteriosclerosis, thrombosis, and vascular biology* **26**, 2103-9 (2006).
10. Borden, M.A. *et al.* Influence of lipid shell physicochemical properties on ultrasound-induced microbubble destruction. *IEEE transactions on ultrasonics, ferroelectrics, and frequency control* **52**, 1992-2002 (2005).
11. Cui, W. *et al.* Preparation and evaluation of poly(L-lactide-co-glycolide) (PLGA) microbubbles as a contrast agent for myocardial contrast echocardiography. *J Biomed Mater Res B Appl Biomater* **73**, 171-178 (2005).
12. Xu, J.S. *et al.* Synthesizing and binding dual-mode poly (lactic-co-glycolic acid) (PLGA) nanobubbles for cancer targeting and imaging. *Biomaterials* **31**, 1716-1722 (2010).
13. Shive, M.S. & Anderson, J.M. Biodegradation and biocompatibility of PLA and PLGA microspheres. *Adv Drug Deliv Rev* **28**, 5-24 (1997).
14. Straub, J.A. *et al.* Porous PLGA microparticles: AI-700, an intravenously administered ultrasound contrast agent for use in echocardiography. *J Control Release* **108**, 21-32 (2005).
15. Pisani, E. *et al.* Polymeric nano/microcapsules of liquid perfluorocarbons for ultrasonic imaging: physical characterization. *Langmuir : the ACS journal of surfaces and colloids* **22**, 4397-402 (2006).
16. El-Sherif, D.M. & Wheatley, M.A. Development of a novel method for synthesis of a polymeric ultrasound contrast agent. *J Biomed Mater Res A* **66**, 347-355 (2003).
17. Correas, J.M. & Quay, S.D. EchoGen emulsion: a new ultrasound contrast agent based on phase shift colloids. *Clinical radiology* **51 Suppl 1**, 11-14 (1996).
18. Kripfgans, O.D., Fowlkes, J.B., Miller, D.L., Eldevik, O.P. & Carson, P.L. Acoustic droplet vaporization for therapeutic and diagnostic applications. *Ultrasound Med Biol* **26**, 1177-1189 (2000).

19. Michnik, A. *Thermal stability of bovine serum albumin DSC study. Journal of Thermal Analysis and Calorimetry* **71**, 509-519 (Akadémiai Kiadó, co-published with Springer Science+Business Media B.V., Formerly Kluwer Academic Publishers B.V.: 2003).
20. Michnik, A., Michalik, K. & Drzazga, Z. Stability of bovine serum albumin at different pH. *Journal of Thermal Analysis and Calorimetry* **80**, 399-406 (2005).
21. Mallidi, S., Larson, T., Aaron, J., Sokolov, K. & Emelianov, S. Molecular specific optoacoustic imaging with plasmonic nanoparticles. *Opt Express* **15**, 6583-6588 (2007).
22. Oraevsky, A.A., Karabutov, A.A. & Savateeva, E.V. Enhancement of optoacoustic tissue contrast with absorbing nanoparticles. *European Conference on Biomedical Optics, Proc. SPIE* **4434**, 60-69 (2001).
23. Wang, Y. *et al.* Photoacoustic Tomography of a Nanoshell Contrast Agent in the in Vivo Rat Brain. *Nano Letters* **4**, 1689-1692 (2004).
24. Agarwal, A. *et al.* Targeted gold nanorod contrast agent for prostate cancer detection by photoacoustic imaging. *Journal of Applied Physics* **102**, 64701 (2007).
25. Eghtedari, M. *et al.* High sensitivity of in vivo detection of gold nanorods using a laser optoacoustic imaging system. *Nano Lett* **7**, 1914-1918 (2007).
26. Wilson, K., Homan, K. & Emelianov, S. Synthesis of a dual contrast agent for ultrasound and photoacoustic imaging. *Photonics West* **7576**, 75760M (2010).
27. Wilson, K., Homan, K. & Emelianov, S. Photoacoustic and ultrasound imaging contrast enhancement using a dual contrast agent. *SPIE Photonics West* **7564**, 75642P (2010).
28. Homan, K. *et al.* Combined ultrasound and photoacoustic imaging of pancreatic cancer using nanocage contrast agents. *SPIE Photonics West* **7177**, 71771M (2009).
29. Rayford, C.E., Shuford, G. & Schatz, G.C. Optical Properties of Gold Nanospheres. *Nanoscape* **2**, 27-33 (2005).
30. Jennings, T. & Strouse, G. Past, present, and future of gold nanoparticles. *Adv Exp Med Biol* **620**, 34-47 (2007).
31. Lu, W. *et al.* Photoacoustic imaging of living mouse brain vasculature using hollow gold nanospheres. *Biomaterials* **31**, 2617-2626 (2010).
32. Eghtedari, M. *et al.* Functionalized gold nanorods for molecular optoacoustic imaging - art. no. 64370G. *Photons Plus Ultrasound: Imaging and Sensing 2007* **6437**, G4370-G4370 (2007).

33. Chen, Y.-S. *et al.* Enhanced thermal stability of silica-coated gold nanorods for photoacoustic imaging and image-guided therapy. *Opt. Express* **18**, 8867-8878 (2010).
34. Nikoobakht, B. & El-Sayed, M.A. Preparation and Growth Mechanism of Gold Nanorods (NRs) Using Seed-Mediated Growth Method. *Chemistry of Materials* **15**, 1957-1962 (2003).
35. Xiaohua, H., Svetlana, N. & Mostafa, A.E.-S. Gold Nanorods: From Synthesis and Properties to Biological and Biomedical Applications. *Advanced Materials* **21**, 4880-4910 (2009).
36. Yang, X., Skrabalak, S.E., Li, Z.Y., Xia, Y. & Wang, L.V. Photoacoustic tomography of a rat cerebral cortex in vivo with Au nanocages as an optical contrast agent. *Nano Lett* **7**, 3798-3802 (2007).
37. Li, P.C. *et al.* Multiple targeting in photoacoustic imaging using bioconjugated gold nanorods - art. no. 60860M. *Photons Plus Ultrasound: Imaging and Sensing 2006* **6086**, M860-M860 (2006).
38. Kou, X. *et al.* One-step synthesis of large-aspect-ratio single-crystalline gold nanorods by using CTPAB and CTBAB surfactants. *Chemistry* **13**, 2929-2936 (2007).
39. Thierry, B., Ng, J., Krieg, T. & Griesser, H.J. A robust procedure for the functionalization of gold nanorods and noble metal nanoparticles. *Chem Commun (Camb)* 1724-1726 (2009).at <<http://pubget.com/article/19294275>>
40. Kumar, A., Joshi, H., Pasricha, R., Mandale, A.B. & Sastry, M. Phase transfer of silver nanoparticles from aqueous to organic solutions using fatty amine molecules. *J Colloid Interface Sci* **264**, 396-401 (2003).
41. He, L., Wang, G.L. & Zhang, Q. An alternative paclitaxel microemulsion formulation: hypersensitivity evaluation and pharmacokinetic profile. *Int J Pharm* **250**, 45-50 (2003).
42. Rowinsky, E.K. & Donehower, R.C. Paclitaxel (taxol). *N Engl J Med* **332**, 1004-1014 (1995).
43. Gao, P. *et al.* Development of a supersaturable SEDDS (S-SEDDS) formulation of paclitaxel with improved oral bioavailability. *J Pharm Sci* **92**, 2386-2398 (2003).
44. Danhier, F. *et al.* Paclitaxel-loaded PEGylated PLGA-based nanoparticles: in vitro and in vivo evaluation. *J Control Release* **133**, 11-17 (2009).
45. Tartis, M.S. *et al.* Therapeutic effects of paclitaxel-containing ultrasound contrast agents. *Ultrasound Med Biol* **32**, 1771-1780 (2006).
46. Lanza, G.M. *et al.* Acoustic molecular imaging and targeted drug delivery with perfluorocarbon nanoparticles. *AIP Conf. Proc.* **754**, 120-123 (2005).

47. Lewinski, N., Colvin, V. & Drezek, R. Cytotoxicity of nanoparticles. *Small* **4**, 26-49 (2008).
48. Nikoobakht, B. & El-Sayed, M.A. Preparation and growth mechanism of gold nanorods (NRs) using seed-mediated growth method. *Chemistry of Materials* **15**, 1957-1962 (2003).
49. Kumar, S., Aaron, J. & Sokolov, K. Directional conjugation of antibodies to nanoparticles for synthesis of multiplexed optical contrast agents with both delivery and targeting moieties. *Nat Protoc* **3**, 314-320 (2008).
50. Zou, X., Ying, E., Chen, H. & Dong, S. An approach for synthesizing nanometer- to micrometer-sized silver nanoplates. *Colloids and Surfaces A: Physicochemical and Engineering Aspects* **303**, 226-234 (2007).

## **Chapter 3: Preliminary Testing of Combined Ultrasound and Photoacoustic Contrast Enhancement**

The previous chapter showed that Photoacoustic nanoDroplets (PAnDs) can be synthesized and characterized reliably. Chapter 3 focuses on the preliminary testing of PAnDs to determine their contrast enhancing abilities, their efficiency over the widely used photoacoustic contrast agent, gold nanorods, and to determine if their provided contrast is sufficient to be used in tissues. Due to the use of vaporization as a contrast mechanism, PAnDs should produce a characteristic signal of high initial signal, followed by decay to a steady state level. These experiments were used to show feasibility of PAnDs for further use in *in vivo* experimentation described in Chapter 5. The descriptions of the imaging systems, experimental setups, and data analysis techniques are explored in this chapter as well as reasoning for their usage.

### **3.1 TISSUE MIMICKING PHANTOMS**

In order to study the contrast enhancing properties of PAnDs, a well controlled and understood environment, in terms of optical, acoustic, and geometric properties, needs to be used during imaging experiments. These environments, called tissue-mimicking phantoms, can be made in several ways, the most popular of which for ultrasound and photoacoustic imaging includes poly(vinyl alcohol) (PVA), gelatin, and poly(acrylamide) (PAA) based phantoms. PVA phantoms are made by mixing PVA chains of a specified molecular weight with water, pouring the solution into the desired mold, and set using two freeze and thaw cycles<sup>1</sup>. This temperature cycling increases the turbidity of the gel while also increasing rigidity. In general, PVA has limited optical absorption in the visible to near infrared wavelength range, optical scattering properties similar to those of tissues with the inclusion of special optically scattering materials, and

has ultrasound attenuation and speed similar to that of water, hence similar to those of tissues<sup>2,3</sup>. While PVA phantoms do provide an environment similar to that of tissues, PAnDs do not maintain stability during freeze-thaw cycles due to denaturing of the bovine serum albumin (BSA) shell. Therefore, PVA phantoms are not applicable for use with PAnDs.

Another typically used phantom is made of gelatin. Gelatin phantoms are synthesized by heating gelatin and water up to 50 °C and then combining the mixture with formaldehyde to improve its long-term stability<sup>4,5</sup>. Finally, the solution is placed in a vacuum to remove air bubbles that were incorporated during mixing. To adjust optical and acoustic properties of gelatin to be more similar to tissue, scattering particles (colloidal graphite<sup>6</sup> or silica<sup>7</sup>, Intralipid® solution<sup>8</sup>, or polystyrene beads<sup>9</sup>) and absorption-inducing agents (dyes, nanoparticles) are often added. Gelatin phantoms are highly versatile; however, PAnDs cannot withstand the inclusion of formaldehyde due to the BSA shell or the placement into a vacuum as this would cause vaporization of the agents.

Poly(acrylamide) (PAA) phantoms provide a solution for these synthesis problems. PAA phantoms are synthesized entirely through chemical reaction, meaning no freezing or heating is required. Furthermore, optical and acoustic properties can be regulated by controlling the synthesis reagents or adding supplemental scattering or absorbing particles. As a hydrogel, PAA phantoms have acoustic properties similar to those of tissue<sup>3,10</sup>. PAA phantoms are synthesized as follows; all materials were purchased from Sigma. A 10% PAA solution in water was made. Next, a 10% w/v solution of ammonium persulfate (APS) was added by 10 µl per 1 ml of phantom volume. Finally, tetramethylethylenediamine (TEMED) was added by 1 µl per 1 ml of phantom volume. This solution was gently swirled and poured into the desired mold. These phantoms took

approximately 10 mins to crosslink, and were stored with a water layer covering them to prevent drying<sup>10</sup>. Before crosslinking, PAA phantom reagents are toxic, and therefore these phantoms should be prepared in a fume hood with full chemical protection gear. By adjusting concentrations of PAA, APS, and TEMED several properties can be adjusted. Adding more PAA, for example a 12 or 15% solution, creates a stiffer gel. Adding more APS, for example 12 – 15  $\mu\text{l}$  per ml of volume creates a stiffer gel and decreases the pore size in the phantom. Increasing the TEMED (1.5 – 2  $\mu\text{l}$  per ml of volume) rapidly increases crosslinking time. Overall, PAA phantoms provide an excellent environment to study PANs which take only minutes to make, and have highly adjustable acoustic and optical properties. Throughout the work, PAA phantoms were made using the above method and used to study PANs.

### **3.2 PHOTOACOUSTIC AND ULTRASOUND IMAGING SYSTEMS**

Due to the complementary equipment shared for ultrasound and photoacoustic imaging modalities, imaging setup typically only requires an ultrasound system capable of operating in pulse-echo and echo only modes triggered by a pulsed laser. The Ultrasound Imaging and Therapeutic Research Laboratory has access to several such systems, and therefore multiple dual imaging setups can be used. Explored here are two ultrasound systems generally used for data acquisition (WP64 and Vevo2100) and a description of parameters of several laser systems and light delivery methods used throughout this research.

#### **3.2.1 WP64 by WinProbe**

Preliminary experiments were all accomplished using a WP64 ultrasound imaging system from WinProbe Corporation. This system has 64 data acquisition channels and can be coupled with several lower frequency transducers including a 5 MHz center

frequency, 14 mm, 128 element transducer which was used for all WinProbe experiments discussed here. The WP64 is highly useful for research purposes due to the direct access to the raw radiofrequency (RF) data collected by the machine. However, this feature limits the frame collection speed to 3.3 Hz, even after being specifically adjusted to collect frames in the phase array mode using only the center 64 elements of the transducer. This limitation has been addressed in newer versions of WinProbe systems. For delivering the pulsed laser light to the sample, a custom built system consisted of a 19 fiber bundle system that surrounded the transducer with a focus approximately 2 cm below the transducer surface.

### **3.2.2 Vevo2100 by Visual Sonics**

The main ultrasound system used in this research was the Vevo2100 system by VisualSonics. This platform was specifically designed with *in vivo* animal research in mind as it provides high resolution images through the use of several high frequency transducers including the MS250 with a center frequency of 21 MHz and the MS550D with a center frequency of 40 MHz. The MS550D transducer allows for an axial resolution down to 30  $\mu\text{m}$ . Light is coupled to the sample via a set of VisualSonics-built optical fibers. Thousands of individual fibers are gathered together and randomly organized to two rectangular outputs, one placed on either side of the transducer with a custom holder. This arrangement gives even illumination regardless of the input beam profile. The fibers themselves can withstand very high laser fluence ( $>100 \text{ mJ/cm}^2$ ). The output beam from the fiber bundle focuses the light approximately 1 cm from the surface of the transducer. These attributes ensured high imaging resolution and sensitivity and therefore, most experiments and all *in vivo* experiments used the Vevo2100 for data acquisition.

### **3.2.3 Lasers**

Several lasers were used to produce photoacoustic transients in this research. First, a pulsed Nd:YAG laser from OPOTEK coupled with an optical parametric oscillator (OPO) tunable in the near infrared (NIR) wavelength range allowed for usable wavelengths from 675 to 950 nm. The OPOTEK laser operated at 10 Hz with a 4-6 ns pulse duration. While the OPOTEK laser was highly useful for many applications, its limited wavelengths prevented its use in the longer wavelength range. Therefore, a Spectra-Physics (SP) Nd:YAG pulsed laser coupled with an OPO was used for a majority of the research here. The SP laser is tunable in wavelengths ranging from 355 to 3000 nm, pulsed at 10 Hz with a 5-7 ns pulse duration. For a few experiments, described more in Chapter 4, a continuous wave diode laser that emitted at 808 nm was used to determine physical properties of PAnDs.

A Ophir power meter (head model: PE50BB with meter style: Nova II) was used to measure the energy of the pulsed laser beam. Laser burn paper was used to determine the beam profile over the sample. Laser fluence was calculated by dividing the energy by the area of the illumination.

### **3.3 DATA ANALYSIS**

The combined ultrasound and photoacoustic imaging systems are responsible for collecting data; much effort went into processing and analyzing them into useful data. The following section outlines the data processing methods from raw RF or in-phase (I) and quadrature (Q) data. Furthermore, due to the dynamic nature of signals produced by PAnDs, special normalizing and referential techniques were developed to allow data comparison. Unless otherwise mentioned, these techniques were followed for post acquisition data processing.

### **3.3.1 Photoacoustic and Ultrasound Image Processing**

The general process for creating ultrasound and photoacoustic images is well known. In a typical signal processing procedure, the raw RF signals are beamformed using a delay and sum technique (dynamic receive focusing) to co-register various signals received by the different transducer element, a Hilbert transform is taken to find the overall amplitude of these signals, and then the image is displayed in a logarithmic scale to help visualize the back scattered acoustic signal in a large dynamic range. Photoacoustic images are displayed in linear scale because they contain not as great of signal differences as in ultrasound imaging.

The image processing methods for each imaging system did not alter much in this research save a few exceptions. The WinProbe imaging system allows direct collection of RF data, allowing the above described process to occur as stated. The Vevo2100, however, collects a downsampled form of RF data called in-phase and quadrature (IQ) data which is beamformed automatically by the system. For ultrasound images, the IQ data is used as is and the square root of the summed squares is taken and normalized. The image can then be displayed in a log scale adjusting the dynamic range through the colormap settings. Photoacoustic data is processed slightly differently. The IQ data is reverse processed to produce a version of the original RF data. This data can then be beam formed, Hilbert transformed and displayed in a linear scale. These image processing methods were used on all images and data shown in this work depending on which ultrasound system was used (noted in each experiment).

### **3.3.2 Photoacoustic and Ultrasound Frame Reference**

Since the PAnD is a dynamic particle that produces a time-varying signal, most of the photoacoustic and ultrasound images were taken in a sequence, up to 500 frames. Since the data were processed after acquisition, it was a challenge to keep all images in

the same relative colormap scale, leading to misleading images in terms of signal dynamics. Therefore, in all data sets the absolute maximum and minimum pixel values in all frames were determined and set as pixels (1,1) and (1,2), respectively, when making images. This ensured that all frames were comparable to each other in terms of color assignment and intensity, providing accurate representation of signal change over time. All photoacoustic and ultrasound images shown in this work have been processed with the aforementioned technique and are, therefore, comparable.

### **3.3.3 Frame Comparison and Graph Production**

To visualize the dynamic signal produced from PAnDs over hundreds of frames, graphs are produced throughout this work. These graphs are generated in two ways. The generated graphs are the summed intensity of either the entire image frame or a user-defined region of interest within the image frame. Summing the entire image has the disadvantage of including more background signal which minimizes the overall signal change. However, for phantom studies which have limited background signal, this processing produces a fairly accurate representation of signal progression. For studies with higher optically absorbing and scattering environments, i.e. mouse experiments, the specific region of interest method was used. Due to animal motion (heart beat and respiration) and migration of PAnDs out of the specified region of interest, this method also had limitations. Therefore, motion artifacts were removed from graphs by correlating the movement within the ultrasound frames. However, not all motion artifacts could be removed which contributes to variance in the signals. The method used in each experiment is noted in the methods section.

### 3.4 METHODS

Four experiments were performed to determine several aspects about the signal and contrast enhancement provided by PAnDS. First, a tissue mimicking phantom with an inclusion of PAnDs was imaged to determine the characteristic signal and contrast enhancement. Next, a phantom homogenously laden with PAnDs was imaged to determine the optically specific activation of PAnDs into their contrast enhancing state. Then, in order to compare PAnDs to the traditional photoacoustic contrast agent, gold nanorods, a study comparing relative gold nanorod concentrations was implemented. Finally, to demonstrate that PAnDs provide sufficient signal to overcome the endogenous contrast of tissues, an *ex vivo* mouse experiment is shown. These experiments provided support that not only do PAnDs provide dual ultrasound and photoacoustic contrast, they do so in a characteristic fashion that is feasible for *in vivo* use.

#### 3.4.1 Characteristic Signal of Photoacoustic nanoDroplets

In order to determine the ultrasound and photoacoustic contrast enhancement properties of the nanodroplet contrast agent, a series of phantom experiments were performed. Phantoms consisting of PAnD suspensions of known concentrations were placed within phantoms of a 10% polyacrylamide solution and used for *in vitro* characterization studies. These phantoms were prepared in a two-step procedure. First, the outside portion of the phantom which acts as background signal was prepared as previously described. The phantom was left to crosslink for approximately 5-10 minutes. Next, the inclusion in the phantom which contained the nanocarrier contrast agent was prepared. A cylindrical inclusion was created through the phantom with the desired nanocarriers as shown in Fig. 3.1 (experimental setup). The inclusion consisted of the nanocarriers added the same 10% polyacrylamide solution in a 1:20 volume ratio, giving a final nanocarrier concentration of  $5 \times 10^8$  nanocarriers/ml. The preparation was left to

crosslink for approximately 10 minutes at which point the phantoms were ready for imaging.

One phantom was used for US imaging and confirmation of vaporization through optical microscopy, while the other was used for US/PA combined imaging. Each phantom was placed into the water bath. US images were taken with a WP64 ultrasound imaging system (Winprobe, USA) using a 7 MHz, 128 element transducer before and after 60 seconds of laser irradiation. The transducer was positioned on the phantom with imaging plane perpendicular to the longitudinal axis of the inclusion. Pulsed laser irradiation, delivered from an optical window on the side of the water bath, was used to trigger the contrast agent. This irradiation was produced by a pulsed Nd:YAG laser pumped OPO (Opotek, USA) tuned to 780 nm, the peak absorption of the encapsulated nanorods. The pulse repetition frequency of the 5-ns laser was 10 Hz, the fluence of the laser beam was 5 mJ/cm<sup>2</sup>. The laser beam was parallel to the imaging plane and perpendicular to the inclusion. This setup is shown in Fig. 3.1.

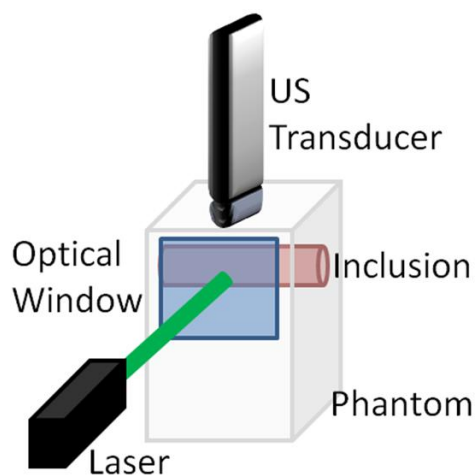


Figure 3.1: Depiction of experimental set up. The PAA phantom has been prepared with a horizontal, cylindrical inclusion. It is placed in a water bath with an optical window. A laser air-beam intersects the inclusion perpendicularly. The US transducer sits above the phantom, in the same plane as the air-beam perpendicular to the inclusion. The air-beam interacts with only half of the inclusion

In the first phantom undergoing US imaging only, the beam was positioned to irradiate only the bottom half of the inclusion. Following, laser irradiation, this phantom was dissected for optical microscopy (Leica, USA). The second phantom was used for US/PA imaging, where the laser beam was positioned to irradiate only the top half of the inclusion. PA signals were acquired with each laser pulse, stored and processed off-line using conventional ultrasound and photoacoustic image reconstruction techniques for array-based systems as described previously.

### 3.4.2 Selective Optical Triggering of Photoacoustic nanoDroplets

In order to show optically specific activation, a phantom experiment was performed using a phantom homogeneously laden with PAnDs, in which only specific points were activated using laser irradiation. More specifically, PAnDs were incorporated into a 10% polyacrylamide hydrogel phantom in a 1:20 volume ratio of agent to

polyacrylamide solution for a final concentration of  $5.5 \times 10^6$  PAnDs/ml. The phantom was positioned in a water bath and imaged using a 7 MHz, 1.4 cm aperture, 128 element, linear array transducer from the Winprobe system. A tunable laser system (optical parametric oscillator pumped by a Q-switched pulsed Nd:YAG laser, Opotek) operating at 780 nm wavelength light,  $5.0 \text{ mJ/cm}^2$  pulse energy, 10 Hz pulse repetition rate, and 5-7 ns pulse duration, was used to irradiate the phantom perpendicular to the imaging plane at 28 different locations for 60 seconds. This setup is similar to part 3.4.1, except the ultrasound transducer is turned 90 degrees to image perpendicular to the direction of the air beam. Ultrasound radiofrequency signals were collected before and after each laser irradiation application. Photoacoustic radiofrequency signals were collected during laser irradiation. Ultrasound and photoacoustic images were reconstructed retrospectively from the captured data. Specifically, the radiofrequency ultrasound signals collected at each transducer were Hilbert transformed and beamformed, and then the amplitude of the signal was scan converted and displayed using either a linear (photoacoustic) or logarithmic (ultrasound) scale (20dB). To form photoacoustic images displaying photoacoustic response from all 28 laser beam positions, photoacoustic images at each individual position were normalized and then the entire image set was added to produce the final photoacoustic image.

### **3.4.3 Photoacoustic nanoDroplets Efficiency**

To determine the photoacoustic signal produced from varying concentrations of PAnDs, compared to an equivalent concentration of gold nanorods, experiments were conducted using 40 nm by 10 nm nanorods which have an absorption peak at 780 nm. A thin, 0.2 mm diameter, glass tube was suspended in a water cuvette, and known concentrations of either PAnDs (containing of 0.25, 0.125, and 0.0625 fraction of the

original, as-prepared concentration of nanorods) or nanorods alone (1.0, 0.5, and 0.25 of the original concentration) were injected into the sample tube. A pulsed (10 Hz, 5-7 ns pulse duration) laser beam was used to irradiate the sample with 780 nm light at 5 mJ/cm<sup>2</sup> from the side. Photoacoustic signal was collected using a 7.5 MHz, single element ultrasound transducer positioned above the sample in the water tank. Peak signal was averaged for three samples per condition, and plotted using error bars representing one standard deviation.

#### **3.4.4 Signal Contrast in Tissue**

While PAnDs produce signal in phantoms, their activity in tissue needed to be explored before animal experiments could be done. Therefore, an *ex vivo* mouse imaging experiment was completed. Scrap mice (Nu/Nu, female, 3-5 months old) were sacrificed immediately before imaging via carbon dioxide asphyxiation and cervical dislocation. Animals were immediately placed in a water tank and three-dimensional US and spectroscopic PA imaging scans of the *ex vivo* mouse spleen were acquired using a Vevo2100 US imaging system (40 MHz, 256 element transducer) and a pulsed, Nd:YAG laser tuned with an OPO. The laser system operated at 10 Hz PRF, 5-7 ns pulse width, and 10 mJ/cm<sup>2</sup> fluence. Under ultrasound guidance, 100  $\mu$ l of PAnDs (10<sup>7</sup> PAnDs/ml) were approximately injected into the mouse spleen in the lower left lobe, a normally hypoechoic organ. Next, with a single imaging plane in the center of the spleen, interleaved photoacoustic and ultrasound images were captured at 3.3 Hz for 60 seconds (200 frames). The first several frames were captured with the laser beam blocked to allow capture of noise levels and to ensure detection of the first laser pulse exposure. Frames were processed after capture as previously discussed, and graphs of ultrasound and photoacoustic signal intensity were created by summing signal over the entire image.

## **3.5 RESULTS AND DISCUSSION**

### **3.5.1 Characteristic Signal of Photoacoustic nanoDroplets**

The US and PA images of the phantom with an inclusion containing the remotely triggered, dual contrast agent are shown in Fig. 3.2 and 3.3. The US image before laser irradiation shows the boundaries of the inclusion; this is due to a slight acoustic impedance mismatch between the inclusion and background, as well as some bubbles at the boundaries and within the inclusion which were created during phantom preparation. The interior of the inclusion shows very little US signal before laser irradiation. In the orientation of these images, the laser beam enters the phantom from the left side. After laser irradiation for 60 seconds, another US image was taken. The image shows strong contrast enhancement in the lower half of the inclusion, where the laser beam was incident upon the phantom. The liquid-to-gas transition of PAnDs is illustrated in the optical images in Fig. 3.2. The right panel of Fig. 3.2 contains light microscopy images of PAnDs suspended in the hydrogel block. The hydrogel was irradiated with a pulsed laser beam and additional optical images were taken. Initially gas bubbles are approximately 1  $\mu\text{m}$  in diameter upon vaporization. The large size of gas bubbles appearing after irradiation is due to coalescence of several individual microbubbles in close proximity.

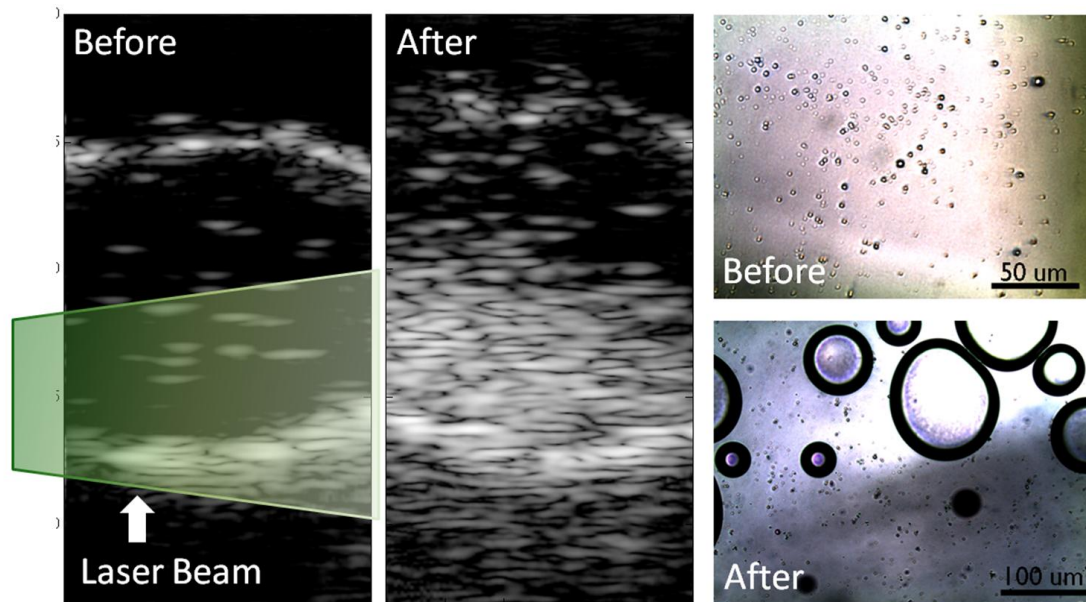


Figure. 3.2: Left: US image of the phantom before laser irradiation showing boundaries of the inclusion containing the contrast agent. The shaded trapezoid indicated the approximate path of the laser beam. Center: US image of the inclusion after laser irradiation. Right, top: Optical microscopy images of the photoacoustic droplets within the PAA phantom. Right, bottom: Vaporized contrast agent. Each ultrasound image is 3 cm tall by 1 cm.

Ultrasound and photoacoustic images from the second phantom are shown in Fig. 3.3. In response to the first laser pulse, there is a significant PA response from the part of the inclusion irradiated with pulsed laser beam. Over time (i.e., with subsequent laser pulses), the intensity of photoacoustic signal decreases (Fig. 3.3 c-k). The ratio between the highest and lowest photoacoustic signal intensities represents a 17 dB increase in signal. Ultrasound images (Fig. 3.3 a and l) confirm the formation of gas bubbles through increased ultrasound contrast.

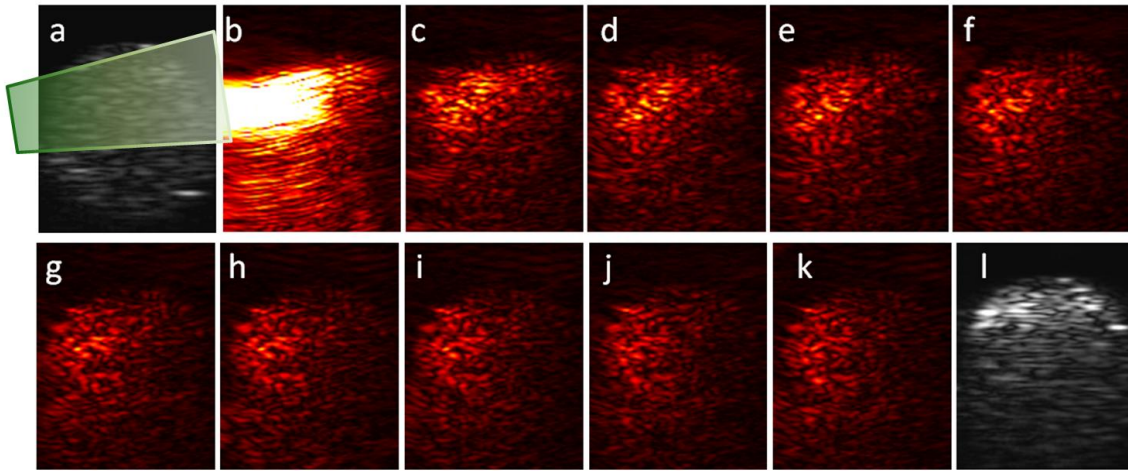


Figure 3.3: **(a and l)** Ultrasound images before and after laser irradiation of inclusion containing the nanocarrier contrast agent. Green shape represents approximate air beam path. **(b-k)** Consecutive PA signal captured over 30 seconds

The developed, remotely triggered, dual contrast nanoagents – photoacoustic droplets (PAD), have a simple and versatile synthesis and have been shown to improve US and PA contrast simultaneously once remotely triggered. Only areas where light was applied showed vaporization of the contrast agent. Once the laser was turned on, there was a dramatic increase in photoacoustic signal magnitude due primarily to the rapid, laser triggered vaporization of PAnDs. As laser irradiation continued, and the supply of PAnDs was depleted, the photoacoustic signal decayed to its steady-state level corresponding to the thermal expansion of the expelled gold nanorods. In biological tissue, unlike the case of the hydrogel phantom, thermal expansion from endogenous optical absorbers will also contribute to the photoacoustic signal. As presented in Fig. 3.4, the PA signal dramatically decreases over time. The initial signal due to vaporization, as well as the persistent increased signal due to thermal expansion demonstrates the dual PA signal production phenomena. The use of vaporization for PA signal production in a biological setting is exciting as it is associated with stronger signal

generation, allowing for deeper depth of imaging and lower potential cytotoxic effects while using plasmonic noble metal nanoparticles.

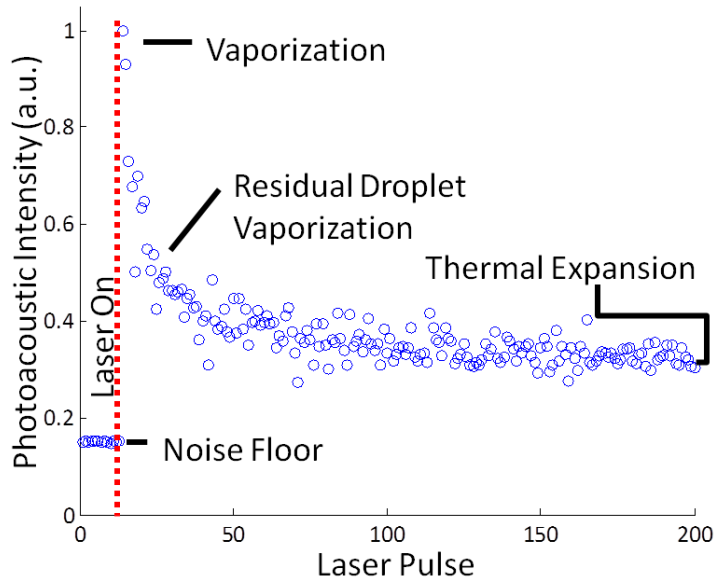


Figure 3.4: Analysis of photoacoustic signal intensity. In each PA frame, the total summed PA intensity is represented, and decays over time.

### 3.5.2 Selective Optical Triggering of Photoacoustic nanoDroplets

To show optical activation selectivity, a phantom underwent pulsed laser irradiation in several locations (28 total) where photoacoustic signals were captured for each laser pulse. These locations were strategically placed to “write” the letters “U” and “T.” Once the vaporization of PAnDs was initiated, the generated gaseous phase of the PFC had a significant acoustic impedance mismatch with the surrounding environment, thus acting as an ultrasound contrast agent as shown in the grown ultrasound pictures in Fig. 3.5. During the photoacoustic imaging experiment, ultrasound signals were collected before and after each laser application. With point-by-point optical laser activation of PAnDs, the ultrasound contrast appears at the corresponding positions of the laser-PAnD

interaction (Fig. 3.5) due to an ultrasound pulse backscattered from PAnD generated microbubbles.

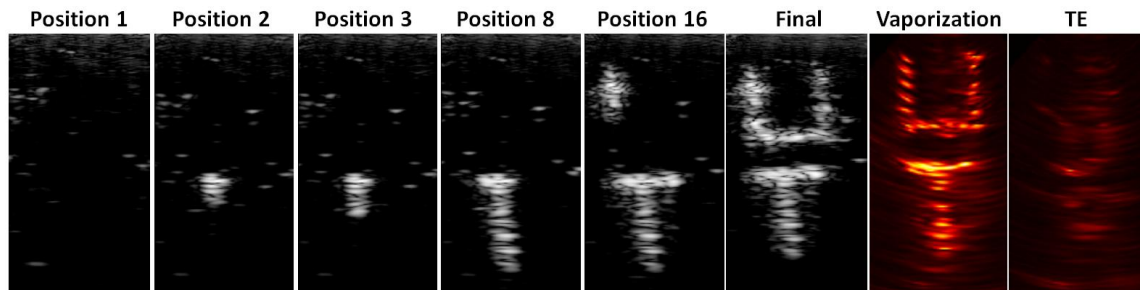


Figure 3.5: Position 1 through 16 and final represent the progression of applied laser positions within the phantom. As PAnDs are activated, they “write” the letters “U” and “T”. The corresponding photoacoustic signals (vaporization and TE panels) represent signals from the initial vaporization and the long term thermal expansion.

The reconstructed photoacoustic images of the phantom (Fig. 3.5) confirm that under the same laser fluence, vaporization of PAnDs results in a stronger photoacoustic signal compared to nanorod-assisted photoacoustic signal generated by thermal expansion alone (Fig. 3.5 right two panels). The vaporization-based photoacoustic image displays a signal-to-noise ratio (SNR) of 7.3 dB, while the thermal expansion-based photoacoustic image displays a SNR of 1.3 dB. Furthermore, the averaged photoacoustic signal amplitude increase from all 28 positions is approximately 13 times, or 22 dB, higher than the thermal expansion signal, with a maximum reaching 66 times, or 37 dB, higher. Interestingly, there is a difference in resolution between the vaporization and thermal expansion based images. The vaporization image clearly shows differences in spot where laser irradiation was applied, while the thermal expansion image shows no differentiation. This is likely due to the presence of the perfluorocarbon gas bubbles either scattering the light (and therefore decreasing thermal expansion based

photoacoustic signal) or scattering the sound (and therefore scattering the thermal expansion based photoacoustic signal). Therefore, the presence of gas bubbles make affect the resolution of the prolonged, thermal expansion-based, photoacoustic images. Therefore, laser-induced vaporization of the PAnDs produced a significantly stronger photoacoustic signal than that of thermal expansion.

### 3.5.3 Photoacoustic nanoDroplets Efficiency

When comparing the signal production of PAnDs versus gold nanorods, it was shown that for the same relative concentration of gold nanorods (i.e. gold nanorods versus the same number of gold nanorods loading into PAnDs), the signal produced from PAnDs is an order of magnitude higher than that produced by the gold nanorods along as shown in Fig. 3.6. Importantly, the results of the phantom experiment indicated that the same amplitude of the photoacoustic signal can be obtained with lower concentrations of gold nanorods inside of PAnDs compared to a higher concentration of gold nanorods alone.

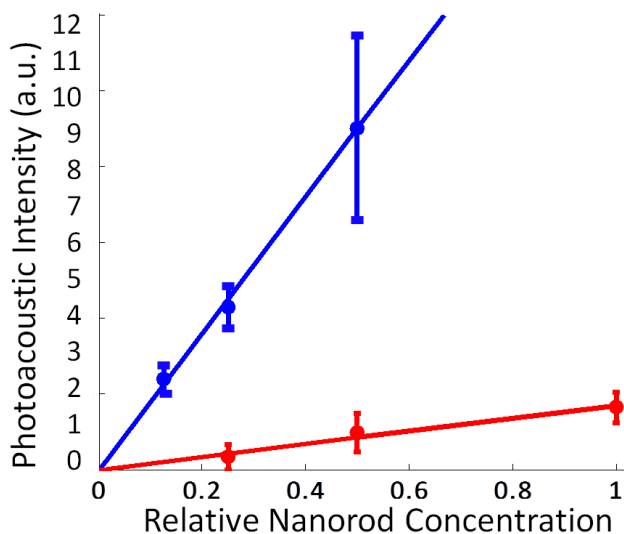


Figure 3.6: Graph showing the signal difference between gold nanorods (red line) and PAnDs (blue line) loaded with the same concentration of gold nanorods.

### 3.5.4 Signal in a Tissue Environment

It is important to ensure that the contrast enhancement and characteristic signal produced from PAnDs in tissue mimicking phantoms is similar to how PAnDs would behave in tissues. Therefore, an *ex vivo* mouse imaging experiment was done. PAnDs were injected into a mouse spleen and immediately imaged. Photoacoustic images (shown in Fig. 3.7) show that the initial signal from the area above the spleen, as PAnDs tended to “leak” away from the injection site, was significantly higher (approximately 50%) than the signal acquired from the same spot after 200 imaging frames when summing the intensity over the entire image. This signal correlates with the characteristic vaporization followed by thermal expansion signal previously shown by PAnDs as shown in the graph in Fig. 3.7. Furthermore, even using a low laser fluence, these signals are higher than the endogenous signal in the spleen area, a highly blood filled organ. When examining the waveform from the photoacoustic signal from the middle of the highest signal area from the 8<sup>th</sup> frame and comparing it to the 100<sup>th</sup> frame, interesting differences can be seen (as shown in Fig. 3.8). The initial frame has much higher signal amplitude than the following frames. Furthermore, the noise levels before and after the signals are the same between the signal frames.

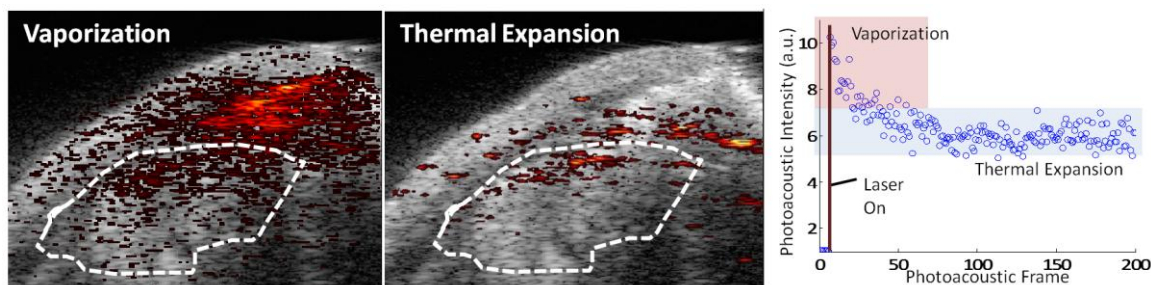


Figure 3.7: Left and middle, Photoacoustic images of peak vaporization signal and prolonged thermal expansion signal of PANDs. The white dashes outline the spleen, however most signal is seen above the spleen. Right, graph showing decrease in photoacoustic intensity with continued pulsed laser irradiation correlating with the characteristic signal of PANDs.

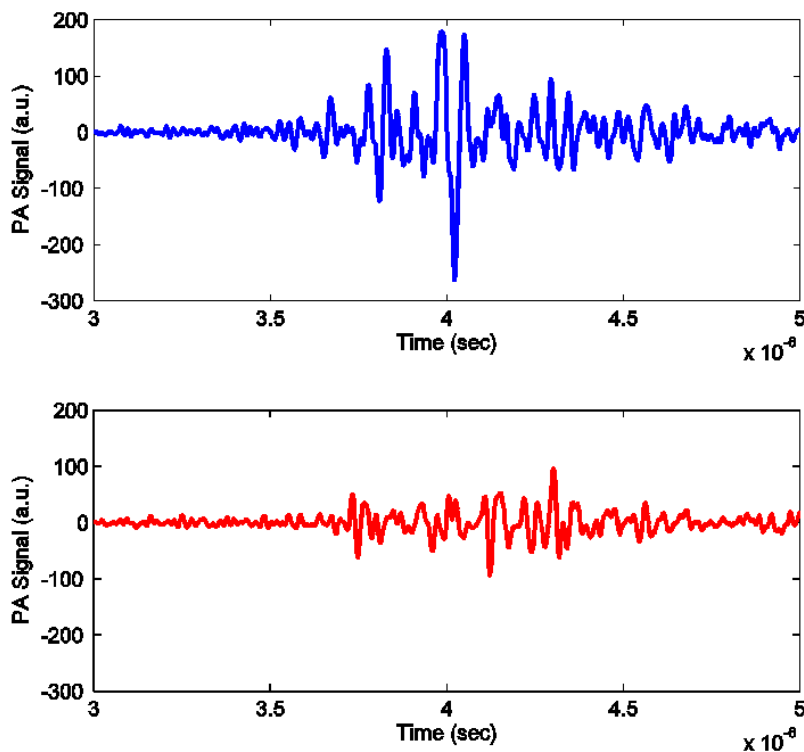


Figure 3.8: Top: Representative waveform of photoacoustic signal from the initial vaporization frame (8<sup>th</sup>). Bottom: Representative waveform of photoacoustic signal from nanoparticle mediated thermal expansion at the 100<sup>th</sup> frame.

While photoacoustic images displayed the characteristic signal of PAnDs, ultrasound images did as well. The ultrasound image taken before laser irradiation is shown in Fig. 3.9. Following laser irradiation, the area of the spleen and above the spleen show a large increase in ultrasound contrast (approximately 50%) as well. When plotting the ultrasound signal over time, it is interesting to note the fluctuations in contrast. This is due to the environment that tissues provided where gaseous bubbles can move and coalesce within and outside of the imaging plane, thus the ultrasound contrast enhancement is more uniform throughout the area as compared to the photoacoustic signal. This experiment indicates that PAnDs can be used in a biological environment, produce contrast enhancement above the endogenous contrast of the tissues, and require less laser energy to do so than traditional gold nanorods.

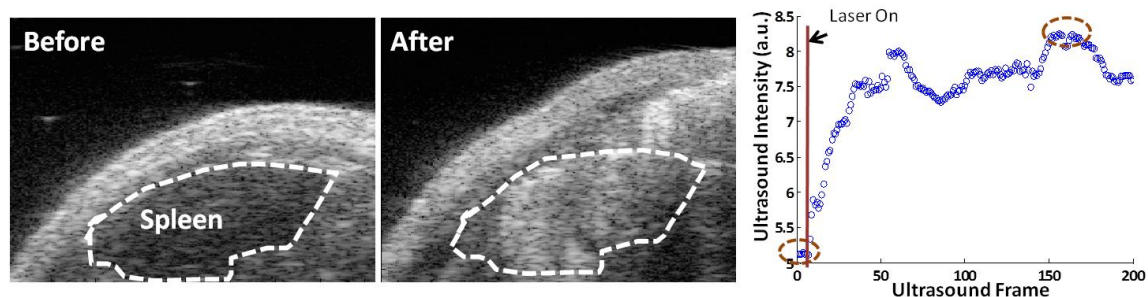


Figure 3.9: Left and middle, Ultrasound images before and after laser activation of injected PAnDs. Right, graph showing increase in ultrasound intensity with continued pulsed laser irradiation. Images are from circled frames.

### 3.6 CONCLUSIONS

This chapter focused on the preliminary phantom experiments that allow characterization of the contrast enhancing abilities of PAnDs for combined ultrasound and photoacoustic imaging. First, the characteristic photoacoustic signal produced by PAnDs was determined as an initially strong peak associated with vaporization, followed with a decreased signal level due to thermal expansion. Furthermore, it was shown that

PAnDs are only activated via optical methods, not with clinically relevant ultrasound. PAnDs were shown to be a more efficient contrast agent in terms of conversion of light to acoustic signal compared to gold nanorods. Finally, it was demonstrated that PAnDs provide significant ultrasound and photoacoustic contrast to overcome the endogenous contrast in tissues, and are still triggerable with relatively low laser fluences. These studies support that PAnDs are feasible for use in *in vivo* applications.

### 3.7 REFERENCES

1. Shah, J. *et al.* Photoacoustic imaging and temperature measurement for photothermal cancer therapy. *J Biomed Opt* **13**, 34024 (2008).
2. Kharine, A. *et al.* Poly(vinyl alcohol) gels for use as tissue phantoms in photoacoustic mammography. *Physics in Medicine and Biology* **48**, 357-370 (2003).
3. Zell, K., Sperl, J.I., Vogel, M.W., Niessner, R. & Haisch, C. Acoustical properties of selected tissue phantom materials for ultrasound imaging. *Physics in medicine and biology* **52**, N475-84 (2007).
4. Cook, J.R., Bouchard, R.R. & Emelianov, S.Y. Tissue-mimicking phantoms for photoacoustic and ultrasonic imaging. *Biomedical optics express* **2**, 3193-206 (2011).
5. Hall, T.J., Bilgen, M., Insana, M.F. & Krouskop, T.A. Phantom materials for elastography. *IEEE Transactions on Ultrasonics, Ferroelectrics and Frequency Control* **44**, 1355-1365 (1997).
6. Madsen, E.L., Zagzebski, J.A., Banjavie, R.A. & Jutila, R.E. Tissue mimicking materials for ultrasound phantoms. *Medical physics* **5**, 391-4
7. Ryan, L.K. & Foster, F.S. Tissue equivalent vessel phantoms for intravascular ultrasound. *Ultrasound in medicine & biology* **23**, 261-73 (1997).
8. Moes, C.J., van Gemert, M.J., Star, W.M., Marijnissen, J.P. & Prahl, S.A. Measurements and calculations of the energy fluence rate in a scattering and absorbing phantom at 633 nm. *Applied optics* **28**, 2292-6 (1989).
9. Fay, B., Brendel, K. & Ludwig, G. Studies of inhomogeneous substances by ultrasonic back-scattering. *Ultrasound in medicine & biology* **2**, 195-8 (1976).
10. Prokop, A.F. *et al.* Polyacrylamide gel as an acoustic coupling medium for focused ultrasound therapy. *Ultrasound in Medicine & Biology* **29**, 1351-1358 (2003).

## **Chapter 4: Exploring Mechanisms Behind Photoacoustic nanoDroplets**

Photoacoustic nanoDroplets (PAnDs) have been synthesized and initially tested for their contrast enhancing abilities and characteristic photoacoustic and ultrasound signals. This chapter will explore the physical mechanisms behind PAnDs' signal generation and more precisely define their functionality. First, a recap of different photoacoustic phenomenon is given emphasizing vaporization and thermal expansion. Then a description of how PAnDs are thought to work is given. Following, experiments are presented to help investigate the reactions of PAnDs under different conditions such as fluence, extent of nanoparticle loading, and droplet size. Finally, the mechanism behind how pulsed laser irradiation triggers PAnDs is investigated. Overall, this chapter engages the physics behind PAnDs.

### **4.1 PHOTOACOUSTIC PHENOMENA**

Thermal expansion is the photoacoustic phenomenon predominantly exploited for photoacoustic imaging, as the laser fluences used to produce acoustic transients are well within the ANSI standard limits for pulsed laser exposure<sup>1</sup>. However, thermal expansion is one of the least efficient energy conversions between light and sound, with the conversion efficiency ( $\eta$ ) around  $10^{-4}\%$ <sup>2</sup>, only more efficient than electrostriction<sup>2</sup>. In comparison, the most efficient mechanism is optical breakdown, or dielectric breakdown, the formation of plasma at the focal point of light, has  $\eta$  at approximately  $30\%$ <sup>3</sup>. Vaporization, the conversion of a material from the liquid to the gas phase is much more efficient than thermal expansion at converting light to acoustic transients, with  $\eta$  close to  $1\%$ <sup>3</sup>. If vaporization could be utilized in biomedical imaging applications, this would allow for deeper imaging, an issue optical modalities struggle with, and help to minimize the concentration of contrast agents used. The conversion of liquids to gas bubbles using

pulsed laser irradiation has been studied in depth<sup>4,5</sup>. Unlike the many applications that investigate bubble formation at boundaries for therapeutic affects, the conversion of liquid to gas bubbles in PAnDs closely matches the theoretical conditions for current equations. For a single bubble, with a smooth surface, that is perfectly spherical and unbound<sup>6,7</sup>, the pressure emitted ( $p_1$ )<sup>8</sup> by the growing vapor volume can be defined as

$$p_1(r, t) - p_0 = \frac{\rho_1}{4\pi r} \frac{d^2V(t-\frac{r}{c})}{dt^2} \quad (4.1)$$

where  $p_0$  is the ambient liquid pressure surrounding the source,  $r$  is the radius from the vaporization center,  $t$  is the time,  $\rho_1$  is the liquid density.  $V$  is the velocity of the bubble expansion, and  $c$  is the speed of sound in the liquid. When combining equation (4.1) with the internal pressure characterized by the Rayleigh-Plesset equation, taking into consideration the liquid viscosity and surface tensions, and assuming the only limitation on bubble growth is liquid inertia, the pressure emitted at a specific time and distance as the first term of a Taylor expansion that describes the initially linear portion of bubble expansion that ends shortly before the maximum bubble diameter is reached. This equation also assumes that the bubble is a compact sound source, which when using a very small, 200 nm droplet, is a likely assumption. So while the pressure does not continuously increase with time, the equation shows that the emitted pressure is dependent on the initial volume of the gas, which in the case of PAnDs is limited by the droplet size. Therefore, the pressure signal emitted by PAnDs during vaporization should be correlated to the droplet diameter.

## 4.2 PHOTOACOUSTIC SIGNAL GENERATION THROUGH THERMAL EXPANSION

As described in Chapter 1, photoacoustic pressure transients due to thermal expansion can be described by the following equation:

$$p_0 = \Gamma \mu_a F \quad (4.3)$$

where  $\Gamma$  is the Grüneisen coefficient (a dimensionless scalar dependent on temperature and native surrounding tissue properties),  $\mu_a$  is the optical absorption coefficient of the optical absorber ( $\text{m}^{-1}$ ), and  $F$  is the laser fluence ( $\text{J}/\text{m}^2$ ). Therefore, the acoustic transients produced from thermal expansion have a linear relationship with the optical absorption coefficient, dependent on the concentration of photoabsorbers, and the laser fluence used to trigger the signal. Equation 4.3 suggests that any signal produced by PAnDs that follows a linear trend when altering the extent of nanoparticle loading or fluence could correspond to signal created due to thermal expansion.

### 4.3 PHOTOACOUSTIC NANODROPLET FUNCTIONALITY

PAnDs are a nano-sized, dual-contrast agent consisting of a bovine serum albumin (BSA) shell and liquid perfluorocarbon (PFC) core, namely perfluoropentane, in which specially capped plasmonic noble metal nanoparticles have been encapsulated. The design and synthesis of these particles are described in Chapter 2. PAnDs are stable because while their nanoscale size increases surface tension, the BSA shell dramatically lowers the surface tension and limits coalescence, thus preventing premature vaporization of super-heated PFC from both clinically relevant imaging ultrasound fields and elevated temperatures. Therefore, pulsed laser irradiation is used to activate (vaporize) this contrast agent, i.e., to remotely trigger the phase transition of PFC.

PAnDs provide three forms of contrast overall. Two forms of contrast for photoacoustic imaging through thermal expansion and vaporization, and one form for ultrasound imaging through increased acoustic impedance mismatch. The contrast from PAnDs is triggered in the following manner. PAnDs are suspended in a tissue-like environment, a phantom as shown in Fig. 4.1, step 1. Upon irradiation with a pulsed

laser, the encapsulated plasmonic nanoparticles, such as gold nanorods, absorb electromagnetic energy from the laser, providing localized heating well over the required vaporization temperature of PFC (steps 1 through 2 in Fig. 4.1). In addition, a high frequency pressure wave is generated at the surface of the plasmonic nanoparticles via thermal expansion. Together, heat and pressure provide the conditions required to nucleate a liquid-to-gas phase transition of PFC, and the PAnD undergoes a vaporization which overcomes the surface tension of the BSA coating (step 3 in Fig. 4.1). The photoacoustic transient produced via vaporization is substantially larger than subsequent transients produced from the expelled plasmonic nanoparticles which undergo thermal expansion under continued pulsed laser irradiation (steps 4-5 in Fig. 4.1). Furthermore, the resulting gaseous phase also produces increased acoustic impedance mismatch between gas bubbles and the surrounding medium (step 6 in Fig. 4.1), providing optically triggered ultrasonic contrast enhancement. Overall, PAnDs provide several types of contrast for two imaging modalities: vaporization and thermal expansion for photoacoustic imaging and gas-tissue acoustic impedance mismatch for ultrasound imaging.

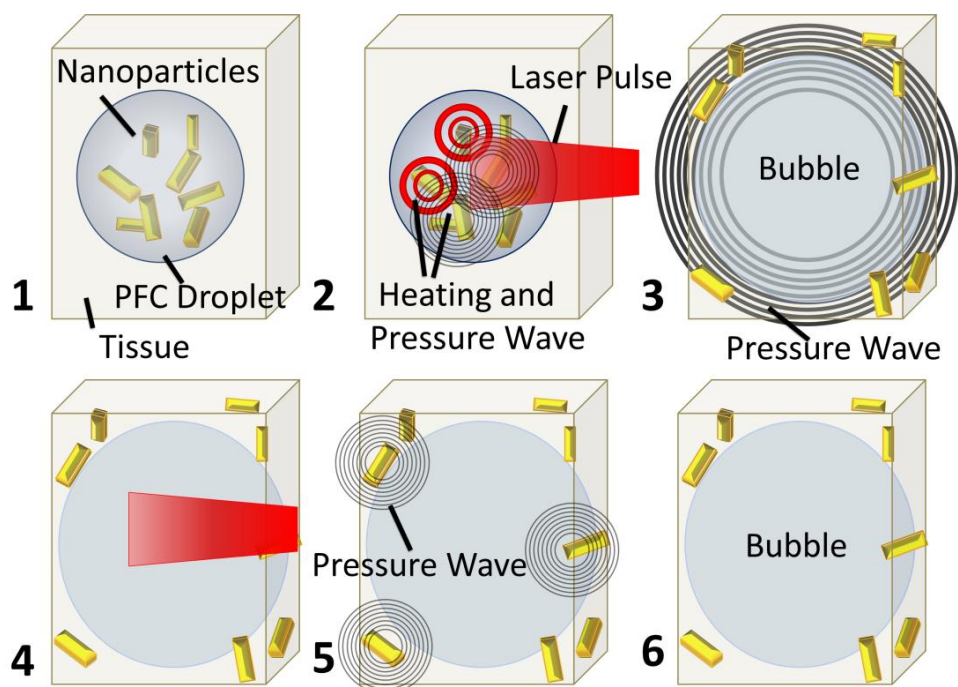


Figure 4.1: Step-by-step diagram of remote activation of PAnDs, providing photoacoustic signal via two mechanisms: vaporization of PAnDs (steps 2-3) and thermal expansion caused by plasmonic nanoparticles (steps 4-5). The resulting gas microbubble of PFC (step 6) provides ultrasound contrast due to increased acoustic impedance mismatch.

There are several ways to experimentally support the described contrast mechanisms of PAnDs. First, in the experimental dependencies of the characteristic signal as shown in Fig. 4.2, both the peak portion due to vaporization and the tail portion due to thermal expansion, are based on laser fluence, nanoparticle loading, and bubble size. It is known that thermal expansion, the mechanism thought to provide the prolonged tail signal, is linearly dependent on several factors including fluence and photoabsorber concentration (Eqn 4.3). It is also known that the pressure wave created via vaporization is directly dependent on the size of the initial droplet (Eqn 4.2). Therefore, by examining the trends of these parts of the signal associated with different photoacoustic phenomenon and altered based on fluence, nanoparticle concentration, and size, the mechanisms responsible can be elucidated.

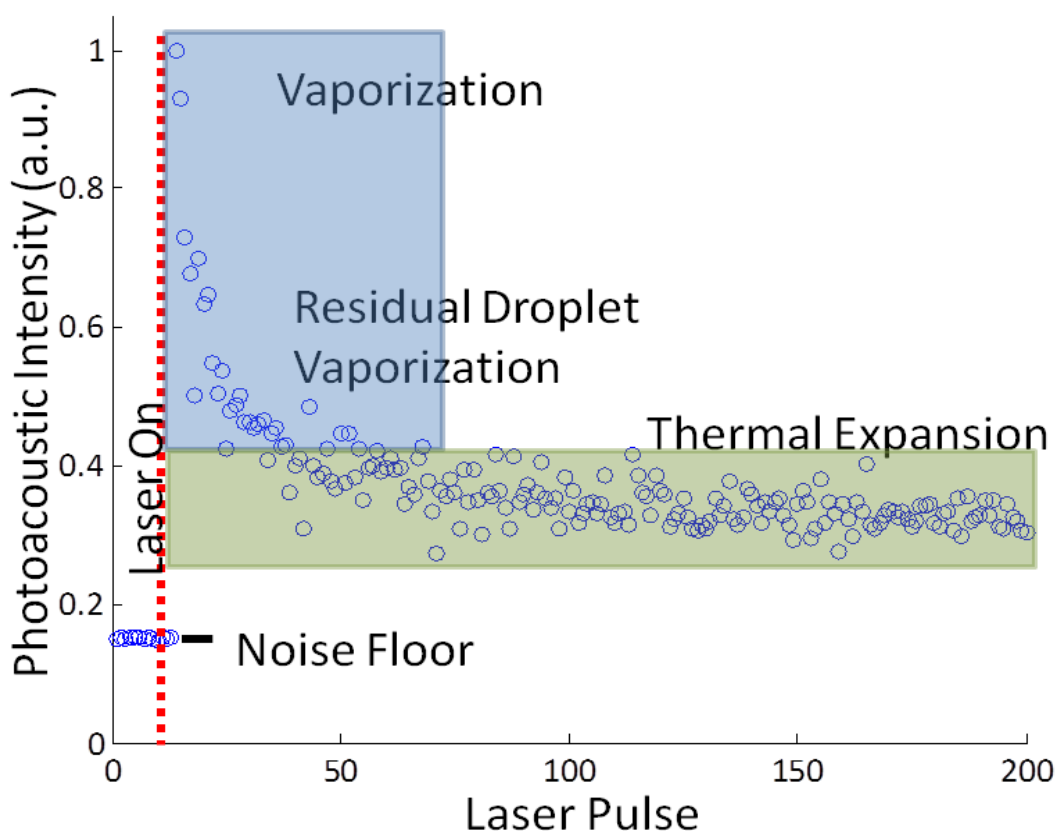


Figure 4.2: Characteristic signal produced by PANs including initial peak signal due to vaporization of the liquid perfluorocarbon droplet and prolonged tail signal due to thermal expansion from the expelled gold nanoparticles.

The other mechanism of PANs which is not clear is how pulsed laser irradiation vaporizes these agents. Two mechanisms are proposed, either heating via optical absorption of the encapsulated plasmonic noble metal nanoparticles or the production of a high frequency, broadband signal from thermal expansion surrounding the encapsulated nanoparticles. Previous research has shown that to activate nanosize perfluorocarbon droplets ultrasonically, either high frequency or high pressure waves need to be used<sup>9</sup>. The pressure transients due to thermal expansion are known to be extremely high frequency<sup>10</sup>, and while these transients would attenuate rapidly, their origins are from within a nano-sized droplet, and therefore could cause vaporization. Furthermore, investigation of vaporization of water with pulsed laser have shown that the main

mechanism for vaporization is thermal expansion<sup>45</sup>. However, perfluorocarbons are also known to be excellent insulators as the heat capacitance is twice that of Styrofoam<sup>11</sup>. This insulating ability of perfluorocarbon suggests that the mechanism could be heating due to rapid heat collection within a short radius from the photoabsorber nucleating gas bubbles on the nanoparticle surface. Furthermore, when modeling the temperature change around a 16 nm gold nanosphere for one  $5 \text{ mJ/cm}^2$ , 10 ns laser pulse, the temperature raises several hundred degrees. Comparatively, the heating immediately surrounding the nanoparticle is less than  $60 \text{ }^\circ\text{C}$  as shown in Fig. 4.3. The heating, while greater in PFC, has a much more shallow depth penetration into the material as compared to the heat profile in water. However, experimentally, the major mechanism of vaporization (either heating or pressure) can be explored by comparing photoacoustic transients caused by PAnDs using both a pulsed and continuous wave laser. The pulsed laser will initiate both a heating and pressure wave effect, while the continuous wave laser will only contribute to heating.

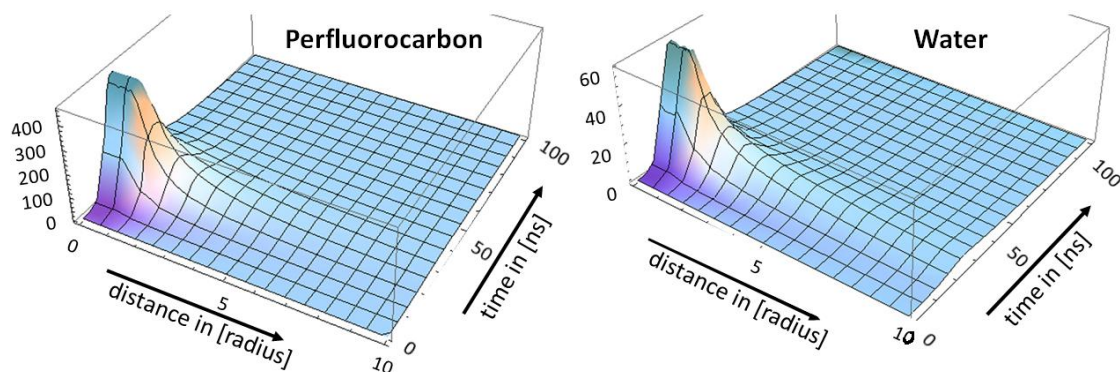


Figure 4.3: Heating profiles in change in temperature ( $^\circ\text{C}$ ) over distance (in radii of the sphere) and time for a 16 nm gold sphere in perfluorocarbon and water. Courtesy of Dr. Wolfgang Frey.

#### 4.4 MATERIALS AND METHODS

Described here are a set of experiments used to explore the mechanisms behind the characteristic photoacoustic signals produced by PAnDs, both vaporization and

thermal expansion, and to investigate how pulsed optical laser irradiation vaporizes PAnDs through heat, pressure transients, or a combination of both.

#### **4.4.1 PAnD Characteristic Signal Corresponding to Photoacoustic Phenomena**

To explore the mechanisms which contribute to PAnD's unique signal, several polyacrylamide phantoms were synthesized as previously described in Chapter 3 with a cylindrical inclusion containing PAnDs. The Vevo2100 combined with the SpectraPhysics laser with integrated fiber light delivery were used to perform combined photoacoustic and ultrasound imaging on all the phantoms. To test for the influence of fluence on the photoacoustic signal, one phantom was subjected to irradiation at different fluences (approximately 6, 8, 10, and 16 mJ/cm<sup>2</sup>). Different points in the same phantom were irradiated to ensure that variables such as PAnD population, size, and loading were controlled. To test the influence of nanorod loading on the photoacoustic signal, another set of phantoms were synthesized using 400 nm PAnDs with different amounts of gold nanorod loading (0.5, 1, and 2 ml of phase transferred gold nanorod solutions in the PAnD synthesis described in Chapter 2). This set of phantoms was irradiated at 5 mJ/cm<sup>2</sup> fluence. Finally, to test the influence of PAnD's size, four phantoms were synthesized containing PAnDs sized to 100, 200, 400, and 1000 nm diameters using a lipid mini extruder on PAnD solutions that were 100 times diluted after synthesis in PBS. Each condition had three repetitions of imaging done, and data was extracted in the region of interest around the inclusion. ANOVA testing was done to test if the differences between collected photoacoustic signal amplitude values with different conditions were statistically significant, and linear regression was done to show linear trends for nanoparticle loading and fluence was done.

#### **4.4.2 Optical Triggering Mechanism**

PAnDs were loaded into a 10% poly(acrylamide) cylindrical inclusion in a tissue mimicking-phantom at an 100 fold dilution of as synthesized concentration as described in Chapter 3. The same phantom, at different cross-sections, was irradiated with either a 10 Hz, pulsed (5-7 ns pulse duration) Nd:YAG laser with a fluence of  $5 \text{ mJ/cm}^2$  tuned to 808 nm (SpectraPhysics) or a continuous wave diode laser (2 W) emitting at 808 nm. It is difficult to compare power between pulsed and continuous wave lasers due to the extremely short time periods (ns) that pulsed lasers are active. Therefore, a relatively low fluence was used with the pulsed laser, and a relatively high power was used for the continuous wave laser experiments to try and compensate for that difficulty. However, the continuous wave laser, when compared to the average power delivered by the pulsed laser was two orders of magnitude higher. Ultrasound signals were collected using the Vevo2100 with a 20 MHz transducer for 500 laser pulses (50 seconds) and monitored for changes over time. Graphs were produced by analyzing ultrasound intensity over a specific region of interest around the inclusion.

#### **4.5 RESULTS AND DISCUSSION**

Several phantom experiments are described here that help elucidate the mechanisms behind PAnDs. Specifically, these experiments are used to identify the photoacoustic phenomenon associated with the characteristic signals that PAnDs demonstrate. Furthermore, the mechanism (either heating or pressure generation) behind the optical vaporization of PAnD is explored by contrasting their response to pulsed and continuous wave laser irradiation.

#### 4.5.1 PAnD Characteristic Signal Corresponding to Photoacoustic Phenomena

Fluence, nanoparticle loading, and droplet size were all varied in phantom studies to determine if the different aspects of the signal provided by PAnDs were correlated to vaporization or thermal expansion signal. When altering fluence and extent of nanoparticle loading, the peak signal showed no statistically significant differences between the different fluence or nanoparticle loading conditions, and showed no linear trends as illustrated in Fig. 4.3. However, the tail portion of the signal (Fig. 4.2), thought to be due to thermal expansion, showed very strong linear correlations ( $R^2 = 0.939$  for fluence and 0.998 for nanoparticle concentration). Furthermore, upon ANOVA analysis, the means for all the signals collected for different nanoparticle loading and fluences showed statistically significant differences in their means. ANOVA and linear regression combined indicating that the hypothesis of a linear correlation based on fluence or nanoparticle loading cannot be rejected. All graphs are shown in Fig. 4.4. These results support the theory that the characteristic signal is due to dual photoacoustic phenomena (i.e., vaporization and thermal expansion). First, the initial vaporization of the perfluorocarbon droplets should produce (in future experiments) a signal correlated to the initial diameter of the droplet (Eqn 4.2) but independent of fluence and extent of nanoparticle loading. Second, the prolonged thermal expansion signal is linearly correlated with the nanoparticle concentration and fluences used (Eqn 4.3) and caused by the expelled gold nanorods, but has no correlation to initial PAnD diameter.

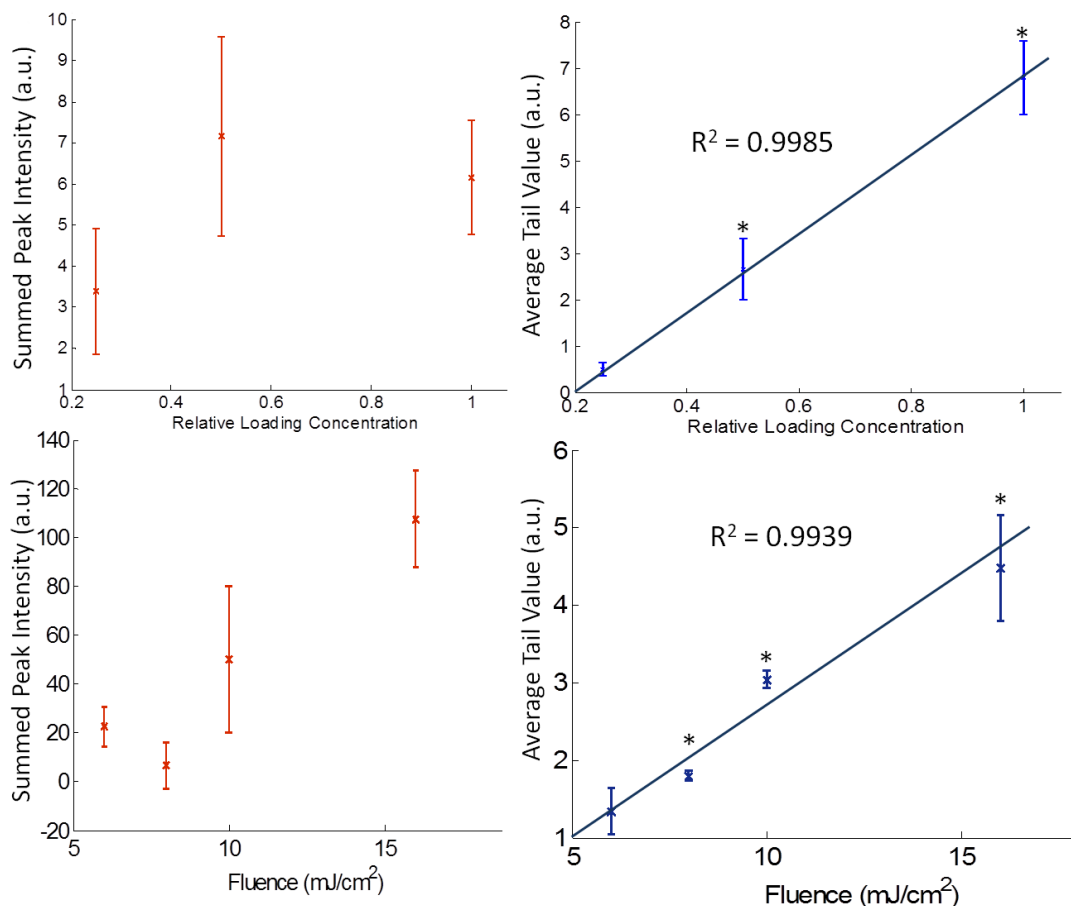


Figure 4.4: Graphs comparing signal trends of the peak signal (vaporization, left) and tail signal (thermal expansion, right) for the thermal expansion linear dependencies on nanoparticle concentration (top), and fluence (middle). Asterisks indicate values that are statistically significantly different from other conditions.

#### 4.5.2 Optical Triggering Mechanism

When comparing the ultrasound signals from cross sections irradiated with the continuous wave laser to those irradiated by the pulsed laser, it is evident that the PANs only vaporized in the presence of pulsed laser. The first and last frames of both laser irradiation types are shown in Fig. 4.5 and are displayed in a 70 dB scale. Furthermore,

the increase in ultrasound signal over time for both laser conditions is shown in the graphs in Fig. 4.5. Pulsed laser irradiation produced a rapid increase in ultrasound contrast that leveled off over time (over a 70% increase), while continuous wave laser irradiation produced very minimal (less than 4%) increase in ultrasound signal. The goal of this study was to determine whether heating or high frequency pressure wave caused by optical absorption by the encapsulated gold nanorods was the main factor in the optical vaporization of PAnDs. As heating occurs in both pulsed and continuous wave laser irradiation, especially at a high power, and pressure waves only occur during pulsed laser irradiation (due to thermal confinement requirements), it is clear that PAnDs vaporize mainly due to the high frequency pressure waves produced by the encapsulated gold nanorods. Furthermore, to ensure that the PAnDs were behaving normally under pulsed laser irradiation, the photoacoustic signals over time were collected for the two laser conditions and are shown in Fig. 4.6. PAnDs irradiated with the traditionally used pulsed laser show the characteristic photoacoustic signal associated with vaporization followed by thermal expansion, while the continuous wave irradiated phantom show no photoacoustic signal, only that associated with the noise in the system. While no thermal expansion signal is expected, vaporization would still be detectable, just not locatable as there is no input trigger to start the calculation of time-of-flight. While it is important to understand exactly how PAnDs act as dual contrast agents to allow for optimization of their usage, these findings support application specific uses of PAnDs as well. These results allude to the possibility that PAnDs could be used as a temperature monitoring device for photothermal therapy. It has been previously shown (Chapter 2) that PAnDs spontaneously vaporize at approximately 50 °C. Therefore, if used in conjunction with continuous wave laser photothermal therapy, PAnDs would vaporize when the tissues

reached an adequate temperature, and could be monitored for vaporization using ultrasound imaging.

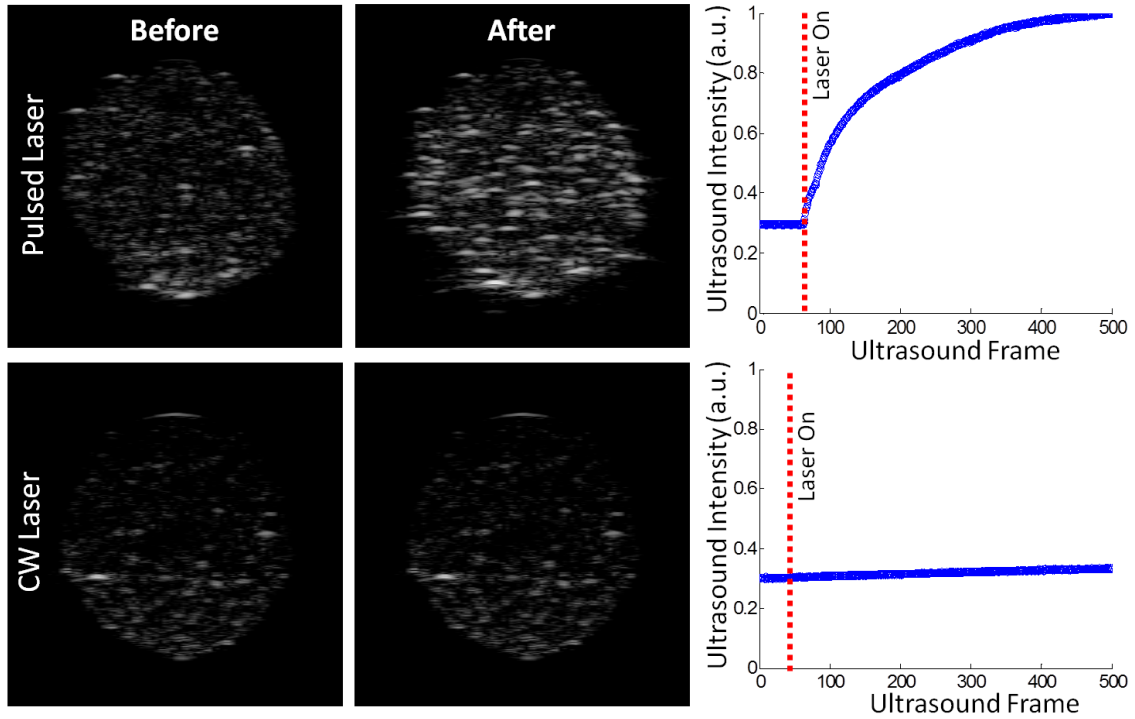


Figure 4.5: Top: ultrasound images from the first and last laser pulses (corresponding with the first and last ultrasound images), and a graph displaying the ultrasound signal increase over time. Bottom: ultrasound images from before the continuous laser was turned on and the last frame taken and a graph displaying the ultrasound signal increase over time.

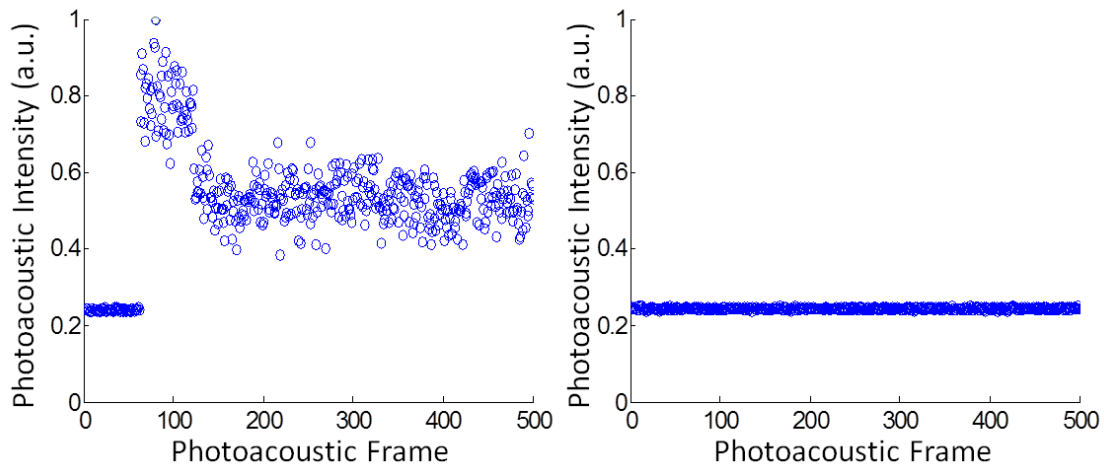


Figure 4.6: Graphs of photoacoustic signal over time for irradiation with a pulsed laser (left) and a continuous wave laser (right).

#### 4.6 CONCLUSIONS

Experiments designed to study the physics behind PAnDs and their triple contrast enhancement mechanisms were presented in this chapter. By exploring the correlations of signals, either the peak signal or prolonged tail signal produced by PAnDs, with the governing equations that represent thermal expansion and vaporization, it was shown that the prolonged tail signal is most likely caused by thermal expansion around the gold nanorods and the initial peak signal is due to vaporization of the liquid PFC droplet. Furthermore, it was determined by using a continuous wave laser, which prevents generation of pressure transients by not permitting the condition of thermal confinement to be met, that the main mechanism for the vaporization of PAnDs is the thermal expansion based, high frequency pressure transients produced by gold nanorods undergoing thermal expansion. Overall, these experiments provide insight into the physics behind the three contrast mechanisms generated by PAnDs and will allow for optimization for potential applications.

#### 4.7 REFERENCES

1. ANSI Orlando: Laser Institute of America . *American National Standard for Safe use of Lasers, ANSI Z136.1* (2000).
2. Sigrist, M.W. Laser generation of acoustic waves in liquids and gases. *Journal of Applied Physics* **60**, R83-R122 (1986).
3. Lyamshev, L.M. Optoacoustic sources of sound. *SOV PHYS USPEKHI* **24**, 977–995 (1981).
4. Asshauer, T., Rink, K. & Delacrétaz, G. Acoustic transient generation by holmium-laser-induced cavitation bubbles. *Journal of Applied Physics* **76**, 5007 (1994).
5. Kim, D. & Grigoropoulos, C.P. Phase-change phenomena and acoustic transient generation in the pulsed laser induced ablation of absorbing liquids. *Applied Surface Science* **127–129**, 53-58 (1998).
6. Landau, L.D. & Lifshitz, E.M. *A Course in Theoretical Physics - Fluid Mechanics*. **6**, 551 (Pergamon Press Ltd.: 1987).
7. Plesset, M.S. & Prosperetti, A. Bubble Dynamics and Cavitation. *Annual Review of Fluid Mechanics* **9**, 145-185 (1977).
8. Zhao, Z., Glod, S. & Poulikakos, D. Pressure and power generation during explosive vaporization on a thin-film microheater. *International Journal of Heat and Mass Transfer* **43**, 281-296 (2000).
9. Sheeran, P.S., Luois, S., Dayton, P.A. & Matsunaga, T.O. Formulation and Acoustic Studies of a New Phase-Shift Agent for Diagnostic and Therapeutic Ultrasound. *Langmuir* **27**, 10412-10420 (2011).
10. Aussel, J.D., Le Brun, A. & Baboux, J.C. Generating acoustic waves by laser: theoretical and experimental study of the emission source. *Ultrasonics* **26**, 245-255 (1988).
11. Stephens, R.B., Cieloszyk, G.S. & Salinger, G.L. Thermal conductivity and specific heat of non-crystalline solids: Polystyrene and polymethyl methacrylate. *Physics Letters A* **38**, 215-217 (1972).

## Chapter 5: *In Vivo* Testing of Photoacoustic nanoDroplets

Photoacoustic nanoDroplets (PAnDs) have been shown to display characteristic contrast enhancement, a signature signal production created via initial vaporization of the perfluorocarbon followed by continued thermal expansion facilitated by the optical absorption of the encapsulated gold nanorods, for combined ultrasound and photoacoustic imaging in tissue mimicking phantom studies (Chapters 3 and 4). However, to move towards clinical translation, PAnD efficiency needs to be proven in animal models and, later, in human subject studies. Tissues have high optical absorption and scattering properties that typically prevent optical imaging modalities from detecting pathologies at high spatial resolution and sensitivity deeply within tissues. Here, two *in vivo* animal imaging studies are presented using a Nu/Nu mouse model. One study was accomplished by using a direct injection of PAnDs into the imaged tissue, while the other study was attempted through the use of a subcutaneous xenograft tumor model and injection of PAnDs into the circulatory system via a tail vein injection. The background on the *in vivo* use of particles similar to PAnDs either in composition or size is discussed here, followed by the methods and results for the two *in vivo* imaging studies performed.

### 5.1 INTRODUCTION

Nano-sized, phase-changed emulsions of liquid perfluorocarbons capped with varying agents are of focus in research currently due to their interesting properties of being able to not only enhance contrast for ultrasound imaging, but also their potential to extravasate out of the circulatory system and into tumor interstitial space due the leaky vasculature of tumor tissues<sup>1-3</sup>. These highly interactive particles have promising futures in molecular imaging. These nano-sized particles were created after much research on their micrometer sized cousins for vascular circulation purposes. Albunex<sup>4,5</sup>, Optison<sup>5,6</sup>,

and Quantison<sup>7</sup> are albumin shelled particles that are clinically available for use for contrast enhancement in cardiology and blood flow imaging. These particles are known to circulate for several hours<sup>4,7</sup>, but are mainly collected in the liver due to their larger size<sup>4,8,9</sup>.

In the last five years, much research has been done on nanometer sized, phase change agents with shells comprised of lipids, proteins, and polymers<sup>10-15</sup>. However, to be relevant as possible to this work, only nanometer sized, albumin particles will be mentioned. Several groups have started to investigate ultrasound activated agents for ultrasound contrast only altering the frequencies or pressure used or the perfluorocarbon encapsulated with the particles<sup>13,16,17</sup>. While *in vivo* animal studies are limited as the research on these particles is new and usually focused on MRI contrast enhancement or used as blood substitutes, all show great promise for the ability of albumin coated particles to circulate in the vasculature for prolonged periods of time (>4 hours) to allow for accumulation in a tumor site<sup>18-20</sup>. Therefore PAnDs should be able to maintain stability in a blood environment as they are made of albumin, the most populous blood protein. Albumin can withstand temperatures of up to 50 °C as shown in Chapter 2. Furthermore, previous studies show albumin coated particles surviving in *in vivo* situations.

## 5.2 METHODS

Two methods are described here to study the efficiency of PAnDs as a dual contrast agent for combined ultrasound and photoacoustic imaging. First, to control for effects that circulating and accumulating could have on PAnDs, a study was done that involved direct injection and imaging of PAnDs into the pancreas of a mouse. Then, in an attempt to view accumulation of PAnDs in tumor tissues, a mouse with a subcutaneous

tumor xenograft was used in combination with a tail vein injection to introduce PAnDs into the vasculature system.

### **5.2.1 Direct Intrapancreatic Injection Study**

An animal study was done using a direct injection of PAnDs into the pancreas followed by imaging. The contrast agent preparation, imaging procedure, injection, and follow up work are described. Furthermore, a comparison study is done by following the sample procedure but using the same amount of gold nanorods only to determine the extent of which gold nanorods increase contrast over endogenous contrast.

#### ***5.2.1.1 Contrast Agent Preparation***

PAnDs were synthesized as previously described at a concentration of  $10^8$  PAnDs/ml with approximately ten gold nanorods per droplet as determined by spectrophotometry and cTEM, and then sized to 400 nm using a lipid mini-extruder. PEGylated gold nanorods were synthesized as described previously, but only underwent the ligand exchange method until the first exchange which resulted in a capping of PEG-thiol, allowing these particles to be injected directly into an animal. Both types of particles were sterilized using UV light for 20 min as described previously.

#### ***5.2.1.2 Imaging Procedure***

The spleen and pancreas were located using a Vevo2100 ultrasound imaging system (VisualSonics) equipped with a 40 MHz, 256-element array transducer. To generate photoacoustic transients, the tissue was irradiated with a laser beam (780 nm wavelength (the peak optical absorption of the gold nanorods encapsulated within PAnDs), 5–7-ns pulses, 10-Hz pulse repetition frequency and  $14 \text{ mJ/cm}^2$  fluence) generated by a Nd:YAG Q-switched pulsed laser pumping an optical parametric oscillator (Newport—Spectra Physics). Control ultrasound and photoacoustic images

were taken before nanoparticle injection. After the injection, photoacoustic signals were recorded before and during pulsed laser irradiation (475 laser pulses). This setup and the animal monitoring and injection guidance system are all shown in Fig. 5.1.

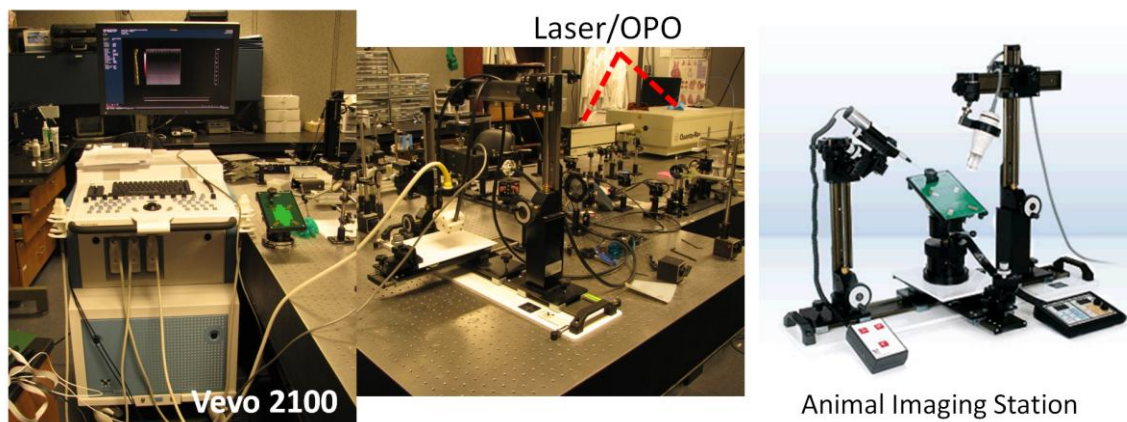


Figure 5.1: (Left) The Visual Sonics Vevo2100 small animal imaging ultrasound system with transducer coupled with optical fibers to the SpectraPhysics Nd:YAG OPO laser system. (Right) Animal health was maintained with warming pad and injection guidance system. Picture courtesy of VisualSonics.

### ***5.2.1.3 Ultrasound Guided Intrapancreatic Injection***

A female, 3-month-old, Nu/Nu mouse (Charles River Laboratory) was anesthetized using 1.5% isoflurane and 2.5% oxygen following proper animal care and use protocols. (Animal handling and care complied with the Guide for the Care and Use of Laboratory Animals (1996). Animal study protocol was approved by The University of Texas at Austin Institutional Animal Care and Use Committee (IACUC)). Using a needle, 100  $\mu\text{l}$  of an equal volume mixture of PANs and Matrigel (BD Biosciences), used to prevent high levels of migration of the PANs away from the injection site, were injected into the pancreas, which resides under the spleen at  $\sim 5\text{--}7$  mm of depth from the skin surface, of the mouse under ultrasound image guidance. Matrigel has peak

absorption at 461 nm, and, as confirmed in previous experiments, does not produce appreciable photoacoustic signal in response to 780 nm laser irradiation.

#### ***5.2.1.4 Gold Nanorod Control Animal***

An *in vivo* experiment was undertaken to determine how effective PAnDs are in producing photoacoustic contrast as compared with the traditional contrast agent, plasmonic gold nanorods alone in biological tissues. To define the exact amount of nanorods encapsulated in the injected amount of PAnDs in the Intrapancreatic injection experiment, several samples were analyzed using spectrophotometry. The spectrum of highly scattering and absorbing PAnDs loaded with gold nanorods was compared with the optically scattering spectra of empty PAnDs to estimate the absorption of nanorods encapsulated in PAnDs. A solution of nanorods with polyethylene glycol grafted to their surface was diluted in water until the optical density matched that of the encapsulated nanorods. Using an anesthetized Nu/Nu mouse and the same imaging setup used in the *in vivo* experiment, baseline photoacoustic and ultrasound images were taken to evaluate the endogenous contrast inherent in a mouse spleen and pancreas. The noise floor of photoacoustic imaging system was evaluated using these images. Then, 50  $\mu\text{l}$  of the diluted nanorod solution, for a total of  $\sim 5 \times 10^8$  nanorods, was injected using the same protocol as the *in vivo* experiment. The animal was imaged and changes in photoacoustic intensity during continued laser irradiation were analyzed.

#### ***5.2.1.5 Animal Sacrifice and Dissection***

After the imaging of the animals was complete, the animals were sacrificed at 48 hours after injection to allow for dissection and possible histology and analysis of biodistribution of gold particles. Animals were sacrificed via slow exposure to  $\text{CO}_2$  gas, followed by cervical dislocation.

### ***5.2.1.6 Data Processing and Image Reconstruction***

The ultrasound and photoacoustic images were reconstructed off-line, and displayed using a linear (photoacoustic) or logarithmic (ultrasound) scale. All images are presented in the same dynamic range so intensity is directly relatable between images. In order to make graphs of signal over time, a region of interest was used over the injection site and the total photoacoustic and ultrasound intensities were calculated for each frame and plotted. Note, there is no animal motion or respiration correction in these images and graphs. These same methods were also used for the tail vein injections studies discussed below.

### **5.2.2 Tail Vein Injection Study**

To allow for a study of PAnDs ability to accumulate within tumor tissues, a study was done that used tumor xenograft models followed by tail vein injection of PAnDs to introduce them into the circulatory system. While the end results presented are negative due to inability to successfully inject PAnDs, the experimental design is sound, and therefore presented here in order to aid others in similar experiments the methods will be described in detail.

#### ***5.2.2.1 Subcutaneous Tumor Model***

Inoculation of tumors in 3 month old, female, Nu/Nu mice was done in the following manner. First,  $10^6$  A431 cancer cells, which are known for production of highly vascularized tumors, were grown and suspended in 100  $\mu$ l of DPBS and stored on ice for transport to the animal housing building. Mice were made drowsy by exposure to a kimwipe dampened with isoflurane. Then the mice were grasped by the skin above their shoulders and tail to allow for intraperitoneal injection of an anesthetic (avertin) solution. Once the mouse was asleep as confirmed by pinch test on the hind paws, the cultured

cells were injected subcutaneously on the right hip of the animal. This location prevents the most motion artifacts as well as provides a superficial and easily accessible location for imaging methods. Tumors were allowed to grow for approximately two weeks until they were sufficient in size, greater than 5 mm but less than 1 cm. Mice were monitored for signs of sickness including malaise, weight loss, and refusal to eat. If an animal appeared sick or the tumor started to erode through the skin, the animal was immediately sacrificed to prevent unnecessary suffering.

#### ***5.2.2.2 Contrast Agent Preparation***

PAnDs were synthesized as described previously, sized to 200 nm to allow for maximum accumulation within the tumor, and concentrated by a factor of ten to  $10^9$  PAnDs/ml and resuspended in DPBS. The solutions were sterilized by 20 min of exposure to UV light, although technically the solution would be sterilized by passing through the 200 nm polycarbonate filters.

#### ***5.2.2.3 Imaging Procedure***

On mice that had developed sufficiently large tumors, a combined ultrasound and photoacoustic experiment was done. The animal was placed under anesthesia (2.5% isoflurane, 1.5% O<sub>2</sub>) and taped to a heated electrocardiogram pad so that vitals such as temperature, respiration rate, and heart rate could be continuously monitored. Using the a Vevo2100 ultrasound imaging system equipped with a 40 MHz, 256-element array transducer several ultrasound and photoacoustic control images were taken before injection. To generate photoacoustic transients, the tissue was irradiated with a laser beam (780 nm wavelength (the peak optical absorption of the gold nanorods encapsulated within PAnDs), 5–7-ns pulses, 10-Hz pulse repetition frequency and 14 mJ/cm<sup>2</sup> fluence) generated by a Nd:YAG Q-switched pulsed laser pumping an optical parametric

oscillator. First, 3D ultrasound and spectroscopic (760, 780, 800, 850, 900 nm) photoacoustic images were taken to account for the total area of the subcutaneous tumor. Then, a single imaging plane which was determined to be high vascular was imaged over time with both ultrasound and photoacoustic images. Then, the animal was allowed to wake up so the tail vein injection could be administered as described in Section 5.2.2.4. After waiting for 4 hours, the animal was placed back under anesthesia and only ultrasound was used to relocate to approximately the same imaging plane as before. Then, single plane photoacoustic and ultrasound images were taken for 60 seconds, followed by 3D ultrasound and spectroscopic images. No laser irradiation was applied to the animal between the injection and collection of photoacoustic images of a single plane over time.

#### ***5.2.2.4 Tail Vein Injection***

To introduce PAnDs into the circulatory system, tail vein injections were attempted. Mice, which had grown tumor xenografts that had reached a sufficient size (greater than 5 mm diameter, but less than 1 cm diameter), were considered ready for imaging studies. Mice were placed into the tail vein injection holder, and a special cone was adapted and inserted into the stage to prevent the mice from turning their heads in the stage to prevent accidental death. The mice tails were submerged in warm water to help dilate the veins. Oil of wintergreen was applied with a cotton swab to help visualize the veins. Then 100  $\mu$ l of PAnDs with a concentration of  $10^9$  droplets/ml were injected into the most prominent vein with the bevel of the needle facing outwards from the animal. A successful injection would include a flushing of the vein of color as the solution was introduced and little to no resistance in injecting the solution.

#### **5.2.2.5 Animal Sacrifice and Dissection**

After the imaging of the animals was complete, the animals were sacrificed at 48 hours after injection to allow for dissection and possible histology and analysis of biodistribution of gold particles. Animals were sacrificed via slow exposure to CO<sub>2</sub> gas, followed by cervical dislocation. During dissection, all organs and the tumor were separated and weighed and frozen for storage. Half of the tumor was fixed for histology in formaldehyde for 24 hours followed by storage in ethanol. Upon successful data analysis, the tissue samples would have undergone digestion and analysis via mass spectroscopy and the histology tumor would have been sent for slicing and staining by an outside company.

### **5.3 RESULTS AND DISCUSSION**

#### **5.3.1 Intrapancreatic Injection**

While PAnDs produced high levels of contrast enhancement in *in vitro* phantom studies, it is important to test their performance in an *in vivo* setting. The spleen represents a highly optically absorbing organ owing to its high blood content. Imaging through the blood-laden spleen and at depth in the pancreas represents a challenge for photoacoustic imaging applications, and therefore it was chosen as an imaging target to exhibit the contrast-enhancing capabilities of PAnDs. Photoacoustic images were collected for 475 laser pulses (that is, 475 photoacoustic frames). Initially, the laser beam was blocked from irradiating the animal to prevent unrecorded vaporization of PAnDs and to determine the noise level of the imaging system. Upon radiation, the photoacoustic signal within the region of interest corresponding to injected PAnDs was initially very strong and, as the pulsed laser irradiation continued, it decayed to the level corresponding to superposition of signals from the expelled nanorods and endogenous thermal

expansion (Fig. 5.2). The vaporization signal was 4.3 dB higher than that given by the nanorod and endogenous chromophores combined. Based on control experiments using the equivalent number of nanorods as encapsulated in the injected PAnDs, the increase of signal generated by the nanorods alone was  $\sim 1.9$  dB, for a total of 6.0 dB increase in signal generation using PAnDs. The corresponding combined photoacoustic and ultrasound images in Fig. 5.2b and 5.2c illustrate the peak photoacoustic signals corresponding to vaporization of PAnDs and thermal expansion. As evident from Fig. 5.2, the photoacoustic signal produced by the initial vaporization is much stronger than the signal produced by thermal expansion.

As displayed in Fig. 5.2d–f, a comparison of photoacoustic signal from thermal expansion caused by endogenous photoabsorbers and the photoacoustic signal from thermal expansion caused by both the endogenous photoabsorbers and the injected gold nanorods revealed that the associated signal increase is 24%, or 1.9 dB. The percentage difference in signal provided by an absolute number of nanorods can be used to determine the overall photoacoustic signal enhancement caused by PAnDs above the endogenous contrast of the animal with the same absolute number of nanorods encapsulated. Furthermore, it is pertinent to note that under the laser fluence used in our experiments, the gold nanorods remained thermodynamically stable<sup>21</sup> and, therefore, do not exhibit photoacoustic signal change with laser irradiation. Furthermore, nanorods alone do not induce vaporization comparable to PAnDs. The photoacoustic and ultrasound signals as the laser irradiated the sample at the first/last photoacoustic frames collected are depicted in Fig. 5.2e–f. As expected, there was no change in these images with continuing laser irradiation.

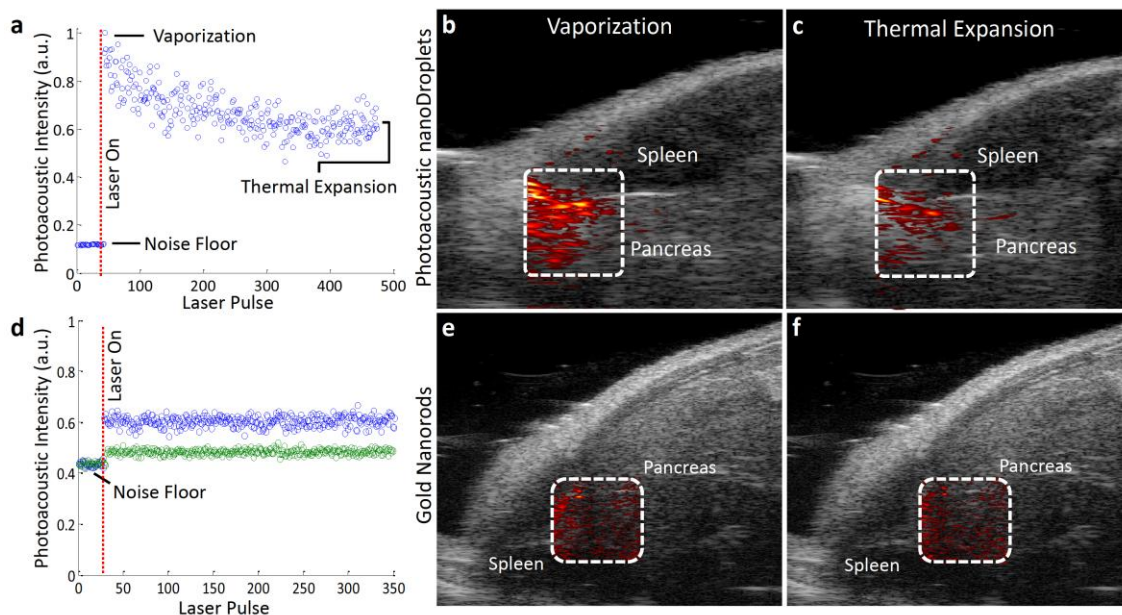


Figure 5.2: Photoacoustic contrast enhancement *in vivo*. (a) Graph depicting the average photoacoustic intensity within the region of interest corresponding to the injected PAnDs, indicated by boxes in panel b and panel c. (b) Image of the peak photoacoustic signal generated from the rapid phase transition of the PAnDs. (c) Image representing photoacoustic signal generated from expelled gold nanorods and endogenous chromophores. Each frame is 20.4 mm wide by 12.8 mm tall. ultrasound is in 20-dB scale. In this experimental setup, ~50% of the droplets are disrupted by the 60th laser pulse. (d) Graph displaying changes of photoacoustic signals during continued pulsed laser irradiation of only gold nanorods. The green circles represent photoacoustic signal of the endogenous photoabsorbers in the mouse tissues. Blue circles represent the photoacoustic signal owing to thermal expansion caused by both the endogenous photoabsorbers and the injected gold nanorods. (e, f) Combined photoacoustic and ultrasound images of mouse cross-section and injection site of gold nanorods immediately after the laser was turned on (first laser pulse) and at the end of the laser pulsing (last laser pulse). Each image is 12.2 mm wide by 10.8 mm tall. ultrasound image is displayed using 20-dB scale.

PAnDs not only produce significant enhancement of photoacoustic contrast in a mouse model but PAnDs also provide significant ultrasound contrast once injected and remotely triggered. Ultrasound images of a mouse cross-section before injection of

PAnDs and after the laser activation injected PAnDs are shown in Fig. 5.3. Owing to the dynamic respiratory/cardiac motion and the nature of internal organs, ultrasound contrast varies owing to migration of PAnDs and bubbles in and out of the imaging plane, coalescence of bubbles, gas diffusion and delayed vaporization of PAnDs. The peak increase of ultrasound contrast was 3.1 dB over post-injection images, and ~29 dB over native ultrasound images. This experiment demonstrates optically triggered, ultrasound contrast enhancement in a living, biological system.

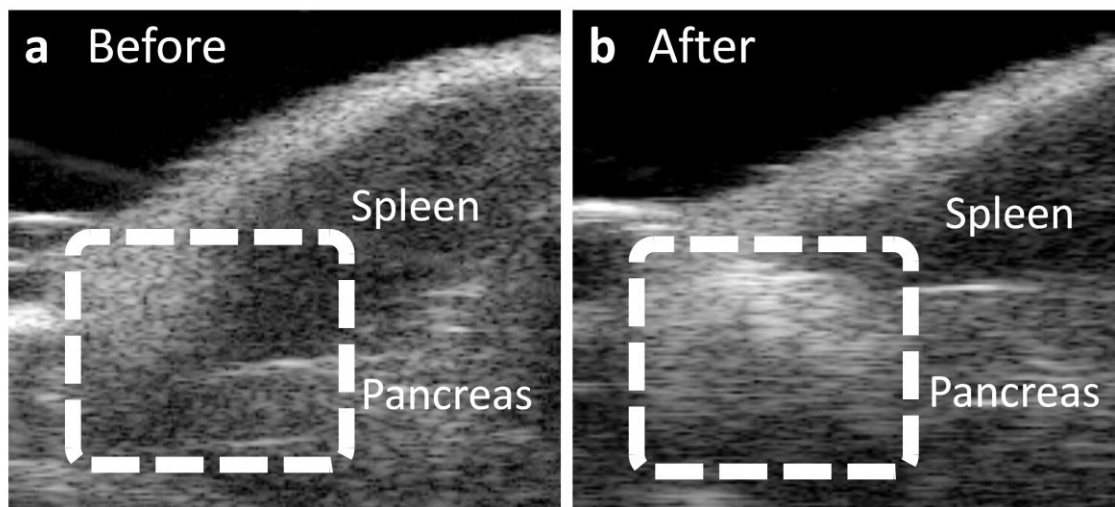


Figure 5.3: Ultrasound contrast enhancement *in vivo*. (a) US image of a mouse before injection of PAnDs displaying the location of the spleen and pancreas. (b) US image after the direct injection and laser activation of PAnDs. Boxes in both images identify the region of interest where PAnDs were injected. Panels are 13.5 mm wide by 18.1 mm tall, and are in 20-dB scale.

### 5.3.2 Tail Vein Injection

After successful direct injections of PAnDs into the pancreas of a healthy mouse, a tumor xenograft model was used to determine how PAnD circulate and accumulate in tumors tissues. However, it quickly became apparent that the actual tail vein injections were not successful. A successful tail vein injection is indicated by flushing of the vein as

the solution passes through and little to no resistance during the injection. While eight attempts were made, a successful injection was never achieved. According to the technicians attempting the tail vein injection, their confidence was low that the injections were successful as they felt strong resistance during the injection, saw no vessel flushing, reported opaque discoloration of the tail area, and saw accumulation of what can only be assumed to be perfluorocarbon gas at the base of the tail. Due to the limited amount of time the animals can be kept after removal from the immunological barrier for imaging, and the limitations on anesthetic usage, each animal was only allowed one full pre-imaging, injection, accumulation time, and post-imaging attempt. A representative collection of photoacoustic and ultrasound is presented in Fig. 5.4. Both ultrasound and photoacoustics show a steady level of signal indicating that no vaporization of PANDs was occurring. However, while this result is disappointing, it is mostly likely not indicative of the inability of the PANDs to circulate and accumulate within the vascular system, as the most probable cause is the injections themselves failed.

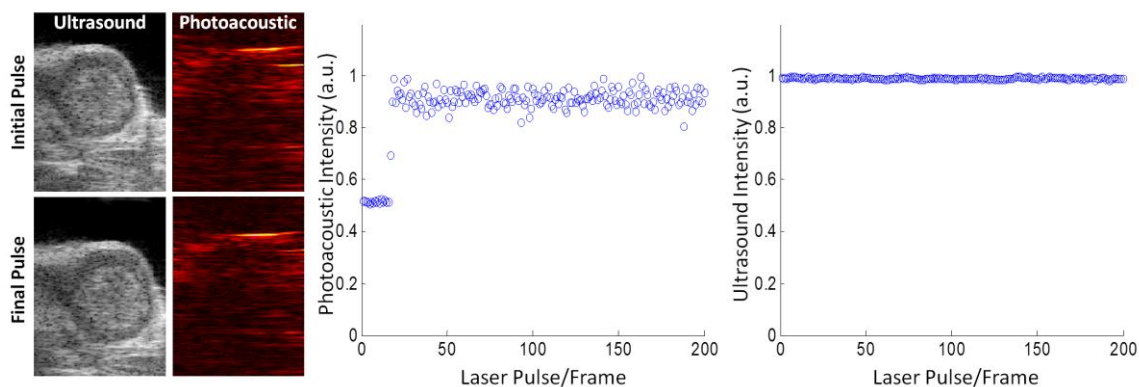


Figure 5.4: Photoacoustic and ultrasound images and corresponding signals over time of a tumor 4 hours after tail vein injection. The results indicate no accumulation of PANDs in the tumor region; however, faulty tail vein injections cloud the interpretation of these results.

In order to test the theory of the tail vein injections not working, several other imaging tests were done. A second imaging session was done at 24 hours to ensure that any accumulation could be potentially imaged. The results of this imaging session shown in Fig. 5.5 lead to the same conclusions as the 4 hour imaging session, that there was no accumulation within the tumor site. Imaging of the animal's spleen and liver, which is where literature suggestions most bubbles are accumulated passively, further showed no accumulation and no characteristic signal generation. Finally, the most indicative evidence that the tail vein injections were not successful was the development of a subcutaneous gas bubble at the base of the tail of the animal as the PAnDs injected into the tail (and remained there) started to vaporize over a 24-48 hour time period. Ultrasound and photoacoustic images were taken at the base of the tail, but as there were no previous images to serve as a control, and there was no vaporization signal, as the PAnD had already vaporized to their gaseous phase, no conclusions could be drawn from this imaging session other than the confirmation of a highly hyperechoic region signaling the collection of a large gas bubble. Possible solutions for these problems include using a highly skilled technician to do the tail vein injections since the solutions of PAnDs (being somewhat viscous) are particularly difficult to inject. Potentially a different injection strategy could also be used, such as intraocular injection.

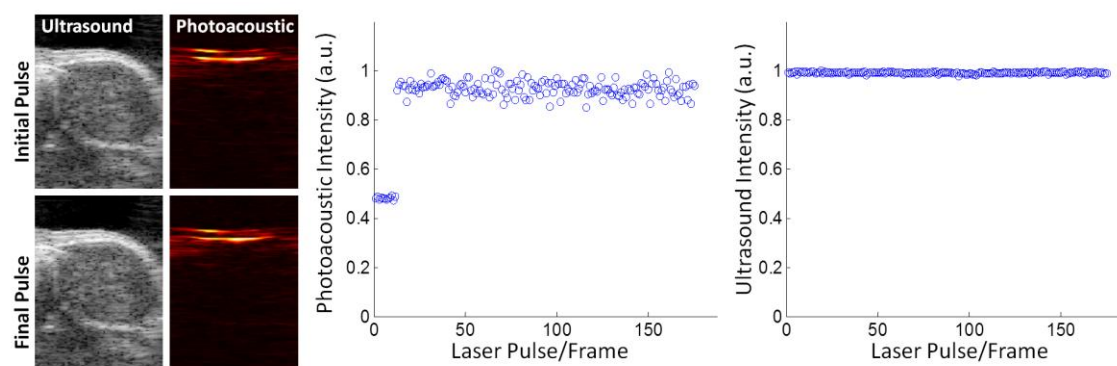


Figure 5.5: Photoacoustic and ultrasound images and corresponding signal over time of a tumor 24 hours after tail vein injection. The results indicate no accumulation of PAnDs in the tumor region; however, faulty tail vein injections cloud the interpretation of these results.

#### 5.4 CONCLUSIONS

Two *in vivo* animal studies were performed to investigate the contrast enhancing abilities of PAnDs in a biological surrounding. The first study, which involved direct injection of PAnDs into the pancreas of a healthy animal, showed characteristic signal enhancement as expected from PAnDs corresponding to the three types of contrast mechanisms PAnDs used. However, the second study, which involved passive accumulation of PAnDs in a tumor, did not show any signal enhancement. While this could potentially be due to several reasons, in this case, it was clearly caused by a failure to properly inject PAnDs into the animal. Additional explorative imaging of the animal's liver and spleen also did not indicate any presence of PAnDs to ensure that there was simply not a problem with extravasation into the tumor tissues. Furthermore, there was collection of perfluorocarbon gas in the tail of the animal, indicating that the PAnDs never flowed out of the tail region. While these results are disappointing, they do not preclude PAnDs ability to be used *in vivo*. Extensive literature shows that albumin coated perfluorocarbon can circulate within the blood stream to accumulate where needed<sup>8,22–26</sup>.

The successful contrast enhancement in the pancreases however, shows that PAnDs have several benefits for biological imaging owing to their unique physical properties. As vaporization provides stronger photoacoustic signal than thermal expansion, by employing PAnDs, a smaller number of noble metal nanoparticles can be used in biological and clinical applications of photoacoustic imaging, reducing the potential toxic effects of plasmonic particles<sup>27</sup>. Furthermore, in biological tissues increased fluence is required to image at sufficient depth. At fluences as low as 8 mJ/cm<sup>2</sup>, gold nanorods can become thermodynamically unstable and this can significantly change their optical properties<sup>21</sup>. PAnDs produce higher photoacoustic signal with only limited laser exposure, as indicated in our phantom and mouse imaging, effectively rendering the thermal stability of nanorods of limited concern. This increased signal can even aid in providing photoacoustic imaging at depths beyond what is obtainable using traditional plasmonic contrast agents and dyes. Finally, regardless of the initial surface fluence of the light delivery, within several centimeters of depth in tissue, the fluence has greatly decreased. As exhibited by phantom experiments, PAnDs require only minimal energy (a fluence of a few mJ/cm<sup>2</sup>) to activate into their contrast-enhancing state, making them able to provide contrast deep within tissues. Recent studies<sup>28</sup> have revealed that photoacoustic imaging at alternative wavelengths, specifically 1064 nm, minimizes endogenous contrast of the tissues, enabling increased imaging depth. Furthermore, the ANSI laser exposure standard also dramatically increases to ~100 mJ/cm<sup>2</sup> in this infrared region<sup>28</sup>. PAnDs can be easily tuned to vaporize at a desired wavelength by changing the aspect ratio of the nanorod, or encapsulating a different plasmonic particle that has peak absorption at the desired wavelength. Therefore, PAnDs are specifically designed to be used in biological contrast-enhancing applications.

## 5.5 REFERENCES

1. Hobbs, S.K. *et al.* Regulation of transport pathways in tumor vessels: Role of tumor type and microenvironment. *Proceedings of the National Academy of Sciences* **95**, 4607-4612 (1998).
2. Maeda, H., Wu, J., Sawa, T., Matsumura, Y. & Hori, K. Tumor vascular permeability and the EPR effect in macromolecular therapeutics: a review. *J Control Release* **65**, 271-284 (2000).
3. Matsumura, Y. & Maeda, H. A new concept for macromolecular therapeutics in cancer chemotherapy: mechanism of tumorotropic accumulation of proteins and the antitumor agent smancs. *Cancer Research* **46**, 6387-6392 (1986).
4. Keller, M.W., Glasheen, W. & Kaul, S. Albunex: a safe and effective commercially produced agent for myocardial contrast echocardiography. *Journal of the American Society of Echocardiography : official publication of the American Society of Echocardiography* **2**, 48-52
5. Li, T., Tachibana, K. & Kuroki, M. Gene transfer with echo-enhanced contrast agents: comparison between Albunex, Optison, and Levovist in mice--initial results. *Radiology* **229**, 423-428 (2003).
6. Chumakova, O.V., Liopo, A.V., Evers, B.M. & Esenaliev, R.O. Effect of 5-fluorouracil, Optison and ultrasound on MCF-7 cell viability. *Ultrasound Med Biol* **32**, 751-758 (2006).
7. Perkins, A.C. *et al.* Human biodistribution of an ultrasound contrast agent (Quantison) by radiolabelling and gamma scintigraphy. *The British journal of radiology* **70**, 603-11 (1997).
8. Ai-Ho, L., Shih-Yen, W., Chien-Hsiu, W., Hsin-Ell, W. & Pai-Chi, L. Targeted multimodality contrast agent: Synthesis and applications of <sup>18</sup>F-labeled targeted perfluorocarbon-filled albumin microbubbles for microUS and microPET. *2009 IEEE International Ultrasonics Symposium* 1274-1277 (2009).doi:10.1109/ULTSYM.2009.5441952
9. Johnson, A.G., Howles-banerji, G., Bing, K.F., Nightingale, K. & Palmeri, M. Method and apparatus for delivery of agents across the blood brain barrier. (2009).at <<http://www.freepatentsonline.com/y2010/0143241.html>>
10. Kwon, S. & Wheatley, M.A. Development and Characterization of PLA Nano-dispersion as a Potential Ultrasound Contrast Agent for Cancer Site Imaging. *Proceedings of the IEEE, 31st Annual Northeast Bioengineering Conference* 144-145 (2005).
11. Pisani, E. *et al.* Polymeric nano/microcapsules of liquid perfluorocarbons for ultrasonic imaging: physical characterization. *Langmuir : the ACS journal of surfaces and colloids* **22**, 4397-402 (2006).

12. Gao, Z., Kennedy, A.M., Christensen, D.A. & Rapoport, N.Y. Drug-loaded nano/microbubbles for combining ultrasonography and targeted chemotherapy. *Ultrasonics* **48**, 260-270 (2008).
13. Rapoport, N., Gao, Z. & Kennedy, A. Multifunctional nanoparticles for combining ultrasonic tumor imaging and targeted chemotherapy. *J. Natl. Cancer Inst.* **99**, 1095-1106 (2007).
14. Rapoport, N. & Gao, Z. Echogenic polymeric nanoparticles for tumor imaging and therapy. *Polym. Prepr. (Am. Chem. Soc., Div. Polym. Chem.)* **47**, 49-50 (2006).
15. Pisani, E. *et al.* Polymeric Nano/Microcapsules of Liquid Perfluorocarbons for Ultrasonic Imaging: Physical Characterization. *Langmuir* **22**, 4397-4402 (2006).
16. Gao, Z., Kennedy, A.M., Christensen, D.A. & Rapoport, N.Y. Drug-loaded nano/microbubbles for combining ultrasonography and targeted chemotherapy. *Ultrasonics* (2007).at  
<[http://www.ncbi.nlm.nih.gov/entrez/query.fcgi?cmd=Retrieve&db=PubMed&dopt=Citation&list\\_uids=18096196](http://www.ncbi.nlm.nih.gov/entrez/query.fcgi?cmd=Retrieve&db=PubMed&dopt=Citation&list_uids=18096196)>
17. Sheeran, P.S., Luo, S., Dayton, P.A. & Matsunaga, T.O. Formulation and Acoustic Studies of a New Phase-Shift Agent for Diagnostic and Therapeutic Ultrasound. *Langmuir* **27**, 10412-10420 (2011).
18. Kawabata, K., Asami, R., Azuma, T. & Umemura, S. Acoustic response of microbubbles derived from phase-change nanodroplet. *Jpn. J. Appl. Phys.* **49**, 07HF18/1-07HF18/9 (2010).
19. Akers, W.J. *et al.* Noninvasive Photoacoustic and Fluorescence Sentinel Lymph Node Identification using Dye-Loaded Perfluorocarbon Nanoparticles. *ACS Nano* **5**, 173-182 (2011).
20. Charlier, N. *et al.* Nano-emulsions of fluorinated trityl radicals as sensors for EPR oximetry. *Journal of magnetic resonance (San Diego, Calif. : 1997)* **197**, 176-80 (2009).
21. Chen, Y.-S. *et al.* Enhanced thermal stability of silica-coated gold nanorods for photoacoustic imaging and image-guided therapy. *Opt. Express* **18**, 8867-8878 (2010).
22. Porter, T.R. *et al.* Targeted vascular delivery of antisense molecules using intravenous microbubbles. *Cardiovasc Revasc Med* **7**, 25-33 (2006).
23. Korpanty, G., Grayburn, P.A., Shohet, R.V. & Brekken, R.A. Targeting vascular endothelium with avidin microbubbles. *Ultrasound Med Biol* **31**, 1279-1283 (2005).
24. Lo, A.H., Kripfgans, O.D., Carson, P.L., Rothman, E.D. & Fowlkes, J.B. Acoustic droplet vaporization threshold: effects of pulse duration and contrast agent. *IEEE Trans Ultrason Ferroelectr Freq Control* **54**, 933-946 (2007).

25. Winter, P.M. *et al.* Endothelial alpha(v)beta3 integrin-targeted fumagillin nanoparticles inhibit angiogenesis in atherosclerosis. *Arteriosclerosis, thrombosis, and vascular biology* **26**, 2103-9 (2006).
26. Lanza, G.M. Targeted Antiproliferative Drug Delivery to Vascular Smooth Muscle Cells With a Magnetic Resonance Imaging Nanoparticle Contrast Agent: Implications for Rational Therapy of Restenosis. *Circulation* **106**, 2842-2847 (2002).
27. Lewinski, N., Colvin, V. & Drezek, R. Cytotoxicity of nanoparticles. *Small* **4**, 26-49 (2008).
28. Homan, K. *et al.* Prospects of molecular photoacoustic imaging at 1064 nm wavelength. *Opt. Lett.* **35**, 2663-2665 (2010).

## Chapter 6: Photoacoustic nanoDroplet Cellular Interactions

The objective of the research described in this chapter is to determine what effects Photoacoustic nanoDroplets (PAnDs) will have on cells both via their passive presence and by their localized vaporization near the cell membrane. In order to accomplish these goals, several studies were undertaken. First, cells were incubated with PAnDs for 30 hours to determine if any of the components of PAnDs caused cytotoxic effects. Next, the potential of non-specific binding of PAnDs, due to their shell being comprised of bovine serum albumin (BSA), was investigated. Finally, the effects of the localized vaporization of the PAnDs near the cell membrane were studied in terms of effect on cell viability and membrane disruption.

### 6.1 INTRODUCTION

So far, the research described in this dissertation has shown PAnDs to be excellent dual contrast agents for combined photoacoustic and ultrasound imaging. Furthermore, these particles are the first to allow photoacoustic imaging via vaporization, a photoacoustic phenomenon that produces large amplitude signal as compared to thermal expansion. However, the vaporization of PAnDs needs to be studied *in vitro* to ensure that vaporization does not induce biological side effects in healthy cells. Beyond active interactions, PAnDs also need to be noncytotoxic. While each component of PAnDs are thought to be biologically inert or minimally cytotoxic<sup>1-3</sup> and some are already FDA approved to be used in other agents<sup>4,5</sup>, the cytotoxicity of these components when combined into PAnD particles needs to be studied.

When PAnDs are injected intravenously, there is a high probability that the particles will accumulate in tumor tissues due to the enhanced permeability and retention effect, which results from the leaky nature of the rapidly developed tumor vasculature,

where endothelial gap junctions are often up to 800 nm,<sup>6-8</sup> as well as active molecular targeting through covalent attachment of monoclonal antibodies to the BSA surface. Furthermore, it has been shown that albumin nanoparticles enhance tumor uptake through a passive binding to the gp60 receptor to albumin<sup>9-11</sup>. Therefore PAnDs are likely to not only accumulate in tumor tissue due to EPR, but also due to receptor mediated binding.

While many passive and active targeting mechanisms can be used to deliver PAnDs to diseased tissue, inevitably PAnDs will accumulate within other parts of the body, such as the liver and spleen. These organs are part of the body's mononuclear phagocyte system that endocytoses foreign bacteria and colloidal particles<sup>12</sup>. While PAnDs are intended to be used for combined imaging and therapy, they must be passive enough to not affect healthy cells. One method to quantify any potential cytotoxicity effects through passive interactions is via cell culture studies using PAnDs incubated with cells and reagents (MTS or MTT) that change properties based on cellular enzymatic activity.

Besides passive cytotoxicity concerns, PAnDs have active physical properties (as discussed and described in Chapter 4) that can also have potentially negative effects on cells and tissues. The larger cousins of PAnDs, phase-change ultrasound contrast agents for ultrasonic contrast enhancement, are currently FDA approved for clinical use<sup>13</sup>. These agents are much larger (micrometers) and therefore their physical effects on surrounding tissues would be more dramatic as compared to PAnDs. The micrometer sized agents do not cause tissue damage or cell death<sup>5</sup>. Sonoporation, or the act of causing temporary, small pores in the membranes of cells by mechanical stimulation of bubbles or micro jetting due to cavitation and inertial collapse, has been studied in-depth<sup>14,15</sup>. These actions cause short term (<1 second) pores to open in the cell membrane that seal themselves causing no long term negative affects in cells. Sonoporation has a promising

future to mediate intracellular delivery of therapeutics such as gene therapies where the cell needs to remain unharmed<sup>14,16-18</sup>. These therapies are generally limited to vascular and cardiac applications, but PAnDs, due to their nano size, could be used to translate these therapies into the tissue interstitial space for tumor therapy and targeted treatment. However, the combination of close proximity vaporization of PAnDs as well as the effect of laser irradiation need to be studied to show if this combination of stimuli causes detectable negative effects on cells.

## 6.2 METHODS

Described here are a set of experiments used to determine the passive and active interactions PAnDs have with cells. The two cell culture lines used in these experiments, A431 (epidermoid carcinoma) and MBA-MD-231 (breast adenocarcinoma), were chosen for their high levels of expression of the EGFR (epidermal growth factor receptor)<sup>19,20</sup>. EGFR was selected as a target for the PAnDs since this receptor is over-expressed in triple-negative or basal breast cancer, which accounts for approximately 7% of all breast cancers but remains one of the most difficult to treat<sup>21-23</sup>. The cells were purchased from Sigma and maintained in a humidified cell incubator at 37 °C and 5% CO<sub>2</sub> with Dulbecco's Modified Eagle Media comprising 4500 mg glucose/L, L-glutamine, NaHCO<sub>3</sub>, and sodium pyruvate with 10% fetal bovine serum, 1% HEPES buffer, and 1% penicillin-streptomycin. A Synergy HT Multimode Microplate reader from BioTek was used to take fluorescence and absorbance readings during assays. Overall, three experiments were run including a cell cytotoxicity assay, a study of the passive interactions between the BSA shell on PAnDs and the cells, and a study of the vaporization effects caused by close proximity vaporization under pulsed laser irradiation.

### 6.2.1 Photoacoustic nanoDroplet Cytotoxicity

Cell cytotoxicity of PAnDs was tested using an MTS assay. PAnDs, prepared as previously described ( $10^8$  PAnDs/ml), were used for this study. PAnDs (5 ml) were sterilized under ultra-violet light for 20 minutes. The sterilized PAnDs were then centrifuged and resuspended in sterile cell media at 5 concentrations ranging between 12.3 mg/ml and 0.13 mg/ml of total droplet weight to volume (12.3, 6.15, 1.23, 0.49, and 0.13 mg/ml). Samples of PEGylated gold nanorods and blank droplets were also created and diluted to match the concentration of the 12.3 mg/ml PAnD solution. Two 96-well plates were seeded with  $1 \times 10^4$  A431 endothelial cancer cells or MDA-MB-231 breast cancer cells per well, and incubated at 37°C and 5% CO<sub>2</sub> for 24 hr before incubation with PAnDs. The media was aspirated, and the new media containing varying concentrations of PAnDs and the control samples were placed in the predetermined wells. The plate was incubated for another 30 hr at 37 °C and 5% CO<sub>2</sub>. The media was removed via aspiration, the wells were gently washed with DPBS, and clean media was added. An initial absorbance was measured using a plate reader at 490 nm. Therefore, the optical density in the well is directly related to the activity, or viability, of the cells. Next, 10 µl of 3-(4,5-dimethylthiazol-2-yl)-5-(3-carboxymethoxyphenyl)-2-(4-sulfophenyl)-2H-tetrazolium (MTS) was added to each well and incubated at 37 °C and 5% CO<sub>2</sub> for 2 hr. The mitochondrial activity in viable cells reduces the MTS to a formazan product that has a peak optical absorbance at 490 nm. A final absorbance reading was taken after the 2 hour incubation. The initial absorbance reading of each well was subtracted from the final reading to determine the relative viability values. A multivariate analysis of variance was used to determine statistically significant different mean viabilities between the control wells and the wells incubated with varying concentrations of PAnDs. Plots were created

showing viability relative to the control cells that were only incubated with normal cell culture media.

### **6.2.2 Passive Targeting Via Bovine Serum Albumin**

BSA has been shown to passively target tumors via superficial binding to tumor tissues. To test this effect, PAnDs were synthesized as previously described. To create unloaded nanodroplets, 2 mL DPBS, 120  $\mu$ l of BSA, at a concentration of 0.2 mg/ml, and 250  $\mu$ l of perfluorocarbon were added to a 5 ml glass vial, briefly vortexed at high speed, and then sonicated at room temperature for 1 minute. The sample was centrifuged twice at 14000 rcf for 30 seconds and resuspended in clean DPBS twice to remove any excess protein. The sample was then diluted by mixing 100  $\mu$ l of the sample with 900  $\mu$ l of water. The gold nanorod control suspension was prepared by adding a 1:1 ml ratio of fluorinated gold nanorods and 1.5% w/v solution of Tween 20 surfactant. To prepare cell samples for microscopy, glass coverslips were placed at the bottom of each well in a 6-well plate. A431 and MD-MBA-231 cells were all incubated in their respective well plates at a concentration of  $1.6 \times 10^5$  cells per well and left to adhere to the coverslips overnight. The media was first removed from each well via aspiration, and the cells were washed with 1 ml of PBS to remove any excess cellular debris. Then, 1 ml of each sample (loaded nanodroplets, unloaded nanodroplets, and gold nanorods) was added to each well. 1 ml of DMEM was also added to each well to bring the final volume in each well to 2 ml. The samples were then incubated for an hour before being imaged using a 40X objective with bright field and dark field microscopy. After being imaged, each glass cover slip was rinsed gently in PBS solution, so as not to remove any cells, but only dislodge unbound PAnDs. After the wash step, 1 ml of fresh DMEM media was added to each well and the plates were allowed to incubate for an additional hour. After

incubation, the cover slips were removed and images were taken again using bright field and dark field microscopy.

### **6.2.3 Cellular Response to Vaporization of Photoacoustic nanoDroplets**

To study the effect of PAnD vaporization on cell viability and cell membrane disruption a multifaceted experiment was planned. First, in order to determine if PAnD vaporization disrupts, either temporarily or permanently, the cell membrane, 3 kDa fluorescently-labeled (Cascade blue) dextran and ethidium bromide (EthD-1) were used. These compounds are normally membrane impermeable. Fluorescent dextran is routinely used to monitor trans-membrane delivery<sup>24,25</sup>. Ethidium bromide will only fluoresce red when in contact with nuclear materials found inside the cytoplasm. Therefore, if a cell that is determined to be viable via other methodologies (MTS assay) has either dextran (fluorescing blue) or ethidium bromide signal (fluorescing red), it is likely that there was a temporary membrane disruption. Calcein green was added to ensure labeled cells that were initially viable as the intracellular esterases remove the acetoxymethyl (AM) esters which cause the molecule to fluoresce green. If a cell were to perish due to vaporization, the cell would still fluoresce green due to the initial exposure during its viable period but also red due to the interaction of the ethidium bromide (EthD-1) with the exposed cytoplasm. Next, to determine long term viability of the cells after close proximity vaporization of PAnDs, an MTS ((3-(4,5-dimethylthiazol-2-yl)-5-(3-carboxymethoxyphenyl)-2-(4-sulfophenyl)-2H-tetrazolium) assay was performed, as described in Section 6.1.1.

Four 96 well plates seeded with 5,000 cells per well of A431 and MDA-MB-231 cancer cells, respectively, were incubated for 24 hours at 37 °C at 5% CO<sub>2</sub> to give a resulting  $1 \times 10^4$  cells per well at the start of the experiment. Plates had rows dedicated to

cells only, cells only with laser irradiation, five concentrations of PAnDs, gold nanorods only, and empty perfluorocarbon droplets. In one plate of each cell type the following were added to each well: 100  $\mu$ l of a combined 2  $\mu$ M calcein AM and 4  $\mu$ M EthD-1 solution, 100  $\mu$ l of 0.2 mg/ml dextran solution, and either 50  $\mu$ l of PAnDs at varying concentrations ( $10^8$  PAnDs/ml (60 mg/ml) to  $10^4$  PAnDs/ml (6.0  $\mu$ g/ml), 50  $\mu$ l of gold nanorod solution at the same concentration of rods contained in the  $10^8$  PAnD solution, or 50  $\mu$ l of empty perfluorocarbon droplets ( $10^8$  droplets/ml) into the corresponding wells. Each condition was repeated in six wells to allow for statistical analysis. The other two plates were loaded in the same manner, without including the calcein and EthD-1 stains. Next, all columns, except control cells (no laser exposure), underwent 10 seconds of pulsed lasing at 780 nm using a fluence of 3 mJ/cm<sup>2</sup>. All plates were then rinsed once with DPBS and 100  $\mu$ l of fresh cell culture media was added. The plates without fluorescent dyes were allowed to incubate for either 4 or 24 hours longer to study immediate and longer term effects. The other plates were read using a plate reader at three conditions: calcein (Ex 485 Em 530), EthD-1 (Ex 530 Em 645), and dextran (Ex 400 Em 420). The data was collected and analyzed for intensities relative to the control wells. Error bars represent one standard deviation. Microscopy images using a Leica inverted microscope with a 40X objective equipped with epi-fluorescence and bright field capabilities were also acquired to verify the location of the fluorescence signal (either from cells or background). The plates that were incubated longer were then used for MTS assays to determine cell viability. Initial absorption readings were taken at 490 nm to set a baseline for each well. In each well 10  $\mu$ l of CellTiter 96® AQueous Non-Radioactive Cell Proliferation Assay (MTS) from Invitrogen was added and allowed to react for two hours. Then, a second absorption reading was taken at 490 nm. The “before” reading was subtracted from the “after” reading and all data were normalized to the average OD of the

control wells to plot relative viability with respect to the control cells. Error bars represent one standard deviation.

## **6.3 RESULTS AND DISCUSSION**

### **6.3.1 Photoacoustic nanoDroplet Cytotoxicity**

The cellular cytotoxicity of PAnDs when passively incubated with cells for over 30 hours was investigated. The relative viability of the cells as compared to control cells is presented in Fig 6.1. After evaluating the conditions with an F test for multivariate ANOVA, it was found that none but one of the test conditions had a p-value of less than 0.05, indicating that the null hypothesis that there is no difference in means between conditions cannot be rejected. The one group that did appear statistically significantly lower than the control group were the A431 cells incubated with gold nanorods. Under microscopic inspection, crystals of CTAB, the surfactant used to cause isotropic growth during gold nanorod synthesis, were found. CTAB is known to be highly cytotoxic. It is likely that for this study, not all of the CTAB was removed from the gold nanorod solution before being added to cell culture. This is unlikely to occur in PAnDs as the gold nanorods encapsulated within them have undergone a two phase ligand exchange in order to be soluble in perfluorocarbons, whereas the gold nanorods used as the gold nanorod control in this experiment only had undergone the first step of the ligand exchange, therefore not all CTAB was likely to be removed. Interestingly, even though the same amount and type of gold nanorods were used for both A431 and MDA-MB-231 cells and both sets of wells showed visible CTAB crystals, A431 cells seem to be much more sensitive to CTAB presence than MDA-MB-231 cells. In future studies to avoid any possible contamination with CTAB, fluorinated gold rods could be used and made soluble by the inclusion of Tween20. Overall these studies indicate that with the final

synthesis methods, PAnDs up to 12.3 mg/ml total w/v (much higher than a typical dosage would entail) do not seem to cause cytotoxic effects in these cell lines. In the future, more studies in non-cancerous cell lines should be conducted to ensure non-cytotoxicity in less robust cell culture lines.

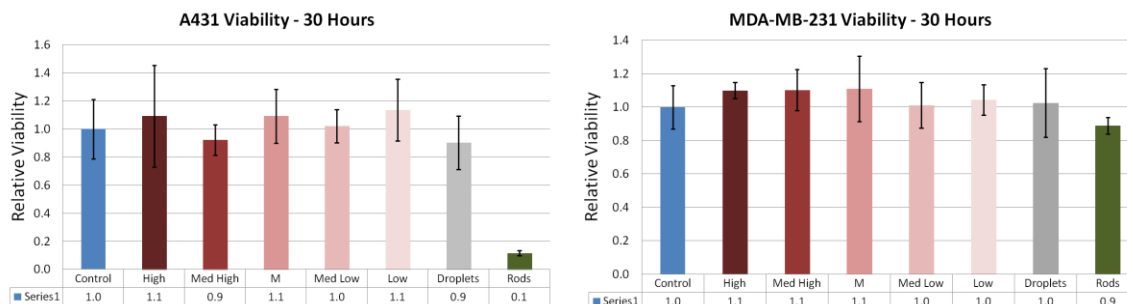


Figure 6.1: Relative viability of A431 and MDA-MB-231 cells incubated with varying concentrations of PAnDs, PEGylated gold nanorods, and empty perfluorocarbon droplets for 30 hours as compared to control cells.

### 6.3.2 Passive Targeting Via Bovine Serum Albumin

After PAnD incubation with cells for 2 hours, and several washes to remove free droplets, the cells were examined under microscopy to visualize passive droplet attachment to cells. The resulting images in bright field and phase microscopy are shown in Fig. 6.2. The MD-MBA-231 had lower confluency than the A431 as evident from the images. However, PAnDs are still shown clustering around cells in both cell lines. This is after several washings with DPBS, and even though there are a few residual droplets in the backgrounds of the images, the concentration of PAnD attached to the cells is much larger than that of the background particles. Especially dense populations are noted with red arrows in the bright field images. PAnDs are easy to distinguish due to their small size and spherical shape. Furthermore, they appear particularly bright in phase microscopy images. This study indicates that there may be passive targeting of PAnD to

cell membranes through the interactions of albumins and specific target receptors, which may help with PAnD accumulation in diseased tumor tissues.

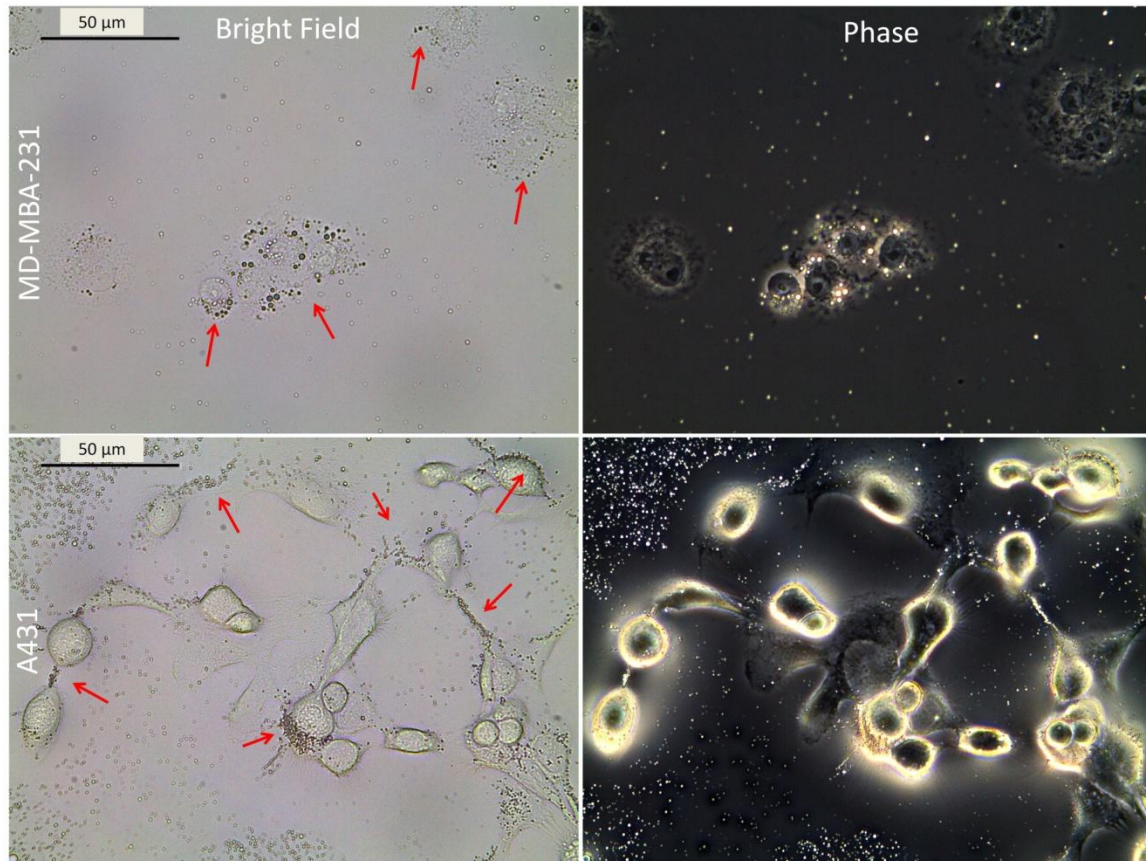


Figure 6.2: Bright field microscopy images of cells (A431 and MD-MBA-231) incubated with PAnDs.

### 6.3.3 Cellular Response to Vaporization of Photoacoustic nanoDroplets

After exposure to pulsed laser irradiation and vaporization of PAnDs, cells were examined using bright field and fluorescence microscopy. Using three band-pass filter cubes to receive red, green, and blue signals, the location of the various dyes was determined. All cells and conditions show bright green fluorescence corresponding to the calcein green stain for cell viability. Furthermore, all cells in all conditions have blue

fluorescent signal located outside the cells with no internalization. However, when examining the red fluorescent signal from reacted ethidium bromide, it is clear that the cells with blank droplets and nanorods only have red signal corresponding with dead cell material as confirmed with bright field microscopy while cells incubated and irradiated with PAnDs have co-localized red fluorescence inside all cells. This red signal increases with PAnD concentration. These effects are shown in Fig. 6.3 with composite bright field and fluorescent images and the grey scale versions of the color filtered fluorescent signals.

These results indicated that all of the cells in all conditions started in a healthy viable state as they all fluoresce green. Furthermore, the dextran blue fluorescence is inconclusive in terms of cellular uptake because no signal is shown inside the cells, and almost entirely surrounding the cells. This is thought to be because dextran and BSA very actively bind together<sup>26</sup>. Therefore, in samples with more BSA, such as the blank droplets and higher concentration of PAnDs, the dextran binds to the BSA which binds to the culture plate surface and are cannot be rinsed off without disturbing the cells. There is significantly less signal from the nanorods-exposed cell sample, which has not been exposed to BSA, and therefore the dextran can be rinsed more thoroughly from the cell culture and culture plate surface. This also explains why no blue signal can be detected within the cells as the dextran is either bound to BSA and cannot enter the cells during vaporization or there is no vaporization due to the lack of PAnDs. Finally, the signal from the ethidium bromide is minimal. In conditions where no vaporization occurs (nanorods only and blank droplets), the only red fluorescent signal is correlated with dead cell material, which can be confirmed by examining the image in bright field settings. However, in conditions where vaporization occurred, there is a very faint red fluorescent signal directly located within the cells which could indicate that an increase in the

number of vaporization events directly correlates with the cell membrane poration and increase in ethidium bromide uptake. The other cause could be that vaporization is causing cell death which would allow ethidium bromide to permeate a disrupted cell membrane, but the MTS cell viability studies later in this section preclude that conclusion. However, most likely, this red signal is the results of the color filters of the microscope incorrectly filtering green signal, and relaying it as red signal. These results are merely qualitative from examining images, so quantitative readings were taken using a fluorescent plate reader.

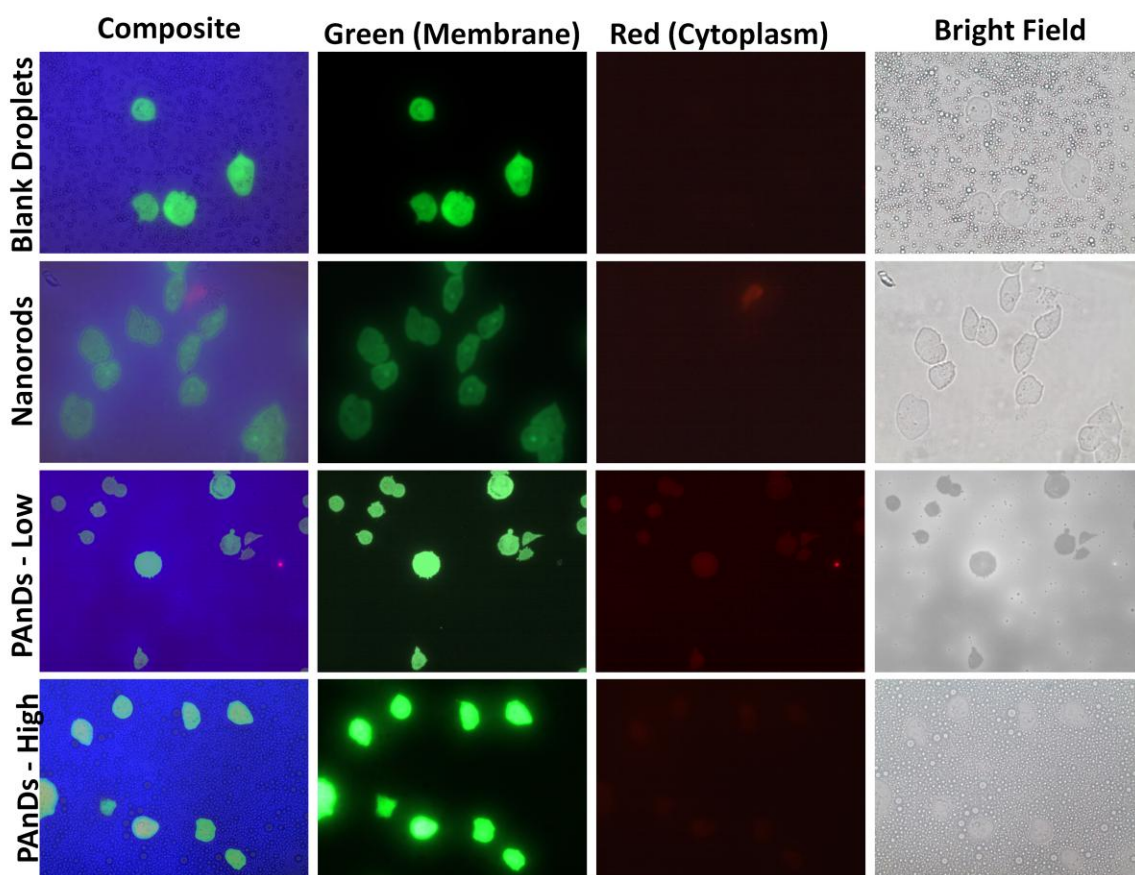


Figure 6.3: Composite bright field and three color fluorescence images of cells which were exposed to vaporization of PAnDs at high and low concentrations or exposed to pulsed laser irradiation while surrounded by either gold nanorods or empty perfluorocarbon droplets. Spatially co-registered red and green signal appear yellow in the composite images.

The three different colors of fluorescent signal were all quantified using a fluorescent plate reader. Since the blue dextran signal was inconclusive, the results were not included here. The relative levels of green/"alive" signal and red/"dead" (but more so referring to any appearance of cell membrane permeation) signal are shown in Fig 6.4 for both A431 and MDA-MB-231 cell lines. Interestingly, the conditions with varying concentrations of PAnDs show a larger green fluorescent signal than control cells alone

or control cells that underwent pulsed laser irradiation. This indicates that the vaporization, not the pulsed laser irradiation, is having a direct affect on the cellular activity of the cell lines. This could potentially be due to the stress of having to repair cell membrane poration or heat shock proteins in a heightened state of activity. However, more surprisingly, the red signal actually shows a decrease in the signal level, in complete contradiction to the fluorescent microscopy images. While this decrease in red signal does correlated with the idea of the increased green signal commenting on the enhanced cell viability of cells according to the green signal, more likely these results are due to the difference in filters used in the microscopy and plate reader. The microscope used direct band-pass color filters for each color, while the plate reader uses long-pass filters. Considering that the absolute value of the green signal is much higher than that of the red signal, and the emission spectrum of the green dye slightly overlaps with the red emission signal, the long-pass red filter would give a more accurate reading due to collection of more of the red signal, suggesting that the plate reader had more accurate estimations of fluorescent signal and the red signal detected in the microscopy images was the results of the higher intensity of green signal as compared to red signal. This would indicate that little ethidium bromide diffused into the cells. The matter could potentially be resolved by rerunning the experiment without the green dye. Another possibility is that the red signal emitted from inside cells is highly scattered and not directly detected, in which this problem might not be able to be resolved. A control experiment was run where cells were only mixed with either none of the dyes, one or the other of the dyes, or both dyes at the same concentration and then fluorescently read to ensure that mixing the dyes does not cause reading interference. The total signal from the mixed dye wells equaled the fluorescent signal from the individual dyes and cells alone

(autofluorescence) combined, indicating that the setup of this experiment should provided viable results.

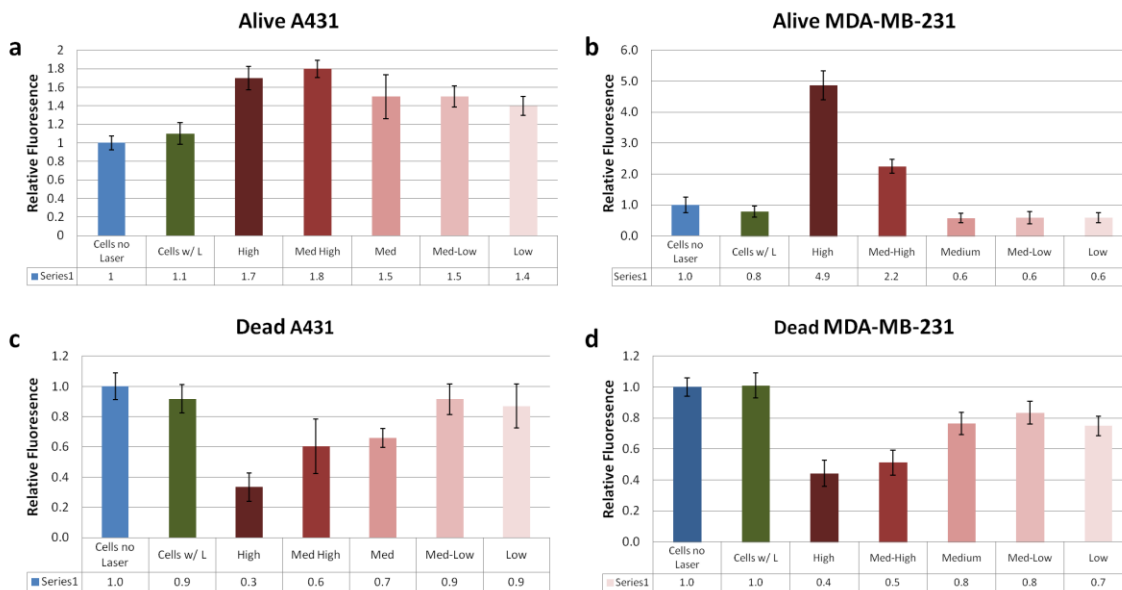


Figure 6.4: Relative levels as compared to untreated controls of “alive” stain, calcein/green, and “dead” stain, ethidium bromide/red, in two cell types after exposure to pulsed laser induced vaporization of PANDs and their components.

After exposure to laser irradiation and close proximity vaporization of PANDs, a MTS cell viability assay was used to look at immediate and long term affects, as well as to confirm secondary viability of cells using the calcein green “alive” stain. For both cell lines, when considering the conditions that include varying concentrations of PANDs, all showed an increased viability both immediately and 24 hours after irradiation/vaporization. The effect seemed to be steady in the A431 cell line, but showed dramatic increase in the MDA-MB-231 cell line over a 24 hour time period, increasing from a 1.7 to 5 relative viability. Furthermore, laser irradiation did not play an effect in the increased activity of the cells as cell that only underwent laser irradiation (either in

the presence of gold nanorods or by themselves) showed no overall increase in cell activity/viability. Furthermore, due to passive incubation studies in Section 6.3.1, it is known that the presence of PAnD does not increase (or decrease) overall cell viability, indicating that the actual vaporization of PAnDs is needed to cause this effect. It has been shown that albumin content can alter the results of MTS viability assays by reducing the products to formazan via the reactive thiol functional groups on the amino acids<sup>27,28</sup>. Not only does the inclusion of PAnD add thiol reactivity from the extra albumin, but also from the surface chemistry on the gold nanorods which are covered by hydrocarbon chains attached via thiol linkages. However, the albumin added by PAnDs is minimal compared to the percentages in the cell culture media (5-10% w/v) and there are also thiols on the PEGylated nanorods used in the control wells. These control wells do not show increased viability compared to the PAnD wells (both in passive and active incubation), and it is known that the signal is not saturated (preventing comparison of these possible effects in the passive incubation) as some of the wells do produce significantly higher absorptions given equal amounts of initial MTS solutions. In future studies, it would be easy to control for these possible effects however, but simply running the MTS in well where only cell media is present to account for any effect is might have.

As to why vaporization of PAnD causes an increased cell activity/viability, there are several possibilities. First, poration of the membrane caused by vaporization shock waves could increase cellular activity by activating heat shock proteins responsible for cellular repair, however this affect should be transient lasting only a short period of time, where as these studies indicate that the affect is long term, even increasing over time. A second explanation could be due to the high oxygen saturation levels of perfluorocarbon gases. Delivery of these gases to cells could increase the oxygen levels in the cells increasing activity/viability, however as these cells are incubated at 37 °C and the boiling

point of perfluoropentane is 27 °C, these gases should vaporized and dissipate relatively quickly. Thirdly, vaporization of PAnDs could have killed a sufficient number of cells that they were able to enter the exponential growth stage. However, this can be accounted for via microscopy, and in this experiment cell confluency was similar in all wells for both cell lines. Finally, generation of ultrasonic waves, which are known to stimulate cellular growth and healing, could produce this effect<sup>29-32</sup>. While the exact mechanisms are unknown, the application of ultrasound has been shown to stimulate protein synthesis, release of angiogenic factors, and cellular proliferation<sup>33</sup>. Therefore, as shown by these studies, PAnD do not hinder cellular viability when vaporized in close proximity to cells. Potentially, PAnDs can increase cell viability and growth, implying that PAnDs may have future use in therapeutic healing applications more than just for solid tumor therapy.

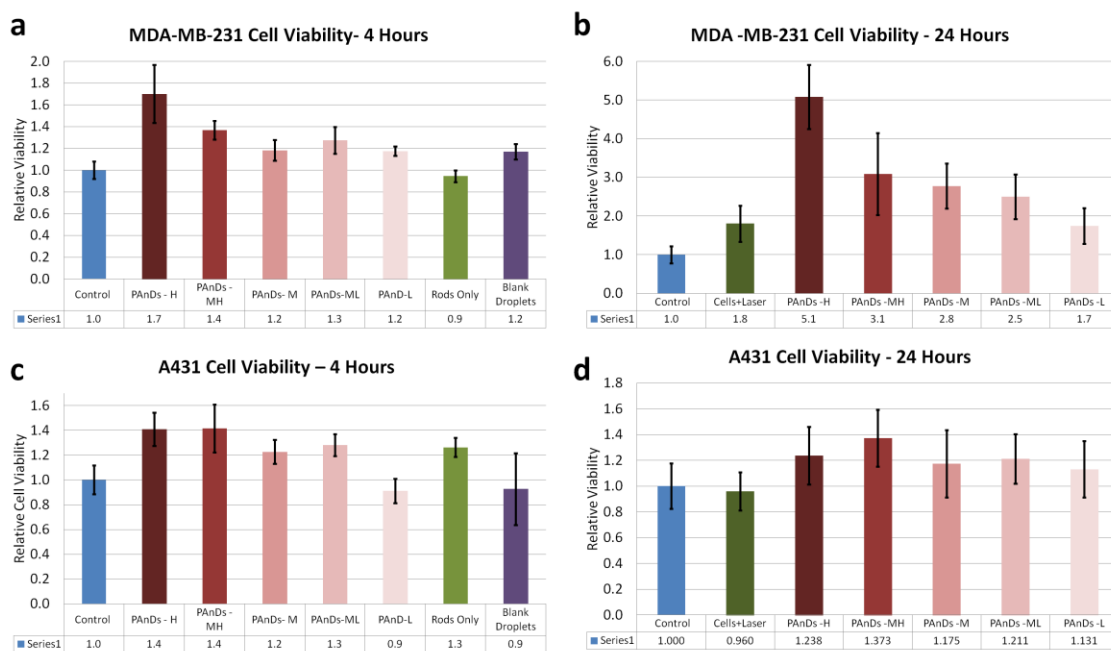


Figure 6.5: Immediate and long term cell viability assay results of MDA-MB-231 and A431 cells that underwent pulsed laser irradiation and close proximity vaporization of PAnD.

## 6.4 CONCLUSIONS

This chapter's focus was to investigate the passive and active interactions that PAnDs have with cells. The interactions need to be studied as PAnDs, even when eventually targeting to diseased tissues, will still circulate and interact with healthy cells. Through various experiments, it was determined that PAnD, in their final product stage, do not induce detectable cytotoxic effects in A431 and MDA-MB-231 cancer cell lines. Furthermore, due to the BSA shell that PAnDs are synthesized with, there is a small amount of non specific targeting to cell membranes. This targeting could potentially be greatly enhanced with covalent attachment of targeting moieties to the cell surface (Chapter 7). Finally, the effect of localized PAnD vaporization near cell membranes was studied. It was shown that vaporization does not have a negative impact on cell viability over time. In some cases the opposite effect was noticed, potentially due to the generation of ultrasonic shock waves which can induce cell proliferation and growth. These results indicate that not only are PAnDs most likely relatively inert in tissue environments, but they may also be useful in application to aid in tissue healing such as bone fractures, nerve damage, and muscle tears. Furthermore, PAnDs could potentially be used to activate certain types of cells for other purposes such as immune cells for disease control. Overall, PAnDs show promise of usage in biological settings, with minimal concern for the safety of the close proximity cells.

## 6.5 REFERENCES

1. Diaz-Lopez, R., Tsapis, N. & Fattal, E. Liquid Perfluorocarbons as Contrast Agents for Ultrasonography and  $^{19}\text{F}$ -MRI. *Pharm. Res.* **27**, 1-16 (2010).
2. Correas, J.M. & Quay, S.D. EchoGen emulsion: a new ultrasound contrast agent based on phase shift colloids. *Clinical radiology* **51 Suppl 1**, 11-14 (1996).
3. Lewinski, N., Colvin, V. & Drezek, R. Cytotoxicity of nanoparticles. *Small* **4**, 26-49 (2008).

4. Cosgrove, D. Ultrasound contrast agents: an overview. *Eur J Radiol* **60**, 324-330 (2006).
5. Dolan, M.S. *et al.* Safety and Efficacy of Commercially Available Ultrasound Contrast Agents for Rest and Stress Echocardiography: A Multicenter Experience. *Journal of the American College of Cardiology* **53**, 32-38 (2009).
6. Matsumura, Y. & Maeda, H. A new concept for macromolecular therapeutics in cancer chemotherapy: mechanism of tumoritropic accumulation of proteins and the antitumor agent smancs. *Cancer Research* **46**, 6387-6392 (1986).
7. Maeda, H., Wu, J., Sawa, T., Matsumura, Y. & Hori, K. Tumor vascular permeability and the EPR effect in macromolecular therapeutics: a review. *J Control Release* **65**, 271-284 (2000).
8. Torchilin, V. Tumor delivery of macromolecular drugs based on the EPR effect. *Adv. Drug Delivery Rev.* **63**, 131-135 (2011).
9. Tiruppathi, C., Finnegan, A. & Malik, A.B. Isolation and characterization of a cell surface albumin-binding protein from vascular endothelial cells . *Proceedings of the National Academy of Sciences* **93** , 250-254 (1996).
10. Sharma, R.I., Pereira, M., Schwarzbauer, J.E. & Moghe, P.V. Albumin-derived nanocarriers: substrates for enhanced cell adhesive ligand display and cell motility. *Biomaterials* **27**, 3589-3598 (2006).
11. Schnitzer, J.E. gp60 is an albumin-binding glycoprotein expressed by continuous endothelium involved in albumin transcytosis . *American Journal of Physiology - Heart and Circulatory Physiology* **262** , H246-H254 (1992).
12. *Textbook of human histology.* (Jaypee Brothers: 2006).at  
<<http://books.google.com/books?id=Ej22iANgNkoC>>
13. Li, T., Tachibana, K. & Kuroki, M. Gene transfer with echo-enhanced contrast agents: comparison between Albunex, Optison, and Levovist in mice--initial results. *Radiology* **229**, 423-428 (2003).
14. Miller, D.L., Pislaru, S.V. & Greenleaf, J.F. *Sonoporation: Mechanical DNA Delivery by Ultrasonic Cavitation.* *Somatic Cell and Molecular Genetics* **27**, 115-134 (Springer Netherlands: 2002).
15. Mitragotri, S. Healing sound: the use of ultrasound in drug delivery and other therapeutic applications. *Nature reviews. Drug discovery* **4**, 255-60 (2005).
16. Tsai, K.-C. *et al.* Differences in gene expression between sonoporation in tumor and in muscle. *J. Gene Med.* **11**, 933-940 (2009).
17. Li, Y.S., Davidson, E., Reid, C.N. & McHale, A.P. Optimising ultrasound-mediated gene transfer (sonoporation) in vitro and prolonged expression of a

- transgene in vivo: Potential applications for gene therapy of cancer. *Cancer Lett. (Shannon, Irel.)* **273**, 62-69 (2009).
18. Suzuki, R. *et al.* Cancer gene therapy by IL-12 gene delivery using liposomal bubbles and tumoral ultrasound exposure. *J. Controlled Release* **142**, 245-250 (2010).
  19. Cailleau, R., Olivé, M. & Cruciger, Q.V.J. Long-term human breast carcinoma cell lines of metastatic origin: Preliminary characterization. *In Vitro* **14**, 911-915 (1978).
  20. Yamamoto, T. *et al.* High Incidence of Amplification of the Epidermal Growth Factor Receptor Gene in Human Squamous Carcinoma Cell Lines. *Cancer Res.* **46**, 414-416 (1986).
  21. Cleator, S., Heller, W. & Coombes, R.C. Triple-negative breast cancer: therapeutic options. *The lancet oncology* **8**, 235-44 (2007).
  22. Nielsen, T.O. *et al.* Immunohistochemical and clinical characterization of the basal-like subtype of invasive breast carcinoma. *Clinical cancer research : an official journal of the American Association for Cancer Research* **10**, 5367-74 (2004).
  23. Atlanta: American Cancer Society, I. *Breast Cancer Facts & Figures 2011-2012*.
  24. Mogensen, C.E. The Glomerular Permeability Determined by Dextran Clearance Using Sephadex Gel Filtration. (2009).at  
<<http://informahealthcare.com/doi/abs/10.3109/00365516809076979>>
  25. Coromili, V. & Chang, T.M.S. Polydisperse Dextran as a Diffusing Test Solute to Study the Membrane Permeability of Alginate Polylysine Microcapsules. (2009).at  
<<http://informahealthcare.com/doi/abs/10.3109/10731199309117382>>
  26. Travis, J. & Pannell, R. Selective removal of albumin from plasma by affinity chromatography. *Clinica Chimica Acta* **49**, 49-52 (1973).
  27. KUANG TZU, H., YEN HAO, C. & WALKER, A.M. Inaccuracies in MTS assays: major distorting effects of medium, serum albumin, and fatty acids. *BioTechniques* **37**, 406-412
  28. Funk, D., Schrenk, H.-H. & Frei, E. Serum albumin leads to false-positive results in the XTT and the MTT assay. *BioTechniques* **43**, 178, 180, 182 passim (2007).
  29. Hart, J. The use of ultrasound therapy in wound healing. *Journal of wound care* **7**, 25-8 (1998).
  30. Mourad, P.D. *et al.* Ultrasound Accelerates Functional Recovery after Peripheral Nerve Damage. *Neurosurgery* **48**, (2001).

31. Hadjiargyrou, M., McLeod, K., Ryaby, J.P. & Rubin, C. Enhancement of Fracture Healing by Low Intensity Ultrasound. *Clinical Orthopaedics and Related Research* **355**, (1998).
32. Cook, S.D. *et al.* Improved Cartilage Repair After Treatment With Low-Intensity Pulsed Ultrasound. *Clinical Orthopaedics and Related Research* **391**, (2001).
33. Doan, N., Reher, P., Meghji, S. & Harris, M. In vitro effects of therapeutic ultrasound on cell proliferation, protein synthesis, and cytokine production by human fibroblasts, osteoblasts, and monocytes. *Journal of oral and maxillofacial surgery : official journal of the American Association of Oral and Maxillofacial Surgeons* **57**, 409-19; discussion 420 (1999).

## **Chapter 7: Molecular and Therapeutic Modifications of Photoacoustic nanoDroplets**

Photoacoustic nanoDroplets (PAnDs) have been shown to be excellent dual contrast agents for combined photoacoustic imaging. Furthermore, through cellular interaction studies, it was shown that their presence and optical activation does not cause harmful or negative effects on cells. However, PAnDs provide a very unique and voluminous environment for the encapsulation of therapeutic drugs, and an excellent surface for binding targeting moieties. This chapter focuses on the specific adaptations of PAnDs to include molecular targeting monoclonal antibodies on the surface, and the inclusion of high concentrations of chemotherapeutic drug in their cores. These adaptations allow PAnDs to be used not only as a dual contrast agent, but also as a molecularly specific therapeutic agent with triggerable drug release. The synthesis and preliminary experiments testing these adaptations are described in this chapter.

### **7.1 INTRODUCTION**

In Chapters 4 and 6, the physical mechanisms of the activation of PAnDs were explored and how those mechanisms affect living cells was studied. These experiments showed that the ultrasonic shock wave generated produced by optically triggered PAnD does not cause harmful effects to cells and may potentially stimulate cell proliferation (Fig. 6.5). While these mechanisms, when used on their own, can be beneficial to cells, the same effects combined with therapeutic agents can be used as therapy for diseased tissues, such a solid cancerous tumors. If PAnDs are loaded with chemotherapeutic drugs, the induced cellular sonoporation that occurs when PAnDs are activated would allow for increased intracellular delivery, and therefore efficacy, of these therapeutic compounds. Not only can PAnDs be used for nonspecific drug delivery, but with the addition of

superficial, molecularly specific targeting moieties, a larger percentage of PAnDs would accumulate in the specific target site, allowing for cell-specific treatment of disease. Localized drug delivery has resulted in a significant decrease in the morbidity associated with chemotherapeutic drugs due to lower dosages of drug delivery to non-diseased tissues reducing systemic toxicity<sup>1-4</sup>. Therefore, PAnDs modified with molecular targeting moieties and encapsulated therapeutics could be very beneficial for cancer imaging, diagnosis, and therapy.

Many chemotherapeutics show great promise in treating cancers, but due to their organic nature and the challenge of creating formulations for clinical use, they cannot be exploited to their full potential. One such drug, Paclitaxel, a mitotic inhibitor which prevents microtubule function, was discovered in 1967 when it was isolated from the bark of the Pacific yew tree<sup>5,6</sup>. Due to the highly hydrophobic nature of Paclitaxel, it is suspended in a polyethoxylated castor oil, known as Cremophor EL<sup>5</sup> for clinical usage. However, Cremophor EL causes hypersensitivity reactions<sup>7</sup> limiting the dosages of Paclitaxel that can be used. Therefore, many encapsulation methods have been researched to try to eliminate the need for a solubilizing agent for aqueous delivery including liposomes<sup>8,9</sup>, polymers<sup>10-13</sup>, emulsions<sup>14,15</sup>, and a now clinically available albumin bound version known as Abraxane<sup>16</sup>. These formulations have been successful in preventing delivery side effects, allowing control of drug release pharmacokinetics, and even enhancing site specific delivery of Paclitaxel. PAnDs, which comprise a large hydrophobic core and albumin surface, present an optimal environment to load Paclitaxel for therapeutic treatment.

While including drugs in a nano-formulation can aide in site specific drug delivery and lowering of systemic toxicity, targeting drug delivery can further aid in that endeavor. Over the past three decades, extensive research has been conducted to

specifically target diagnostic and therapeutic nanocarriers to cancer cells. Preliminary studies in the 1980s sought to passively target nanoparticles to tumors by exploiting the enhanced permeability and retention (EPR) effect upon injection<sup>17,18</sup>. While passive targeting has been used as a strategy for nanocarriers currently undergoing clinical trials, there are several limitations to this strategy<sup>19</sup>. For example, nanocarriers that are conjugated to therapeutics may non-selectively bind to and damage healthy tissues. Passive targeting of contrast agents only allow for imaging structures with generally poorly formed vasculature<sup>20</sup>. Also, the strategy is limited by the fact that some human tumors, unlike their small animal models, exhibit a weak and differential EPR effect leading to an uneven distribution of contrast agents throughout the cancerous tissue<sup>21,22</sup>. Therefore a strategy that relies on specific binding between contrast agent and the diseased cells is needed to overcome these challenges.

Active targeting, an alternative targeting strategy, overcomes the restrictions of passive targeting. This strategy entails conjugating targeting ligands that can selectively bind to receptors that are over-expressed on diseased tissues to the surface of contrast agents. Various ligands including monoclonal antibodies, antibody fragments, vitamins, glycoproteins, carbohydrates, and peptides have been used as targeting moieties<sup>23</sup>. The ligands can either be covalently attached to the agent's surface or non-covalently conjugated using various binding chemistries. In order for active targeting to be successful, several requirements must be met. First, the agents must bind with increased selectivity to an antigen overexpressed in tumor cells with minimal binding to non-cancerous cells. Secondly, the targeted receptor should be selectively expressed or overexpressed on cancer cells. Thirdly, the contrast agents should have a higher binding affinity for targeted cells via multivalent targeting moieties. Finally, targeted agents must withstand physical and biological barriers *in vivo* to become attached to the desired cells.

To actively target nanocarriers to cancer cells, the selection of the receptor to be targeted must be carefully considered. One of the major requirements needed to achieve active targeting is that the chosen receptor must be selectively overexpressed on diseased cells when compared to normal cells. Studies evaluating receptor density and therapeutic efficacy of drug loaded nanocarriers have determined that a minimum of  $10^4$ - $10^5$  receptors are necessary to observe sufficient targeting and an improvement in therapeutic efficacy<sup>24,25</sup>. Additionally the cell receptor should be expressed in all cells of the diseased tissues and be vital to cellular function<sup>26</sup>. Numerous receptors have been proposed for the active targeting of contrast nanoagents. For example studies have been conducted on ErbB2, a growth factor that is over-expressed in 30% of human breast carcinomas<sup>27</sup>. A study using a Doxil loaded liposome system conjugated to an antibody targeted to ErbB2 demonstrated a faster reduction in tumor volume in mice injected with breast tumor cells<sup>28</sup>. Folate receptors have also been studied as a potential nanocarrier target, as they are often overexpressed in various cancer cells including ovarian, endometrial, and kidney cancer<sup>29</sup>. A study conducted by Pan et al demonstrated that liposome complexes loaded with doxorubicin and targeted with folate had better therapeutic outcomes than non-targeted loaded liposomes and freely circulating doxorubicin<sup>30</sup>. However, in the work presented here, a very specialized application will be focused on: triple-negative breast cancer. This focus is due to the special abilities of PAnDs, including their activation at low energy and the production of high photoacoustic signal, allowing for high depth imaging. Triple-negative breast cancers (15% of all breast cancers<sup>31</sup>) are particularly difficult to treat with current therapeutics that target Human Epidermal Growth Factor Receptor 2 (HER2), Estrogen Receptor (ER), and/or Progesterone Receptor (PR), none of which are expressed in triple-negative breast cancer. However, triple-negative breast cancer does often (~50% of the time) overexpress Endothelial

Growth Factor Receptor (EGFR)<sup>31</sup>. Therefore, in these studies, PAnDs will be targeting using anti-EGFR antibodies.

While there are currently many strategies to link mAbs to the surface of protein nanocarriers<sup>32</sup>, one specific method will be focused on here, the biotin-avidin bridge. The biotin/avidin link is one of the strongest non-covalent bonds known<sup>33</sup>, is biologically compatible as avidin and biotin are both found naturally in the body, and both are easily obtainable through most chemical suppliers. Furthermore, antibodies have several methods to undergo “biotinylation” or “avidinylation”, the attachment of these molecules to the constant portion of antibodies, and can often be purchased directly in the conjugated form. Biotin and avidin can be conjugated to fluorescent dyes for easy experimental verification. For these reasons, PAnDs will be targeted via mAbs attached to the albumin shell via a biotin/avidin bridge.

## **7.2 METHODS**

The methods described here explore two techniques that could be used to attach monoclonal antibodies to PAnDs in the future, and the initial drug loading and passive drug diffusion studies. Two methods of antibody attachment are described to determine which is a more effective method of molecular-specific PAnD accumulation. One method describes biotin incorporation into the BSA shell, while attaching antibodies which have an avidin strategically attached to the particles. The other method describes incorporation of avidin into the BSA shell and attachment of biotinylated antibodies.

### **7.2.1 Molecular Targeting via a Biotin – Avidin Bridge**

The following protocol was performed to incorporate biotinylated BSA into the nanodroplet shell in order to create a biotin-avidin bridge, which could later be conjugated to antibodies to create molecularly specific PAnDs. First, 2 ml of phase-

transferred gold nanorods (synthesis described in Chapter 2) were evaporated in a 5 ml glass vial until all the solvent was evaporated. Then, 2 ml of water was added followed by 120  $\mu$ l of a 0.2 mg/ml solution of BSA. 16  $\mu$ g of Biotin-BSA was also added to the sample, followed by 250  $\mu$ l of perfluorocarbon. The mixture was then rapidly vortexed for a few seconds and sonicated at room temperature for one minute. Next, the particles were extruded through a lipid mini-extruder to create a uniform size distribution and washed to remove unbound protein and unencapsulated gold. To test for the creation of a biotin/avidin bridge, fluorescently labeled avidin was used. To this end, 64  $\mu$ l of a 0.25 mg/ml solution of FITC conjugated avidin was added to the vial. The 5 ml vial was then wrapped in aluminum foil to prevent photobleaching. The sample was allowed to rotate on a stir plate for an hour and then the sample was refrigerated overnight. The sample was spun down and washed twice to remove any unbound FITC-avidin. Then, the sample was imaged using bright field and fluorescence microscopy using a 40X objective.

### **7.2.2 Molecular Targeting via an Avidin – Biotin Bridge**

This protocol was followed to incorporate avidin into the nanodroplet shell in order to create an avidin-biotin bridge which could later be conjugated to biotinylated antibodies. First, 2 ml of fluorinated gold nanorods were evaporated in a 5 ml glass vial until all the solvent was evaporated. Next, 2 ml of water was then added followed by 120  $\mu$ l of a 0.2 mg/ml solution of BSA. Then, 180  $\mu$ l of a 0.4 mg/ml solution of avidin was also added to the sample followed by 250  $\mu$ l of perfluorocarbon. The mixture was rapidly vortexed for a few seconds and then sonicated at room temperature for a minute. The particles were microextruded and washed to remove unbound protein and unencapsulated gold. Then, 120  $\mu$ l of a 0.25 mg/ml solution of FITC conjugated biotin was added to the vial to act as a visual test of avidin-biotin bridge formation. The 5 ml vial was then

wrapped in aluminum foil to prevent photobleaching. The sample was allowed to rotate on a stir plate for an hour and then the sample was refrigerated overnight. The sample was spun down and washed twice to remove any unbound FITC-biotin. Then, the sample was imaged using bright field and fluorescence microscopy at 40X.

### **7.2.3 Drug Loading Synthesis – Paclitaxel**

Creating drug loaded PANs was done via a simple modification of the original synthesis method described in Chapter 2. This method creates 9 ml of PANs with encapsulated Paclitaxel at 20 mg/ml of drug concentration. This is an extremely high level of drug loading. First, 36 mg of Paclitaxel were dissolved in 2 ml chloroform (20 ml glass scintillation vial). The chloroform was evaporated off in order to deposit a thin film of Paclitaxel onto the bottom of the container. Following, 1.8 ml of mineral oil was added and sonicated for 20 minutes to resuspend Paclitaxel in oil. Next, 0.72 ml of perfluoropentane was added to the container with the Paclitaxel/mineral oil mixture. Then, similar to previously described methods in Chapter 2, 1.72 ml of BSA (2 mg/ml) and 5.76 ml of nanopure water were added to the container. The solution was vortexed for 15 seconds and then sonicated in a bath sonicator for 15 mins. This procedure was used to create drug loaded PANs for the characterization studies. For the fluorescent imaging study described below, the same concentration of a fluorescently labeled Paclitaxel was loaded following the methods described above. To characterize drug loading in PANs, mass-spectroscopy was performed to qualitatively identify the constituents of a control sample of Paclitaxel in chloroform, the drug loaded PANs, and the supernatant removed from drug loaded PANs. A control sample of Paclitaxel in chloroform at five times loading concentration was used to determine the peak at 876.17 and 877.07 indicating the molecular weights of Paclitaxel with single or double

protonation. The sample was centrifuged and the PAnDs were separated from the supernatant. Also, fluorescently labeled Paclitaxel was loaded into the PAnDs and examined using fluorescent microscopy. These techniques were used to verify drug loading into PAnDs.

#### **7.2.4 Passive Paclitaxel Drug Release**

In order to study the passive drug release, PAnDs loaded with oil droplets containing a known concentration of Paclitaxel were placed into an aqueous salt solution. At defined time points, the suspensions of nanocarriers in the salt solution were filtered through a 0.1 $\mu$ m syringe filter and the filtrate decanted into clean glass containers. The filtrates were combined with equimolar aqueous solutions of sodium chloride as well as a portion of chloroform in order to form a 1:2 volume fraction of aqueous and organic phases.

The experiment featured three sample groups (A,B,C) each with six time points (2, 12, 36, 48, and 72 hours). Each sample contained 0.5 ml PAnDs synthesized as described in Section 7.2.3 and 0.5 ml 2M sodium salicylate to solubilize any released drug<sup>34</sup>. The concentration of salt used in the release medium was experimentally determined to be capable of dissolving the quantity of drug used in the experiment. The samples were placed in 2 ml centrifuge tubes, housed within a rack on an automatic agitator. Over the entire course of the experiment, the agitator remained on the “medium” setting to prevent the sedimentation of carriers or released drug. At each time point, the corresponding sample from each of the three groups was removed from the rack and filtered with the syringe filter until 0.5 ml of filtrate was obtained. The pore size of the syringe filter was large enough to allow for the passage of drug and sodium salicylate, but

was sufficiently small to restrict the passage of bovine serum albumin (BSA) protein used to form the outer “shell” of the carrier particle.

Each 0.5mL portion of filtered 2 M sodium salicylate release medium was combined with an equal volume of 2 M sodium chloride solution in order to force dissociation of Paclitaxel with salicylate ions in aqueous phase due to the co-solubilizing function of salicylate ions. A 0.5 ml portion of chloroform was also added to each sample in order to exploit the improved solubility of Paclitaxel within organic media. As the samples were mixed by vortex-agitation, any drug present in the aqueous layer was transferred to the organic phase, where it could be detected by UV-vis spectrophotometry. To demonstrate total vaporization of the droplets after 75 hours, the vials were heated to 60 °C and the UV-vis readings were taken and compared to the expected released dosage.

### **7.3 RESULTS AND DISCUSSION**

The following are the results and discussion concerning the experiments done to modify PAnDs for targeted therapeutic applications. This includes two methods of attaching monoclonal antibodies, both of which incorporate the biotin-avidin bridge, a method for encapsulating chemotherapeutic drugs via suspension in oil droplets, and a study of the passive drug release from PAnDs which shows a slow, linear release of the drug due to progressive droplet vaporization.

#### **7.3.1 Molecular Targeting via a Biotin – Avidin Bridge**

Microscopy was used to detect fluorescent signals from the avidin and those images were compared with bright field images to co-localize the signal to the surface of PAnDs. These images have good agreement between the fluorescent signal and the location of the droplets. The fluorescent signal is stronger on the “edges” of the droplets

(due to the droplets 3D nature, more signal is located on the sides due to a higher collection of photons from that area due to depth of the droplet) indicating superficial placement of the fluorescent markers as expected. These images can be seen in Fig. 7.1. This method creates attachment sites for approximately 2500 avidin molecules per PAnD indicating that a sufficient number of antibodies could attach to each droplet to increase accumulation. A comparison of the two methods is given in the next section.

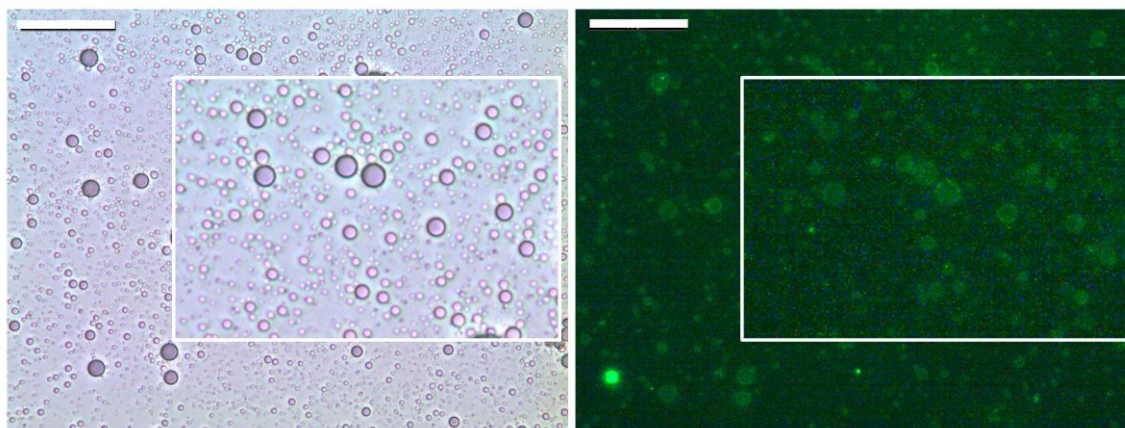


Figure 7.1: Bright field and fluorescent microscopy images of PAnDs with biotin incorporated into the shell and fluorescent avidin attached to complete the bridge. Each scale bar represents 50  $\mu\text{m}$ .

### 7.3.2 Molecular Targeting via a Avidin – Biotin Bridge

After attaching fluorescent biotin to the surface of PAnDs with avidin incorporated into the shell, bright field and fluorescent microscopy was used to verify co-location of the fluorescent signal to the surface of PAnDs. As shown in Fig. 7.2, fluorescent signal is correlated to the placement of the PAnDs, however, there is also clear aggregation of protein in other locations even after washing the samples. This method of antibody attachment creates approximately 10,000 binding sites for biotin per droplet. Both methods, due to their similarities, are relatively easy to synthesize, have

commonly available compounds, produce PAnDs that are stable and well formed, and produce PAnD solutions that are able to have fluorescently labeled ligands attached to their surfaces.

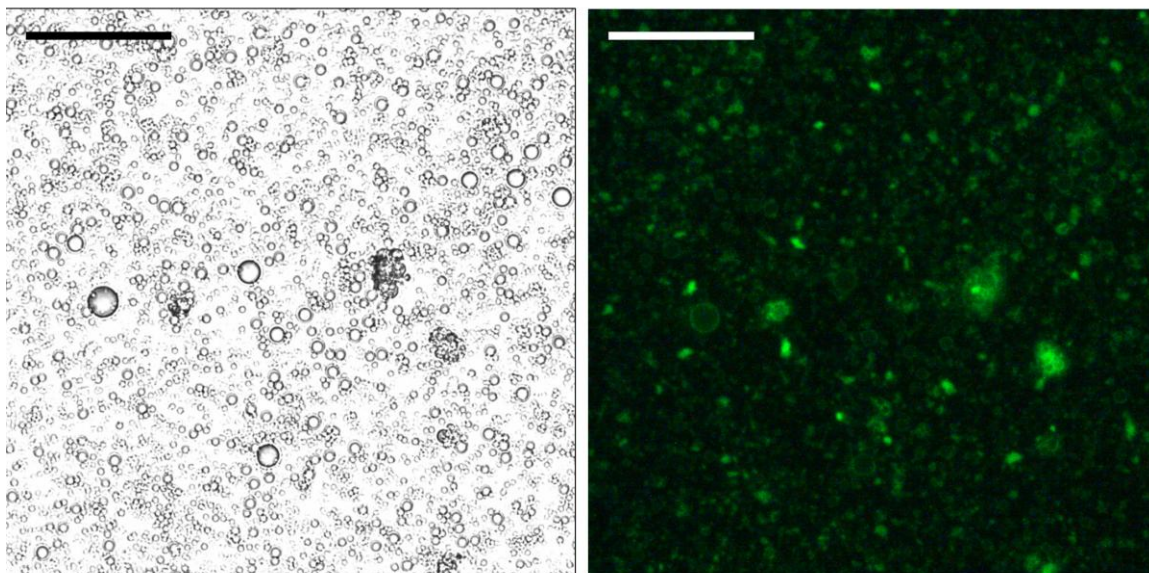


Figure 7.2: Bright field and florescent microscopy images of PAnDs with avidin incorporated into the shell with fluorescent biotin attached to complete the bridge. Each scale bar represents 50  $\mu\text{m}$ .

### 7.2.3 Drug Loading Synthesis – Paclitaxel

The method described above to incorporate Paclitaxel into the cores of PAnDs via an oil droplet suspension technique was characterized with two different methods. First, using mass spectroscopy, the samples were all read, and the PAnDs contained approximately twice the amount of Paclitaxel than the supernatant as shown in Fig. 7.3 (note the y-axis scales vary between samples, as indicated by the red circles). While this does not show complete specific loading, this is most likely due to the limited ability of the PAnDs to be separated from their liquid supernatant by centrifugation. The droplets have a combination of oil and perfluorocarbon that varies in the mixture amounts. As

mineral oil and perfluorocarbon are substances which are less and more dense than water respectively, this creates particle that have a various, overall densities. Therefore the mixture of PANds in the water phase does not pellet, creating instead a density gradient. It is highly likely that the “supernatant” sample also contained drug filled PANds, hence giving a false positive for free Paclitaxel in the water phase. This is also highly unlikely as Paclitaxel is highly insoluble in the water phase. Some amount might be expected due to the ability of Paclitaxel to bind to albumin, which is water soluble. However this binding is minimized by using an excess of PFC to BSA indicating that much of the albumin is used for droplet formation and little free protein should remain available in solution. However, these results indicate that a larger fraction of Paclitaxel is incorporated into the PANds than not. Therefore, these results are promising for indicating high levels of drug loading into the center of PANds.

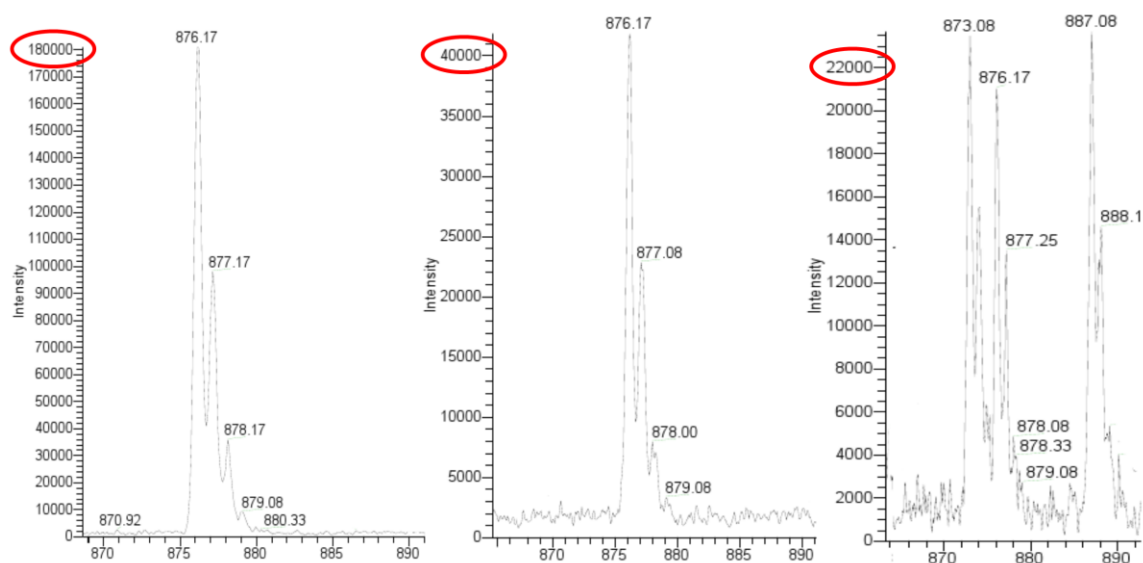


Figure 7.3: Mass spectroscopy readings of three samples from left to right: Paclitaxel in chloroform, Paclitaxel in PANds, supernatant from PANds. Paclitaxel reads at 876.17 and 877.07. Notice different scale on y-axis.

The loading of Paclitaxel was not only verified by mass spectroscopy, but also by fluorescent microscopy. Fluorescently labeled Paclitaxel was loaded into the droplets which were then imaged with both bright field and fluorescent microscopy. These images can be seen in Fig. 7.4. Due to some sample flow, the images do not completely correlate to location, but it is clear that the PANds are filled with fluorescent signal from the Paclitaxel and no signal is detected externally to these particles. Furthermore, unlike the surface targeting of PANds, the fluorescent signal is not only on the edges but fully homogenous through the droplets indicating a signal from the interior of the particles instead of only superficially. These results show that PANds can act as a drug delivery vehicle that can contain large concentrations of chemotherapeutic (up to 20 mg/ml in these experiments so far) for combined imaging and therapy of diseased tissues.

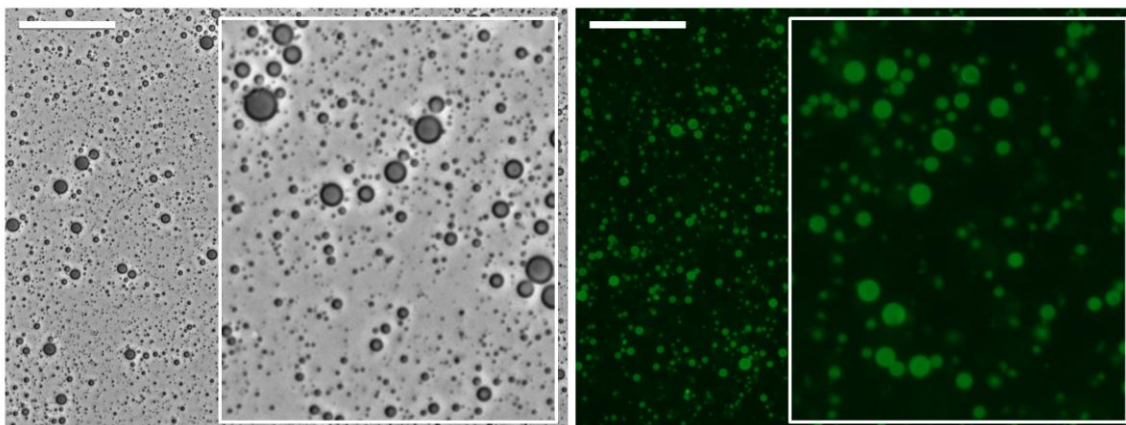


Figure 7.4: Bright field and fluorescent microscopy images of PANds loading with fluorescent Paclitaxel. Droplet position change is due to sample flow. White scale bar represents 50  $\mu\text{m}$ .

#### 7.2.4 Passive Paclitaxel Drug Release

A room temperature passive release study of Paclitaxel from PANds was done to look at diffusion of the drug versus release from vaporization of the droplets over time.

While this study provides conditions slightly favorable to long term stability of these particles (room temperature versus body temperature), the droplets were constantly agitated and suspended in a salt solution that is capable of dissolving Paclitaxel. The initial small burst in drug release is most likely due to Paclitaxel that had bound to the albumin unbinding and dissolving into solution, as Paclitaxel is known to bind to albumin<sup>16,35</sup>. It was found that after the initial 2 hour time period, a linear drug release profile was established. In a 72 hour time period, less than 3% of the total drug encapsulated was released from the droplets as shown in Fig. 7.5, indicating long term drug delivery potential. If the zero hour time point is not included, the data fits the equation  $\% \text{ Released} = 0.0262 * \text{Hours} + 1.001$  with a correlation coefficient of 0.987. If the zero hour time point is included, the data fits the equation  $\% \text{ Released} = 0.0316 * \text{Hours} + 0.725$  with a correlation coefficient of 0.8583. Extrapolating these results, the time when 100% drug release would occur is greater than 130 days. This is not likely however, as the PANDs would degrade at room temperature after a few weeks, and much more rapidly in the body, after a few days. It is important to note, however, that the long term or *in vivo* trends would vary from these predictions due to the increased body temperature and convective forces within the vasculature. Furthermore, the release trend is linear, indicating that the drug release is probably not due to passive diffusion out of the carriers, but from cumulative release during individual droplet vaporization. When these PANDs were vaporized (in this case by heating to 60 °C), for example during imaging and optical irradiation, the entire contents of the particles were be released in that location simultaneously. Over 76% of the drug was released in this experiment, however more was probably released but the saturation of the detection method was encountered at 4 mg/ml, or approximately 80% of the total encapsulated dosage. While these results are highly optimized, they are also not indicative of PANd stability and drug

leakage through the PAnD membrane during long term storage which could be maintained at 5 °C and not in a buffer such as sodium salicylate, which would impede drug diffusion through the PAnD membrane. These results suggest that PAnDs could be an excellent, remotely triggered organic drug delivery vehicle.

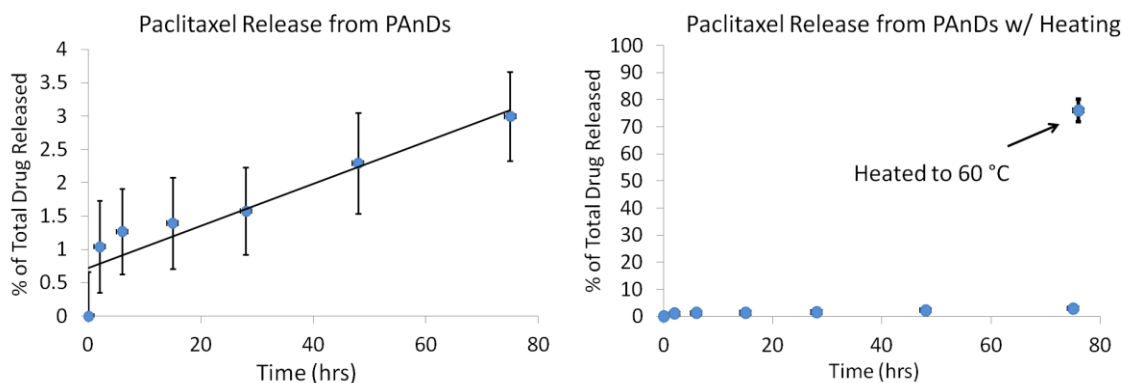


Figure 7.5: Passive Paclitaxel drug release as a percent of total drug encapsulation from PAnDs over a 72 hour time period resulting in less than 3% release. At the 76 hour time point, the droplets were destroyed by heating to 60 °C, releasing approximately 76% of the drug.

#### 7.4 CONCLUSIONS

This chapter focuses on using PAnDs as potential targeted drug delivery agents. While all of these studies are preliminary, all show promise for the future adaptation of PAnDs for specific molecular and therapeutic applications. It was demonstrated that molecularly specific moieties, such as monoclonal antibodies, could potentially be attached the surface of PAnDs via avidin/biotin bridges. Furthermore, PAnDs were adapted to act as highly concentrated, organic drug delivery agents that have the potential to be remotely triggered to deliver the entire dosage at the desired location and time. The future work for this portion of the overall project includes cellular interaction studies with antibody labeled PAnDs, to determine how that interaction varies compared to the

passive interactions noticed in Chapter 6. Furthermore, cell studies for efficacy of drugs for triggered release and in mouse models should be examined.

## 7.5 REFERENCES

1. Cho, K., Wang, X., Nie, S., Chen, Z.G. & Shin, D.M. Therapeutic nanoparticles for drug delivery in cancer. *Clin Cancer Res* **14**, 1310-1316 (2008).
2. Malam, Y., Loizidou, M. & Seifalian, A.M. Liposomes and nanoparticles: nanosized vehicles for drug delivery in cancer. *Trends Pharmacol. Sci.* **30**, 592-599 (2009).
3. Esenaliev, R.O. Radiation and nanoparticles for enhancement of drug delivery in solid tumors. *USPTO A*, 25 (2000).
4. Brown, D.M. *Drug delivery systems in cancer therapy. Cancer drug discovery and development* x, 390 p. (Humana Press: Totowa, N.J., 2004).at  
<<http://www.loc.gov/catdir/toc/fy042/2003042321.html>>
5. Wall, M.E. & Wani, M.C. Camptothecin and Taxol: Discovery to Clinic—Thirteenth Bruce F. Cain Memorial Award Lecture . *Cancer Research* **55** , 753-760 (1995).
6. Rowinsky, E.K. & Donehower, R.C. Paclitaxel (taxol). *N Engl J Med* **332**, 1004-1014 (1995).
7. Rowinsky, E.K., Eisenhauer, E.A., Chaudhry, V., Arbuck, S.G. & Donehower, R.C. Clinical toxicities encountered with paclitaxel (Taxol). *Seminars in oncology* **20**, 1-15 (1993).
8. Lundberg, B.B. Ether lipids enhance the cytotoxic effect of teniposide and paclitaxel in liposomes against leukaemic cells in culture. *Anticancer Drug Des* **12**, 503-513 (1997).
9. Tartis, M.S. *et al.* Therapeutic effects of paclitaxel-containing ultrasound contrast agents. *Ultrasound Med Biol* **32**, 1771-1780 (2006).
10. Danhier, F. *et al.* Paclitaxel-loaded PEGylated PLGA-based nanoparticles: in vitro and in vivo evaluation. *J Control Release* **133**, 11-17 (2009).
11. Azouz, S.M. *et al.* Prevention of local tumor growth with paclitaxel-loaded microspheres. *J Thorac Cardiovasc Surg* **135**, 1014-1021 (2008).
12. Soga, O. *et al.* Thermosensitive and biodegradable polymeric micelles for paclitaxel delivery. *Journal of Controlled Release* **103**, 341-353 (2005).
13. Liggins, R.T. & Burt, H.M. Polyether-polyester diblock copolymers for the preparation of paclitaxel loaded polymeric micelle formulations. *Adv Drug Deliv Rev* **54**, 191-202 (2002).

14. He, L., Wang, G.L. & Zhang, Q. An alternative paclitaxel microemulsion formulation: hypersensitivity evaluation and pharmacokinetic profile. *Int J Pharm* **250**, 45-50 (2003).
15. Lee, I.-H. *et al.* Stable paclitaxel formulations in oily contrast medium. *Journal of Controlled Release* **102**, 415-425 (2005).
16. Miele, E., Spinelli, G.P., Miele, E., Tomao, F. & Tomao, S. Albumin-bound formulation of paclitaxel (Abraxane ABI-007) in the treatment of breast cancer. *International journal of nanomedicine* **4**, 99-105 (2009).
17. Yuan, F. *et al.* Vascular Permeability in a Human Tumor Xenograft: Molecular Size Dependence and Cutoff Size. *Cancer Research* **55**, 3752-3756 (1995).
18. Matsumura, Y. & Maeda, H. A new concept for macromolecular therapeutics in cancer chemotherapy: mechanism of tumoritropic accumulation of proteins and the antitumor agent smancs. *Cancer Research* **46**, 6387-6392 (1986).
19. Duncan, R. Polymer conjugates as anticancer nanomedicines. *Nat Rev Cancer* **6**, 688-701 (2006).
20. Morawski, A.M., Lanza, G.A. & Wickline, S.A. Targeted contrast agents for magnetic resonance imaging and ultrasound. *Curr Opin Biotechnol* **16**, 89-92 (2005).
21. Jain, R.K. Transport of molecules, particles, and cells in solid tumors. *Annu Rev Biomed Eng* **1**, 241-263 (1999).
22. Chauhan, V.P., Stylianopoulos, T., Boucher, Y. & Jain, R.K. Delivery of Molecular and Nanoscale Medicine to Tumors: Transport Barriers and Strategies. *Annual Review of Chemical and Biomolecular Engineering* **2**, 281-298 (2011).
23. Loomis, K., McNeeley, K. & Bellamkonda, R.V. Nanoparticles with targeting, triggered release, and imaging functionality for cancer applications. *Soft Matter* **7**, (2011).
24. Park, J.W. *et al.* Anti-HER2 Immunoliposomes . *Clinical Cancer Research* **8** , 1172-1181 (2002).
25. Lopes de Menezes, D.E., Pilarski, L.M. & Allen, T.M. In Vitro and in Vivo Targeting of Immunoliposomal Doxorubicin to Human B-Cell Lymphoma. *Cancer Res.* **58**, 3320-3330 (1998).
26. Abou-Jawde, R., Choueiri, T., Alemany, C. & Mekhail, T. An overview of targeted treatments in cancer. *Clinical Therapeutics* **25**, 2121-2137 (2003).
27. Slamon, D. *et al.* Studies of the HER-2/neu proto-oncogene in human breast and ovarian cancer. *Science* **244**, 707-712 (1989).

28. Nielsen, U.B. *et al.* Therapeutic efficacy of anti-ErbB2 immunoliposomes targeted by a phage antibody selected for cellular endocytosis. *Biochimica et Biophysica Acta (BBA) - Molecular Cell Research* **1591**, 109-118 (2002).
29. Antony, A.C. The biological chemistry of folate receptors. *Blood* **79**, 2807-20 (1992).
30. Pan, X.Q., Wang, H. & Lee, R.J. *Antitumor Activity of Folate Receptor-Targeted Liposomal Doxorubicin in a KB Oral Carcinoma Murine Xenograft Model.* *Pharmaceutical Research* **20**, 417-422 (Springer Netherlands: 2003).
31. Nielsen, T.O. *et al.* Immunohistochemical and clinical characterization of the basal-like subtype of invasive breast carcinoma. *Clinical cancer research : an official journal of the American Association for Cancer Research* **10**, 5367-74 (2004).
32. Klibanov, A.L. Targeted delivery of gas-filled microspheres, contrast agents for ultrasound imaging. *Adv Drug Deliv Rev* **37**, 139-157 (1999).
33. Green, N.M. AVIDIN. 1. The use of (14-C)Biotin for Kinetic Studies and for Assay. *The Biochemical journal* **89**, 585-91 (1963).
34. Cho, Y.W., Lee, J., Lee, S.C., Huh, K.M. & Park, K. Hydrotropic agents for study of in vitro paclitaxel release from polymeric micelles. *Journal of controlled release : official journal of the Controlled Release Society* **97**, 249-57 (2004).
35. Harries, M., Ellis, P. & Harper, P. Nanoparticle albumin-bound paclitaxel for metastatic breast cancer. *Journal of clinical oncology : official journal of the American Society of Clinical Oncology* **23**, 7768-71 (2005).

## Chapter 8: Conclusions and Future Work

### 8.1 MOTIVATION

Cancer is the second leading cause of death in the United States and affects one-half of all men and one-third of all women in their lifetimes<sup>1</sup>. Due to effective therapies such as surgery, chemotherapeutics, and radiation, it has been shown that early detection of cancer dramatically increases survival rates<sup>1</sup>. The main method of early cancer detection is through the use of medical imaging modalities, and recent advances have allowed for super high resolution and high contrast images, some with functional capabilities, but no imaging modality is without limitations. Some of the most common clinically employed imaging modalities, including computed tomography (CT), X-ray imaging, nuclear imaging, and magnetic resonance imaging (MRI), expose patients to ionizing radiation, and have high costs to purchase and operate which limit their general availability to large hospitals<sup>2</sup>. Recently, combined ultrasound and photoacoustic imaging has emerged as a possible solution to the invasive and expensive problems associated with other imaging modalities<sup>3-8</sup>. Combined ultrasound and photoacoustic imaging can be used to provide morphological, functional, and molecular data with the same instrumentation<sup>9,10</sup> all while being biologically noninvasive, real-time, and cost effective. Combined ultrasound and photoacoustic imaging can provide morphological and functional data solely from the intrinsic acoustic and optical contrasts within the body, but it can also be adapted to use nanoparticle contrast agents, providing significantly higher contrast and added molecular imaging functionality. The difficulty of developing a single contrast agent for ultrasound and photoacoustic imaging modalities lies with the fact that they use two different contrast mechanisms (acoustic impedance and optical absorption, respectively). Therefore, prior to the beginning of this

dissertation, no single contrast agent had been developed that could be used simultaneously for this powerful imaging combination.

The overarching goal of this work was to design, synthesize, characterize, and test a nano-scale, dual contrast agent that worked simultaneously for combined ultrasound and photoacoustic imaging. Beyond contrast enhancing abilities, the adaptation of said contrast agent for targeted and therapeutic applications was explored. Towards that end, a contrast agent was developed that combined a miniaturized version of perfluorocarbon particles for ultrasound contrast with plasmonic, noble metal nanoparticles traditionally used to enhance optical imaging modalities to produce a signal contrast agent. This contrast agent, entitled Photoacoustic nanoDroplets (PAnDs), is novel and has been patented<sup>11,12</sup>. This work encompassed the development from bench-top design to *in vivo* animal testing, with the goals of showing feasibility for clinical research. More specifically, Chapter 2 introduced the design process for development of PAnDs, their general synthesis and characterization methods, and a few alternative synthesis strategies that could be used when slightly different outcomes are desired. Chapters 3 and 4 focused on the testing and optimization of PAnDs for dual contrast enhancement, and understanding the physics and functionality of PAnDs. After characterization and optimization of PAnDs, *in vivo* experiments were discussed in Chapter 5. Chapters 6 and 7 focused on how PAnDs passively and actively interact with cells and how PAnDs can be altered to become molecularly specific drug delivery agents as well as dual contrast agents. Overall, PAnDs have the potential to be used for a multitude of purposes and applications due to their flexibility and adaptability for diagnostic and therapeutic applications. Here, a critical overview of the conclusions provided through experimentation with PAnDs will be presented, as well as discussion concerning the

future directions that PAnD research could take. Finally, a statement of contributions to the field of this thesis work is provided.

## **8.2 SUMMARY OF CONCLUSIONS**

The following sections detail the conclusions and any potential future work that might be done based on the experiments described throughout this thesis.

### **8.2.1 Photoacoustic nanoDroplet Synthesis and Characterization**

PAnDs were synthesized via a facile “oil-in-water” emulsion technique that produces naturally nano-sized, albumin coated droplets of perfluorocarbon in which specially capped gold nanorods (described in Section 2.5.1) are suspended. To create a more homogenous size distribution, the PAnDs are pushed through polycarbonate membranes with a lipid mini-extruder. Analysis and characterization through UV-visible spectrophotometry, transmission electron microscopy, dynamic light scattering, and stability studies verify that PAnDs can be synthesized with highly repeatable properties. Furthermore, PAnDs maintain their stability under refrigeration at 2-8 °C, and after being heated up to 50 °C. During characterization, it was noticed that initial size before passing through the mini-extruder corresponded to the concentration of BSA used in the procedure. The methods described use BSA as the limiting constituent so that nano size particles can be synthesized. Throughout the project, cryotransmission electron microscopy (cTEM) was used for all high resolution images of PAnDs in their natural state. However, cTEM is a very temperamental imaging method and currently not available and The University of Texas at Austin campus (images acquired in this study were taken at Texas A&M University and Rice University). To routinely characterize PAnD particles standard TEM of dried or glutaraldehyde fixed samples was sufficient in terms of nanorod location, minimal droplet size, and loading efficiency. Overall, the

synthesis method provided a simple way to create a dual contrast agent for combined photoacoustic and ultrasound imaging that is highly adaptable to specific applications in terms of particle size, the number of nanoparticles encapsulated, the extent of nanoparticle loading, and the addition of surface coatings.

### **8.2.2 Cellular Interactions and Cytotoxicity**

The studies completed in this thesis show that PAnDs have no cytotoxic effects after simple incubation with cells for 30 hours. This is not surprising, considering that PAnDs use materials that are FDA approved for use in correlation with other drugs (albumin and perfluorocarbons) and materials that are currently undergoing rigorous cytotoxicity trials (gold nanoparticles) that seem to be indicating that they are bioinert. The hydrocarbon coated or fluorinated gold nanorods have had the majority of the initial synthesis ligand, CTAB (known to be cytotoxic), removed from the surface. There is some question about the toxicity of organically coated gold nanorods expelled from the droplets. These question could be investigated using further animal studies, but current data suggest that gold is simply retained in the liver and spleen or excreted in the feces with limited, if any, long term effects<sup>13</sup>. While these studies can only be broadly generalized with regards to the clinical application of PAnDs, initial studies suggest limited chemical cytotoxicity.

Passive interaction between PAnDs and cells show only neutral effects, although the active interaction between vaporization PAnDs and cells is another matter. The active interaction studies show no harmful effects on cells, but rather the potential for increased cell activity or viability. While extensive discussion about why these effects occur was provided in Section 6.3.3, a general summary indicates that negative, destructive effects are likely not occurring, but there is still some uncertainty whether the vaporization of

PAnDs near cells may actually induce positive effects. However, if PAnDs are shown to produce increases in cell viability, they could be used in healing therapeutic applications, such as muscle, nerve, and bone regrowth or in combination with stem cell therapy.

### **8.2.3 PAnD Functionality and Physical Responses**

Through various phantom and *in vivo* experiments, the methods in which PAnDs enhance contrast in both ultrasound and photoacoustic imaging were determined. PAnDs function through a total of three contrast enhancing mechanisms, including vaporization and thermal expansion for photoacoustic imaging and increased acoustic impedance mismatch for ultrasound imaging. Pulsed laser irradiation is absorbed by the encapsulated gold nanorods and released to the surrounding fluid as heat, which causes localized thermal expansion around the nanoparticle. This high pressure frequency, as determined by comparing the effects of continuous versus pulsed laser irradiation wave in Section 4.5.2, vaporizes the nano-sized perfluorocarbon droplet into a gaseous bubble. This vaporization produces a single occurrence shock wave that can be interpreted by ultrasound transducers as a large photoacoustic transient. The second, and long term photoacoustic signal is generated by the continued pulsed laser irradiation, absorption, and subsequent thermal expansion experienced by the gold nanorods. Finally, the resulting gaseous phase (shown in Figs, 3.2, 3.3, 3.5, 3.8, and 4.6) increases the acoustic mismatch causing greater pressure wave reflectance and higher contrast ultrasound images.

### **8.2.4 Contrast Enhancing Abilities of PAnDs**

The phantom studies performed showed an average photoacoustic contrast approximately one order of magnitude higher than that of the gold nanorods loading inside the PAnDs on their own, with a high of two orders of magnitude of signal increase.

Ultrasound contrast exceeds 20 dB in some experiments depending on the experimental conditions such as PAnD concentration and size. However, while the mechanisms of function and contrast enhancing abilities are demonstrated in this work, there is a realization that the full potential for using vaporization of PAnDs for signal generation might not have been met. In this work, the maximum signal gain between vaporization and thermal expansion signal was slightly under two orders of magnitude. Theoretically, vaporization should emit acoustic transients four orders of magnitude higher than thermal expansion. Therefore, further optimization of PAnDs may yield an even higher signal. Specifically, focusing on the nanoparticle loading would allow the nanorod signal to be minimized while still allowing for vaporization. Further, the use of equipment tuned to discern signals from vaporization from those caused by thermal expansion could optimize the use of PAnDs.

While phantom studies showed great promise for the use of PAnDs, some challenges were encountered during the tissue studies. The highly optically absorbing and scattering environment that exists within tissues increased the background noise for imaging of PAnDs. This noise is inclusive of the endogenous absorbers found in tissues and decreases the difference between the signal from vaporization and thermal expansion. This phenomenon is relatively unavoidable unless imaging with laser wavelengths that minimize background signal from tissue, such as 1064 nm. Furthermore, because light in the tissue becomes diffuse, not all of the accumulated PAnDs vaporize at the same time point, decreasing the initial signal, but simultaneously prolonging an increased signal. This effect can be seen in the graph in Fig 5.2, which represents imaging in tissue as compared to the graph in Fig. 3.4 which represents imaging done in a phantom. In spite of this issue, the signals collected in tissue were still sufficiently large that they could be distinguished from the background signal level caused by endogenous contrast. In

addition, the characteristic decay curve of the photoacoustic signal produced by PAnDs was observed, indicating PAnDs would be suitable for *in vivo* applications. However, when attempting image via vasculature accumulation in a mouse model, no increase in signal was seen. While these results were disappointing, it was no doubt due to the challenge of completing a successful tail-vein injection of the animal subject. This hypothesis was verified after gas accumulation was observed in the areas of the tail where the injections took place, representing vaporization of localized aggregates of PAnDs. Possible alternatives to tail vein injection include using intraocular injection<sup>14</sup> or using a larger animal model, such as rat. A rat model would provide the additional benefit of imaging at greater depth at the same time. There is extensive literature showing that particles similar to PAnDs can circulate and accumulate efficiently<sup>15-20</sup>. Therefore, future studies should focus on *in vivo* vascular circulation and accumulation of PAnDs.

### **8.2.5 Therapeutic and Molecular Modifications of PAnDs**

Two methods for attaching monoclonal antibodies (mAb) to the surface of PAnDs were described in section 7.2.1 and 7.2.2 and showed promising results for the targeted delivery of PAnDs to specific receptors of diseased cells. Incorporating biotin into the shell of the PAnDs and then attaching avidin to the targeting moieties proved to be a slightly better strategy as less aggregation in the samples occurred. Further studies will be needed to determine to what extent the mAb bind to PAnDs and the selectivity that can be obtained by using this targeting strategy. Furthermore, *in vivo* studies using positive and negative control tumor models should be used to test if targeting PAnDs will actually increase their accumulation within tumor tissues. Overall, these studies show promise for the ability of PAnDs to be targeting to specific molecular markers.

Beyond molecular targeting, PAnDs were also loading with a chemotherapeutic drug, Paclitaxel. Fluorescent studies and mass spectroscopy analysis showed high concentrations of Paclitaxel could be loaded into PAnDs. The drug delivery vector Abraxane® (albumin bound Paclitaxel) holds less than 5 mg/ml of drug, however PAnDs can easily be loaded with up to 20 mg/ml as shown by current experiments, and have the potential to be loaded even higher. Considering that PAnDs are vaporized upon applied pulsed laser irradiation, this would allow for optically triggered drug release only in the areas where imaging took place. This has the potential to reduce systemic cytotoxic effects of the drug and reduce unwanted side effects. When studying the passive release of the drug Paclitaxel from PAnDs, it was noted that a slow and linear drug release occurred due to cumulative release of contents from PAnDs instead of passive diffusion of drugs. This indicates that PAnD are likely to survive with a majority of their therapeutic cargo still encapsulated, allowing for release during optically triggered activation. These studies indicate that there is promise for using PAnDs as nano-size drug delivery vectors for treatments of cancers.

### **8.3 FUTURE DIRECTIONS FOR PANDS**

The immediate research directions, some discussed in the previous sections, also include continuing studies towards clinical translation. Initially, continuing animal studies to investigate PAnD pharmacokinetics and pharmacodynamics, accumulation properties in different types of tissues, and whether targeting moieties attached to the surface alter these properties need to be examined. Additionally, it has been demonstrated that PAnDs can contain large concentrations of organic drug compared to other drug delivery vectors. Therefore, research should be done to determine how treatment using

these particles differs from the traditional “gold standard” methods such as direct chemotherapy and radiation therapy.

PAnDs are not only useful for treatment of diseased tissues, but also in conjunction with ultrasound for healing of damaged tissues such a nerve, muscle, and bone. Therefore, the immediate research directions continue beyond the scope of this work towards a number of *in vivo* capabilities for clinical applications. The strong photoacoustic signal PAnDs produce with minimal light energy indicates that one of their primary uses could be for relatively deep imaging of tissues. A few of these applications include breast cancer, pancreatic cancer, and prostate cancer imaging. These organs are too deep to image using traditional optical modalities, as light delivery is prevented by the high tissue absorption and scattering. In the case of triple-negative breast cancer, PAnDs could be used clinically in the following way and as outlined in Fig 8.1. First, EGFR-targeted imaging Photoacoustic nanoDroplets (i-PAnDs) would be injected into a patient intravenously, and allowed to accumulate in the tumor region with molecular specificity conferred by the attached targeting moieties. Then, combined ultrasound and photoacoustic imaging would allow for localization and diagnosis of tumors with matching molecular profiles. Next, therapeutic EGFR-targeted Photoacoustic nanoDroplets (t-PAnDs) loaded with Paclitaxel, a drug commonly used to treat triple negative breast cancer, would be injected and allowed to accumulate in the tumor. Combined ultrasound and photoacoustics would be used to trigger the optically activated delivery of the encapsulated therapeutic cargo, the attached antibodies, while ultrasound would then be applied to stimulate the co-localized gas bubbles, thus inducing sonoporation and allowing for increased cellular uptake of the dual therapeutic agents. Treatment outcome would be monitored noninvasively via further use of EGFR-targeted i-PAnDs using combined ultrasound and photoacoustic imaging, negating the need for

invasive biopsies or surgeries. The monitoring would quantify important parameters in tumor malignancy, including: size and morphology, total hemoglobin content, oxygen saturation, and relative changes in molecular expressions.

Additional clinical applications of PAnDs would include liver and spleen imaging. Intravenously injected contrast agents will accumulate naturally in these organs as they are cleared from the circulatory system. Enhancing delivery using molecular-specific targeting could increase the accumulation within any diseased spots. Using PAnDs and a combination of photoacoustic imaging at 1064 nm<sup>10</sup> to reduce the background signal from blood, diseased liver and spleen tissue could be imaged. These are only a few examples of how PAnDs could be used for imaging of disease relatively deep within the body and combined with therapeutic treatment.

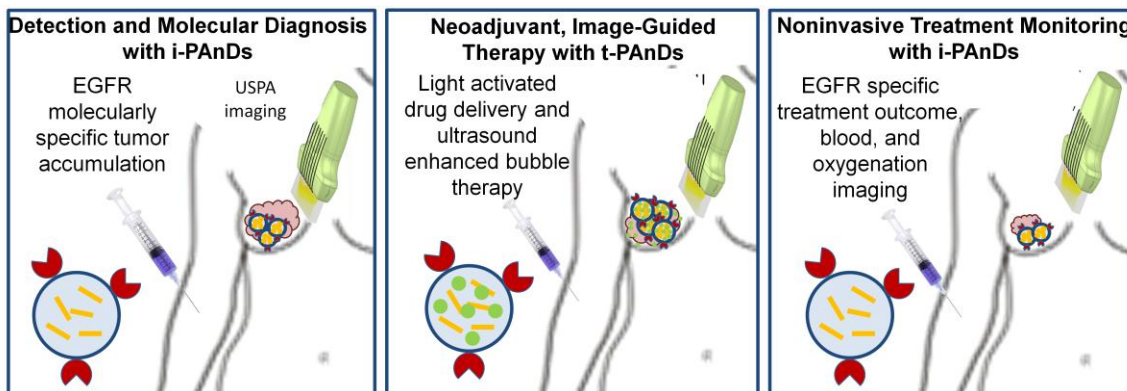


Figure 8.2: Diagram showing the proposed clinical use of PAnDs for treatment of triple-negative breast cancer through imaging diagnosis, imaged guided therapy, and treatment monitoring.

While most of the therapeutic applications of PAnDs discussed herein have focused on the treatment of cancers using a novel method of delivering chemotherapeutic drugs, PAnDs also have the potential to be used in additional treatment strategies. Transfection of cells with si-RNA using droplets and bubbles has also recently been

studied<sup>21-23</sup>. The vaporization and then stimulation via ultrasound of gas bubbles using sonoporation, cavitation, or acoustic streaming mediate gene-silencing therapies by increasing the intracellular uptake or delivery of si-RNAs. PAnDs could provide further assistance as their nano-size allows their extravasation into diseased tissues where si-RNA could be delivered to different types of cells, such as cancer stem cells, potentially limiting the growth of tumor malignancies. Another potential therapeutic application for PAnDs involves controlled, localized disruption of the blood brain barrier<sup>24</sup>, which is impermeable to all but the smallest metabolites by mechanisms similar to those listed for gene therapy delivery. Finally, PAnDs not only have the potential to destroy diseased cells, but also to repair damage to normal cells and tissues. The effects of ultrasound-induced cavitation have been demonstrated to accelerate the recovery of injured nerve, muscle, and bone tissues<sup>25-28</sup>. The potential therapeutic applications of PAnDs, combined with the demonstrated contrast enhanced imaging applications, make the applications of PAnDs numerous.

#### **8.4 SUMMARY OF CONTRIBUTIONS TO THE FIELD**

The originality and impact of this thesis work has been demonstrated by the design, synthesis, and development of a novel dual contrast agent for combined ultrasound and photoacoustic imaging. To that end, several strategies were developed that aided in the synthesis of PAnDs including: the process of fluorination of gold nanorods (Chapter 2), sizing of protein coated nano-scale perfluorocarbon droplets (Chapter 2), using cryoTEM to image intact protein coated, perfluorocarbon droplets (Chapter 2), development of phantom preparation methods (Chapter 3), altering ultrasound imaging methods to collect real-time ultrasound and photoacoustic using the WinProbe system (Chapter 4), altering imaging methods using the Vevo2100 to collect real-time

photoacoustic signals (Chapter 4), developing methods to monitor short and long term effects of vaporization on cells and membrane permeation (Chapter 6), developing methods for drug encapsulation (Chapter 7), developing a method to study the drug release characteristics of an organic drug into an aqueous environment (Chapter 7), and developing a method for incorporation of biotin and avidin into the shell of PANDs (Chapter 7). The aim of this dissertation was also meant to be instructional for any who may wish to continue this work, as it includes detailed instructions for synthesis and the experiments done here as well as discussion about areas that represent potential problems or pitfalls. While no specific applications for PANDs were focused on in this work, besides those discussed in the previous section, the flexibility and adaptability of PANDs makes them ideal for many imaging and therapeutic applications.

PANDs have made a major contribution to the field of photoacoustics beyond their role as a dual contrast agent for combined ultrasound and photoacoustic imaging. For the first time, vaporization has been employed as a signal generator for *in vivo* photoacoustic imaging. Furthermore, the methods used for imaging are non-destructive and convert light to acoustic transients with high efficiency. One of the biggest challenges facing optical imaging modalities is the penetration of light at depths sufficient for imaging. The use of PANDs provides a method by which photoacoustic imaging depth can be increased, making them suitable for use in human applications. Optical activation of PANDs also provides an advance to the ultrasound contrast field. Previously, inducing a phase change in nanoscale perfluorocarbon droplets required either high frequency or high intensity ultrasound, or the use of a perfluorocarbon that is superheated at room temperature. The effects of high frequency and high pressure ultrasound on tissues can be detrimental, and working with perfluorocarbons with low boiling points is extremely

difficult. These issues are successfully overcome by the light-triggered vaporization of PANDs.

Extensive further investigation is required to study PANDs and explore their potential uses for specific medical applications. The work described in this dissertation represents a significant step towards the development of a clinically functional, dual contrast agent for combined ultrasound and photoacoustic imaging that would image deeper with more sensitivity and specificity than existing techniques and offer improved outcomes for disease diagnostics and treatment.

## 8.5 REFERENCES

1. Hayat, M.J., Howlader, N., Reichman, M.E. & Edwards, B.K. Cancer Statistics, Trends, and Multiple Primary Cancer Analyses from the Surveillance, Epidemiology, and End Results (SEER) Program. *Oncologist* **12**, 20-37 (2007).
2. Hendee E. Russell, W.R.R. *Medical Imaging Physics*. 512 (Wiley-Liss, Inc.: New York, 2002).
3. Oraevsky, A.A., Jacques, S.L. & Tittel, F.K. Determination of tissue optical properties by time-resolved detection of laser-induced stress waves. *Proc. SPIE* **1882**, 86-101 (1993).
4. Oraevsky, A.A., Jacques, S.L., Esenaliev, R.O. & Tittel, F.K. Time-Resolved Optoacoustic Imaging in Layered Biological Tissues. *Advances in Optical Imaging and Photon Migration* **21**, 161-165 (1994).
5. Oraevsky, A.A., Esenaliev, R.O., Jacques, S.L., Thomsen, S.L. & Tittel, F.K. Lateral and z-axial resolution in laser optoacoustic imaging with ultrasonic transducers. *Proc. SPIE* **2389**, 198-208 (1995).
6. Oraevsky, A.A., Jacques, S.L. & Tittel, F.K. Measurement of tissue optical properties by time-resolved detection of laser-induced transient stress. *Appl Opt* **36**, 402-415 (1997).
7. Kruger, R.A. Photoacoustic ultrasound. *Med Phys* **21**, 127-131 (1994).
8. Kruger, R.A., Liu, P., Fang, Y.R. & Appledorn, C.R. Photoacoustic ultrasound (PAUS)--reconstruction tomography. *Med Phys* **22**, 1605-1609 (1995).
9. Mallidi, S., Larson, T., Aaron, J., Sokolov, K. & Emelianov, S. Molecular specific optoacoustic imaging with plasmonic nanoparticles. *Opt Express* **15**, 6583-6588 (2007).

10. Homan, K. *et al.* Prospects of molecular photoacoustic imaging at 1064 nm wavelength. *Opt. Lett.* **35**, 2663-2665 (2010).
11. Emelianov, S., Wilson, K. & Homan, K. Nanocarriers for Imaging and Therapy Applications. (2011).at  
<<http://www.wipo.int/patentscope/search/en/detail.jsf?docId=WO2011035279>>
12. Wilson, K., Homan, K. & Emelianov, S. Biomedical photoacoustics beyond thermal expansion using triggered nanodroplet vaporization for contrast-enhanced imaging. *Nature Communications* **3**, 618 (2012).
13. Lewinski, N., Colvin, V. & Drezek, R. Cytotoxicity of nanoparticles. *Small* **4**, 26-49 (2008).
14. Xie, W. *et al.* Ultrasound microbubbles enhance recombinant adeno-associated virus vector delivery to retinal ganglion cells *in vivo*. *Academic radiology* **17**, 1242-8 (2010).
15. Lavisse, S. *et al.* In vitro echogenicity characterization of poly[lactide-coglycolide] (plga) microparticles and preliminary *in vivo* ultrasound enhancement study for ultrasound contrast agent application. *Invest Radiol* **40**, 536-544 (2005).
16. Nishihara, M., Imai, K. & Yokoyama, M. Preparation of perfluorocarbon/fluoroalkyl polymer nanodroplets for cancer-targeted ultrasound contrast agents. *Chem. Lett.* **38**, 556-557 (2009).
17. Caskey, C.F., Stieger, S.M., Qin, S., Dayton, P.A. & Ferrara, K.W. Direct observations of ultrasound microbubble contrast agent interaction with the microvessel wall. *J. Acoust. Soc. Am.* **122**, 1191-1200 (2007).
18. Zhu, J.-an *et al.* Low-frequency and high-intensity ultrasonic may play a better role in Ultrasound Contrast Agent drug delivery system *in vivo*. *Med. Hypotheses* **73**, 211-212 (2009).
19. Li, T., Tachibana, K. & Kuroki, M. Gene transfer with echo-enhanced contrast agents: comparison between Alunex, Optison, and Levovist in mice--initial results. *Radiology* **229**, 423-428 (2003).
20. Wheatley, M.A., Forsberg, F., Oum, K., Ro, R. & El-Sherif, D. Comparison of in vitro and in vivo acoustic response of a novel 50:50 PLGA contrast agent. *Ultrasonics* **44**, 360-367 (2006).
21. Ferrara, K., Pollard, R. & Borden, M. Ultrasound microbubble contrast agents: fundamentals and application to gene and drug delivery. *Annu. Rev. Biomed. Eng.* **9**, 415-447 (2007).
22. Wells, D.J. Electroporation and ultrasound enhanced non-viral gene delivery in vitro and in vivo. *Cell Biol. Toxicol.* **26**, 21-28 (2010).

23. Unger, E.C., Hersh, E., Vannan, M. & McCreery, T. Gene delivery using ultrasound contrast agents. *Echocardiography* **18**, 355-361 (2001).
24. Chopra, R., Vykhodtseva, N. & Hynynen, K. Influence of Exposure Time and Pressure Amplitude on Blood-Brain-Barrier Opening Using Transcranial Ultrasound Exposures. *ACS Chem. Neurosci.* **1**, 391-398 (2010).
25. Hart, J. The use of ultrasound therapy in wound healing. *Journal of wound care* **7**, 25-8 (1998).
26. Mitragotri, S. Healing sound: the use of ultrasound in drug delivery and other therapeutic applications. *Nature reviews. Drug discovery* **4**, 255-60 (2005).
27. Hadjiargyrou, M., McLeod, K., Ryaby, J.P. & Rubin, C. Enhancement of Fracture Healing by Low Intensity Ultrasound. *Clinical Orthopaedics and Related Research* **355**, (1998).
28. Cook, S.D. *et al.* Improved Cartilage Repair After Treatment With Low-Intensity Pulsed Ultrasound. *Clinical Orthopaedics and Related Research* **391**, (2001).

## References

- ANSI. "Orlando: Laser Institute of America ." *American National Standard for Safe use of Lasers, ANSI Z136.1* (2000): n. pag. Print.
- Abou-Jawde, Rony et al. "An overview of targeted treatments in cancer." *Clinical Therapeutics* 25.8 (2003): 2121-2137. Web. 10 Dec. 2011.
- Agarwal, A et al. "Targeted gold nanorod contrast agent for prostate cancer detection by photoacoustic imaging." *Journal of Applied Physics* 102 (2007): 64701. Print.
- Ai-Ho, Liao et al. "Targeted multimodality contrast agent: Synthesis and applications of <sup>18</sup>F-labeled targeted perfluorocarbon-filled albumin microbubbles for microUS and microPET." *2009 IEEE International Ultrasonics Symposium*. IEEE, 2009. 1274-1277. Web. 3 Mar. 2012.
- Akers, Walter J et al. "Noninvasive Photoacoustic and Fluorescence Sentinel Lymph Node Identification using Dye-Loaded Perfluorocarbon Nanoparticles." *ACS Nano* 5. Copyright (C) 2011 American Chemical Society (ACS). All Rights Reserved. (2011): 173-182.
- Antony, A C. "The biological chemistry of folate receptors." *Blood* 79.11 (1992): 2807-20. Web. 26 Feb. 2012.
- Asshauer, T., K. Rink, and G. Delacrétaz. "Acoustic transient generation by holmium-laser-induced cavitation bubbles." *Journal of Applied Physics* 76.9 (1994): 5007. Web. 16 Jan. 2012.
- Atlanta: American Cancer Society, Inc. *Breast Cancer Facts & Figures 2011-2012*. Print.
- Aussel, J D, A Le Brun, and J C Baboux. "Generating acoustic waves by laser: theoretical and experimental study of the emission source." *Ultrasonics* 26.5 (1988): 245-255.
- Azouz, S M et al. "Prevention of local tumor growth with paclitaxel-loaded microspheres." *J Thorac Cardiovasc Surg* 135.5 (2008): 1014-1021.
- Bekeredjian, Raffi, Paul A Grayburn, and Ralph V Shohet. "Use of ultrasound contrast agents for gene or drug delivery in cardiovascular medicine." *Journal of the American College of Cardiology* 45.3 (2005): 329-335.
- Bell, Alexander Graham. "Production of sound by radiant energy." *Journal of Franklin Institute* 111.6 (1881): 401-426. Print.
- Bergen, J M et al. "Gold nanoparticles as a versatile platform for optimizing physicochemical parameters for targeted drug delivery." *Macromol Biosci* 6.7 (2006): 506-516.

- Borden, Mark A et al. "Influence of lipid shell physicochemical properties on ultrasound-induced microbubble destruction." *IEEE transactions on ultrasonics, ferroelectrics, and frequency control* 52.11 (2005): 1992-2002. Web. 5 Jan. 2012.
- Bowen, T. "Radiation-Induced Thermoacoustic Soft Tissue Imaging." *1981 Ultrasonics Symposium*. 1981. 817-822. Print.
- Brigger, I, C Dubernet, and P Couvreur. "Nanoparticles in cancer therapy and diagnosis." *Adv Drug Deliv Rev* 54.5 (2002): 631-651.
- Brown, Dennis M. *Drug delivery systems in cancer therapy*. Totowa, N.J.: Humana Press, 2004.
- Cailleau, Relda, Matilde Olivé, and Quita V. J. Cruciger. "Long-term human breast carcinoma cell lines of metastatic origin: Preliminary characterization." *In Vitro* 14.11 (1978): 911-915. Web. 11 Feb. 2012.
- Campbell, Robert B. "Tumor Physiology and Delivery of Nanopharmaceuticals." *Anti-Cancer Agents in Medicinal Chemistry (Formerly Current Medicinal Chemistry* 6.6 (2006): 10. Web. 1 Jan. 2012.
- Caruthers, Shelton D et al. "Anti-angiogenic perfluorocarbon nanoparticles for diagnosis and treatment of atherosclerosis." *Wiley Interdiscip. Rev.: Nanomed. Nanobiotechnol.* 1. Copyright (C) 2011 American Chemical Society (ACS). All Rights Reserved. (2009): 311-323.
- Caskey, Charles F et al. "Direct observations of ultrasound microbubble contrast agent interaction with the microvessel wall." *J. Acoust. Soc. Am.* 122. Copyright (C) 2011 American Chemical Society (ACS). All Rights Reserved. (2007): 1191-1200.
- Castelli, Francesco et al. "Characterization of Lipophilic Gemcitabine Prodrug-Liposomal Membrane Interaction by Differential Scanning Calorimetry." *Mol. Pharm. FIELD Full Journal Title: Molecular Pharmaceutics* 3.6 (2006): 737-744. Print.
- Charlier, N et al. "Nano-emulsions of fluorinated trityl radicals as sensors for EPR oximetry." *Journal of magnetic resonance (San Diego, Calif. : 1997)* 197.2 (2009): 176-80. Web. 3 Mar. 2012.
- Chauhan, Vikash P et al. "Delivery of Molecular and Nanoscale Medicine to Tumors: Transport Barriers and Strategies." *Annual Review of Chemical and Biomolecular Engineering* 2.1 (2011): 281-298.
- Chen, Di, and Junru Wu. "An in vitro feasibility study of controlled drug release from encapsulated nanometer liposomes using high intensity focused ultrasound." *Ultrasonics* 50. Copyright (C) 2011 American Chemical Society (ACS). All Rights Reserved. (2010): 744-749.
- Chen, Huxiong, and Gerald Diebold. "Chemical generation of acoustic waves: a giant photoacoustic effect." *Science* v270.n5238 (1995): p963(4).

- Chen, Yun-Sheng et al. "Enhanced thermal stability of silica-coated gold nanorods for photoacoustic imaging and image-guided therapy." *Opt. Express* 18.9 (2010): 8867-8878.
- Cho, K, X Wang, et al. "Therapeutic nanoparticles for drug delivery in cancer." *Clin Cancer Res* 14.5 (2008): 1310-1316.
- Cho, Yong Woo, Jaehwi Lee, et al. "Hydrotropic agents for study of in vitro paclitaxel release from polymeric micelles." *Journal of controlled release : official journal of the Controlled Release Society* 97.2 (2004): 249-57. Web. 27 Mar. 2012.
- Chopra, Rajiv, Natalia Vykhodtseva, and Kullervo Hynynen. "Influence of Exposure Time and Pressure Amplitude on Blood-Brain-Barrier Opening Using Transcranial Ultrasound Exposures." *ACS Chem. Neurosci.* 1. Copyright (C) 2011 American Chemical Society (ACS). All Rights Reserved. (2010): 391-398.
- Christensen, Douglas A. *Ultrasonic Bioinstrumentation*. New York: John Wiley & Sons, Inc., 1988. Print.
- Chumakova, O V et al. "Effect of 5-fluorouracil, Optison and ultrasound on MCF-7 cell viability." *Ultrasound Med Biol* 32.5 (2006): 751-758.
- Cleator, Susan, Wolfgang Heller, and R Charles Coombes. "Triple-negative breast cancer: therapeutic options." *The lancet oncology* 8.3 (2007): 235-44. Web. 17 Sept. 2011.
- Cook, Jason R, Richard R Bouchard, and Stanislav Y Emelianov. "Tissue-mimicking phantoms for photoacoustic and ultrasonic imaging." *Biomedical optics express* 2.11 (2011): 3193-206. Web. 6 Jan. 2012.
- Cook, Stephen D et al. "Improved Cartilage Repair After Treatment With Low-Intensity Pulsed Ultrasound." *Clinical Orthopaedics and Related Research* 391 (2001): n. pag.
- Copland, J A et al. "Bioconjugated gold nanoparticles as a molecular based contrast agent: implications for imaging of deep tumors using photoacoustic tomography." *Mol Imaging Biol* 6.5 (2004): 341-349.
- Coromili, V., and T. M. S. Chang. "Polydisperse Dextran as a Diffusing Test Solute to Study the Membrane Permeability of Alginate Polylysine Microcapsules." (2009): n. pag. Web. 27 Feb. 2012.
- Correas, J M, and S D Quay. "EchoGen emulsion: a new ultrasound contrast agent based on phase shift colloids." *Clinical radiology* 51 Suppl 1 (1996): 11-14.
- Cosgrove, D. "Ultrasound contrast agents: an overview." *Eur J Radiol* 60.3 (2006): 324-330.

- Couture, Olivier et al. "A model for reflectivity enhancement due to surface bound submicrometer particles." *Ultrasound in Medicine & Biology* 32.8 (2006): 1247-1255.
- Crowder, Kathryn C et al. "Sonic activation of molecularly-targeted nanoparticles accelerates transmembrane lipid delivery to cancer cells through contact-mediated mechanisms: implications for enhanced local drug delivery." *Ultrasound Med Biol* 31. Copyright (C) 2011 U.S. National Library of Medicine. (2005): 1693-1700. Print.
- Cui, W et al. "Preparation and evaluation of poly(L-lactide-co-glycolide) (PLGA) microbubbles as a contrast agent for myocardial contrast echocardiography." *J Biomed Mater Res B Appl Biomater* 73.1 (2005): 171-178.
- Danhier, F et al. "Paclitaxel-loaded PEGylated PLGA-based nanoparticles: in vitro and in vivo evaluation." *J Control Release* 133.1 (2009): 11-17.
- Dayton, Paul A et al. "Application of ultrasound to selectively localize nanodroplets for targeted imaging and therapy." *Mol Imaging* 5. Copyright (C) 2011 U.S. National Library of Medicine. (2006): 160-174. Print.
- Diaz-Lopez, Raquel, Nicolas Tsapis, and Elias Fattal. "Liquid Perfluorocarbons as Contrast Agents for Ultrasonography and 19F-MRI." *Pharm. Res.* 27. Copyright (C) 2011 American Chemical Society (ACS). All Rights Reserved. (2010): 1-16.
- Dijkmans, P A et al. "Microbubbles and ultrasound: from diagnosis to therapy." *European Journal of Echocardiography* 5.4 (2004): 245-246.
- Doan, N et al. "In vitro effects of therapeutic ultrasound on cell proliferation, protein synthesis, and cytokine production by human fibroblasts, osteoblasts, and monocytes." *Journal of oral and maxillofacial surgery : official journal of the American Association of Oral and Maxillofacial Surgeons* 57.4 (1999): 409-19; discussion 420. Web. 12 Feb. 2012.
- Dolan, Melda S et al. "Safety and Efficacy of Commercially Available Ultrasound Contrast Agents for Rest and Stress Echocardiography: A Multicenter Experience." *Journal of the American College of Cardiology* 53.1 (2009): 32-38.
- Duncan, Ruth. "Polymer conjugates as anticancer nanomedicines." *Nat Rev Cancer* 6.9 (2006): 688-701.
- Eck, W et al. "PEGylated gold nanoparticles conjugated to monoclonal F19 antibodies as targeted labeling agents for human pancreatic carcinoma tissue." *ACS Nano* 2.11 (2008): 2263-2272.
- Eghtedari, M A, J A Copland, et al. "Bioconjugated gold nanoparticles as a contrast agent for optoacoustic detection of small tumors." *Biomedical Optoacoustics Iv*. Ed. A A Oraevsky. Vol. 4960. Bellingham: Spie-Int Soc Optical Engineering, 2003. 76-85.

- Eghtedari, M, A V Liopo, J A Copland, et al. "Engineering of Hetero-Functional Gold Nanorods for the in vivo Molecular Targeting of Breast Cancer Cells." *Nano Lett* 9.1 (2009): 287-291. Print.
- Eghtedari, M et al. "Functionalized gold nanorods for molecular optoacoustic imaging - art. no. 64370G." Ed. A A Oraevsky & L V Wang. *Photons Plus Ultrasound: Imaging and Sensing 2007* 2007 : G4370-G4370.
- Eghtedari, M, A Oraevsky, et al. "High sensitivity of in vivo detection of gold nanorods using a laser optoacoustic imaging system." *Nano Lett* 7.7 (2007): 1914-1918.
- Eisenbrey, J R et al. "Development and optimization of a doxorubicin loaded poly(lactic acid) contrast agent for ultrasound directed drug delivery." *J. Controlled Release* 143. Copyright (C) 2011 American Chemical Society (ACS). All Rights Reserved. (2010): 38-44.
- El-Sherif, D M, and M A Wheatley. "Development of a novel method for synthesis of a polymeric ultrasound contrast agent." *J Biomed Mater Res A* 66.2 (2003): 347-355.
- Emelianov, S Y et al. "Combined ultrasound, optoacoustic, and elasticity imaging." *Proceedings of the SPIE Photonics West* 5320 (2004): 101-112. Print.
- Emelianov, Stanislav, Katheryne Wilson, and Kimberly Homan. "Nanocarriers for Imaging and Therapy Applications." 24 Mar. 2011. Web. 10 Jan. 2012.
- Escoffre, J M et al. "Doxorubicin Delivery into Tumor Cells with Ultrasound and Microbubbles." *Mol. Pharmaceutics* 8. Copyright (C) 2011 American Chemical Society (ACS). All Rights Reserved. (2011): 799-806.
- Esenaliev, Rinat O. "Radiation and nanoparticles for enhancement of drug delivery in solid tumors." Ed. USPTO. *USPTO* 2000 : 25.
- Eustis, Susie, and Mostafa A El-Sayed. "Why gold nanoparticles are more precious than pretty gold: Noble metal surface plasmon resonance and its enhancement of the radiative and nonradiative properties of nanocrystals of different shapes." *Chemical Society Reviews* 35.3 (2006): 209-217.
- Fay, B, K Brendel, and G Ludwig. "Studies of inhomogeneous substances by ultrasonic back-scattering." *Ultrasound in medicine & biology* 2.3 (1976): 195-8. Web. 6 Jan. 2012.
- Ferrante, E A et al. "Dual targeting improves microbubble contrast agent adhesion to VCAM-1 and P-selectin under flow." *J. Controlled Release* 140. Copyright (C) 2011 American Chemical Society (ACS). All Rights Reserved. (2009): 100-107.
- Ferrara, Katherine, Rachel Pollard, and Mark Borden. "Ultrasound microbubble contrast agents: fundamentals and application to gene and drug delivery." *Annu. Rev. Biomed. Eng.* 9. Copyright (C) 2011 American Chemical Society (ACS). All Rights Reserved. (2007): 415-447.

- Flaim, Stephen F. "Pharmacokinetics and Side Effects of Perfluorocarbon-Based Blood Substitutes." *Artificial Cells, Blood Substitutes and Biotechnology* 22.4 (1994): 1043-1054.
- Frenkel, V. "Ultrasound mediated delivery of drugs and genes to solid tumors." *Adv Drug Deliv Rev* 60.10 (2008): 1193-1208.
- Funk, Dorothee, Hans-Hermann Schrenk, and Eva Frei. "Serum albumin leads to false-positive results in the XTT and the MTT assay." *BioTechniques* 43.2 (2007): 178, 180, 182 passim. Web. 6 Mar. 2012.
- Galanzha, E I et al. "In vivo fiber-based multicolor photoacoustic detection and photothermal purging of metastasis in sentinel lymph nodes targeted by nanoparticles." *Journal of Biophotonics* 2.8-9 (2009): 528-539.
- Gao, P, B D Rush, et al. "Development of a supersaturable SEDDS (S-SEDDS) formulation of paclitaxel with improved oral bioavailability." *J Pharm Sci* 92.12 (2003): 2386-2398.
- Gao, Z et al. "Drug-loaded nano/microbubbles for combining ultrasonography and targeted chemotherapy." *Ultrasonics* (2007): n. pag.
- Gao, Zhonggao, Anne M Kennedy, Douglas A Christensen, et al. "Drug-loaded nano/microbubbles for combining ultrasonography and targeted chemotherapy." *Ultrasonics* 48. Copyright (C) 2011 American Chemical Society (ACS). All Rights Reserved. (2008): 260-270.
- Gobin, A M et al. "Near-infrared resonant nanoshells for combined optical imaging and photothermal cancer therapy." *Nano Lett* 7.7 (2007): 1929-1934.
- Goel, R et al. "Biodistribution of TNF-alpha-coated gold nanoparticles in an in vivo Model System." *Nanomedicine* 4.4 (2009): 401-410.
- Green, N M. "AVIDIN. 1. The use of (14-C)Biotin for Kinetic Studies and for Assay." *The Biochemical journal* 89.3 (1963): 585-91. Web. 30 Mar. 2012.
- Hadjigargyrou, Michael et al. "Enhancement of Fracture Healing by Low Intensity Ultrasound." *Clinical Orthopaedics and Related Research* 355 (1998): n. pag.
- Hall, T.J. et al. "Phantom materials for elastography." *IEEE Transactions on Ultrasonics, Ferroelectrics and Frequency Control* 44.6 (1997): 1355-1365. Web. 6 Jan. 2012.
- Harries, Mark, Paul Ellis, and Peter Harper. "Nanoparticle albumin-bound paclitaxel for metastatic breast cancer." *Journal of clinical oncology : official journal of the American Society of Clinical Oncology* 23.31 (2005): 7768-71. Web. 12 Feb. 2012.
- Hart, J. "The use of ultrasound therapy in wound healing." *Journal of wound care* 7.1 (1998): 25-8. Web. 12 Feb. 2012.

- Hayat, Matthew J et al. "Cancer Statistics, Trends, and Multiple Primary Cancer Analyses from the Surveillance, Epidemiology, and End Results (SEER) Program." *Oncologist* 12.1 (2007): 20-37.
- He, L, G L Wang, and Q Zhang. "An alternative paclitaxel microemulsion formulation: hypersensitivity evaluation and pharmacokinetic profile." *Int J Pharm* 250.1 (2003): 45-50.
- Hendee E. Russell, William R Ritenour. *Medical Imaging Physics*. 4th ed. New York: Wiley\_Liss, Inc., 2002. Print.
- Hobbs, Susan K et al. "Regulation of transport pathways in tumor vessels: Role of tumor type and microenvironment." *Proceedings of the National Academy of Sciences* 95.8 (1998): 4607-4612.
- Homan, K, J Shah, et al. "Combined ultrasound and photoacoustic imaging of pancreatic cancer using nanocage contrast agents." *SPIE Photonics West*. Vol. 7177. San Jose, CA, USA: Proceedings of the SPIE, 2009. 71771M. Print.
- Homan, Kimberly, Seungsoo Kim, et al. "Prospects of molecular photoacoustic imaging at 1064 nm wavelength." *Opt. Lett.* 35.15 (2010): 2663-2665.
- Immordino, M L et al. "Preparation, characterization, cytotoxicity and pharmacokinetics of liposomes containing lipophilic gemcitabine prodrugs." *J Control Release* 100.3 (2004): 331-346.
- Jain, R K. "Transport of molecules, particles, and cells in solid tumors." *Annu Rev Biomed Eng* 1 (1999): 241-263.
- Jennings, T, and G Strouse. "Past, present, and future of gold nanoparticles." *Adv Exp Med Biol* 620 (2007): 34-47.
- Johnson, Allan G. et al. "Method and apparatus for delivery of agents across the blood brain barrier." 22 Oct. 2009. Web. 3 Mar. 2012.
- Joshi, Pratixa et al. "Molecular Therapeutic Agents for Noninvasive Photoacoustic Image-guided Photothermal Therapy." *31st Annual International IEEE The Engineering in Medicine and Biology Conference (EMBC) Proceedings* 1158 (2009): n. pag. Print.
- Kuang Tzu, Huang, Chen Yen Hao, and Ameae M. Walker. "Inaccuracies in MTS assays: major distorting effects of medium, serum albumin, and fatty acids." *BioTechniques* 37.3 406-412. Web. 6 Mar. 2012.
- Kaneda, Megan M et al. "Perfluorocarbon nanoemulsions for quantitative molecular imaging and targeted therapeutics." *Ann Biomed Eng* 37. Copyright (C) 2011 U.S. National Library of Medicine. (2009): 1922-1933. Print.

- Kawabata, Kenichi et al. "Acoustic response of microbubbles derived from phase-change nanodroplet." *Jpn. J. Appl. Phys.* 49. Copyright (C) 2011 American Chemical Society (ACS). All Rights Reserved. (2010): 07HF18/1-07HF18/9.
- Keller, M W, W Glasheen, and S Kaul. "Albunex: a safe and effective commercially produced agent for myocardial contrast echocardiography." *Journal of the American Society of Echocardiography : official publication of the American Society of Echocardiography* 2.1 48-52. Web. 3 Mar. 2012.
- Kharine, Alexei et al. "Poly(vinyl alcohol) gels for use as tissue phantoms in photoacoustic mammography." *Physics in Medicine and Biology* 48.3 (2003): 357-370. Web. 6 Jan. 2012.
- Kiessling, F, J Huppert, and M Palmowski. "Functional and molecular ultrasound imaging: concepts and contrast agents." *Curr. Med. Chem.* 16. Copyright (C) 2011 American Chemical Society (ACS). All Rights Reserved. (2009): 627-642.
- Kim, Dongsik, and Costas P Grigoropoulos. "Phase-change phenomena and acoustic transient generation in the pulsed laser induced ablation of absorbing liquids." *Applied Surface Science* 127-129.0 (1998): 53-58.
- Klibanov, A L. "Targeted delivery of gas-filled microspheres, contrast agents for ultrasound imaging." *Adv Drug Deliv Rev* 37.1-3 (1999): 139-157.
- Korpanty, G et al. "Targeting vascular endothelium with avidin microbubbles." *Ultrasound Med Biol* 31.9 (2005): 1279-1283.
- Kou, X et al. "One-step synthesis of large-aspect-ratio single-crystalline gold nanorods by using CTPAB and CTBAB surfactants." *Chemistry* 13.10 (2007): 2929-2936.
- Kripfgans, O D et al. "Acoustic droplet vaporization for therapeutic and diagnostic applications." *Ultrasound Med Biol* 26.7 (2000): 1177-1189.
- Kruger, R A. "Photoacoustic ultrasound." *Med Phys* 21.1 (1994): 127-131.
- Kruger, R A et al. "Photoacoustic ultrasound (PAUS)--reconstruction tomography." *Med Phys* 22.10 (1995): 1605-1609.
- Ku, G, and L H V Wang. "Deeply penetrating photoacoustic tomography in biological tissues enhanced with an optical contrast agent." *Optics Letters* 30.5 (2005): 507-509.
- Kumar, A et al. "Phase transfer of silver nanoparticles from aqueous to organic solutions using fatty amine molecules." *J Colloid Interface Sci* 264.2 (2003): 396-401.
- Kumar, S, J Aaron, and K Sokolov. "Directional conjugation of antibodies to nanoparticles for synthesis of multiplexed optical contrast agents with both delivery and targeting moieties." *Nat Protoc* 3.2 (2008): 314-320.
- Kwon, S, and M A Wheatley. "Development and Characterization of PLA Nano-dispersion as a Potential Ultrasound Contrast Agent for Cancer Site Imaging."

- Proceedings of the IEEE, 31st Annual Northeast Bioengineering Conference* (2005): 144-145. Print.
- Landau, L D, and E M Lifshitz. *A Course in Theoretical Physics - Fluid Mechanics*. Vol. 6. Pergamon Press Ltd., 1987. Print.
- Lanza, G. M. “Targeted Antiproliferative Drug Delivery to Vascular Smooth Muscle Cells With a Magnetic Resonance Imaging Nanoparticle Contrast Agent: Implications for Rational Therapy of Restenosis.” *Circulation* 106.22 (2002): 2842-2847. Web. 12 July 2011.
- Lanza, Gregory M, Michael S Hughes, et al. “Acoustic molecular imaging and targeted drug delivery with perfluorocarbon nanoparticles.” *AIP Conf. Proc.* 754. Copyright (C) 2011 American Chemical Society (ACS). All Rights Reserved. (2005): 120-123. Print.
- Lanza, Gregory, Patrick M Winter, et al. “Targeted Perfluorocarbon Nanoparticles for Diagnosis and Therapy.” *Mater. Res. Soc. Symp. Proc.* 1019E. Copyright (C) 2011 American Chemical Society (ACS). All Rights Reserved. (2007): No pp. given, Paper #: 1019-FF02-04.
- Lavis, S et al. “In vitro echogenicity characterization of poly[lactide-coglycolide] (plga) microparticles and preliminary in vivo ultrasound enhancement study for ultrasound contrast agent application.” *Invest Radiol* 40.8 (2005): 536-544.
- Lee, In-Hyun et al. “Stable paclitaxel formulations in oily contrast medium.” *Journal of Controlled Release* 102.2 (2005): 415-425.
- Lewinski, N, V Colvin, and R Drezek. “Cytotoxicity of nanoparticles.” *Small* 4.1 (2008): 26-49.
- Li, C, and L H V Wang. “Photoacoustic tomography and sensing in biomedicine.” *Physics in Medicine and Biology* 54.19 (2009): R59.
- Li, P C, C W Wei, C K Liao, C D Chen, K C Pao, C R C Wang, Y N Wu, and D B Shieh. “Multiple targeting in photoacoustic imaging using bioconjugated gold nanorods.” Vol. 6086. 2006. 60860M. Print.
- Li, T, K Tachibana, and M Kuroki. “Gene transfer with echo-enhanced contrast agents: comparison between Albunex, Optison, and Levovist in mice--initial results.” *Radiology* 229.2 (2003): 423-428.
- Li, Ying Suet, Emma Davidson, et al. “Optimising ultrasound-mediated gene transfer (sonoporation) in vitro and prolonged expression of a transgene in vivo: Potential applications for gene therapy of cancer.” *Cancer Lett. (Shannon, Irel.)* 273. Copyright (C) 2011 American Chemical Society (ACS). All Rights Reserved. (2009): 62-69.

- Liggins, R T, and H M Burt. "Polyether-polyester diblock copolymers for the preparation of paclitaxel loaded polymeric micelle formulations." *Adv Drug Deliv Rev* 54.2 (2002): 191-202.
- Lo, A H et al. "Acoustic droplet vaporization threshold: effects of pulse duration and contrast agent." *IEEE Trans Ultrason Ferroelectr Freq Control* 54.5 (2007): 933-946.
- Loomis, Kristin, Kathleen McNeeley, and Ravi V Bellamkonda. "Nanoparticles with targeting, triggered release, and imaging functionality for cancer applications." *Soft Matter* 7.3 (2011): n. pag.
- Lopes de Menezes, Daniel E., Linda M. Pilarski, and Theresa M. Allen. "In Vitro and in Vivo Targeting of Immunoliposomal Doxorubicin to Human B-Cell Lymphoma." *Cancer Res.* 58.15 (1998): 3320-3330. Web. 26 Feb. 2012.
- Lu, Wei et al. "Photoacoustic imaging of living mouse brain vasculature using hollow gold nanospheres." *Biomaterials* 31.9 (2010): 2617-2626.
- Lundberg, B B. "Ether lipids enhance the cytotoxic effect of teniposide and paclitaxel in liposomes against leukaemic cells in culture." *Anticancer Drug Des* 12.6 (1997): 503-513.
- Lyamshev, L M. "Optoacoustic sources of sound." *SOV PHYS USPEKHI* 24.12 (1981): 977-995. Print.
- Madsen, E L et al. "Tissue mimicking materials for ultrasound phantoms." *Medical physics* 5.5 391-4. Web. 6 Jan. 2012.
- Maeda, H et al. "Tumor vascular permeability and the EPR effect in macromolecular therapeutics: a review." *J Control Release* 65.1-2 (2000): 271-284.
- Malam, Yogeshkumar, Marilena Loizidou, and Alexander M Seifalian. "Liposomes and nanoparticles: nanosized vehicles for drug delivery in cancer." *Trends Pharmacol. Sci.* 30. Copyright (C) 2011 American Chemical Society (ACS). All Rights Reserved. (2009): 592-599.
- Mallidi, S, T Larson, J Aaron, et al. "Molecular specific optoacoustic imaging with plasmonic nanoparticles." *Opt Express* 15.11 (2007): 6583-6588.
- Mallidi, S, T Larson, J Tam, et al. "Multiwavelength Photoacoustic Imaging and Plasmon Resonance Coupling of Gold Nanoparticles for Selective Detection of Cancer." *Nano Lett* (2009): n. pag.
- Matsumura, Y, and H Maeda. "A new concept for macromolecular therapeutics in cancer chemotherapy: mechanism of tumorotropic accumulation of proteins and the antitumor agent smancs." *Cancer Research* 46 (1986): 6387-6392. Print.
- "Medical Radiation Exposure Of The U.S. Population Greatly Increased Since The Early 1980s." Web. 13 Jan. 2012.

- Michnik, A. *Thermal stability of bovine serum albumin DSC study*. Vol. 71. Akadémiai Kiadó, co-published with Springer Science+Business Media B.V., Formerly Kluwer Academic Publishers B.V., 2003. Web. 5 Jan. 2012.
- Michnik, Anna, Katarzyna Michalik, and Zofia Drzazga. "Stability of bovine serum albumin at different pH." *Journal of Thermal Analysis and Calorimetry* 80.2 (2005): 399-406.
- Miele, Evelina et al. "Albumin-bound formulation of paclitaxel (Abraxane ABI-007) in the treatment of breast cancer." *International journal of nanomedicine* 4 (2009): 99-105. Web. 15 Feb. 2012.
- Miller, Douglas L., Sorin V. Pislaru, and James F. Greenleaf. *Sonoporation: Mechanical DNA Delivery by Ultrasonic Cavitation*. Vol. 27. Springer Netherlands, 2002. Web. 11 Feb. 2012.
- Mitragotri, Samir. "Healing sound: the use of ultrasound in drug delivery and other therapeutic applications." *Nature reviews. Drug discovery* 4.3 (2005): 255-60. Web. 11 Feb. 2012.
- Moes, C J et al. "Measurements and calculations of the energy fluence rate in a scattering and absorbing phantom at 633 nm." *Applied optics* 28.12 (1989): 2292-6. Web. 6 Jan. 2012.
- Mogensen, C. E. "The Glomerular Permeability Determined by Dextran Clearance Using Sephadex Gel Filtration." (2009): n. pag. Web. 27 Feb. 2012.
- Morawski, A M, G A Lanza, and S A Wickline. "Targeted contrast agents for magnetic resonance imaging and ultrasound." *Curr Opin Biotechnol* 16.1 (2005): 89-92.
- Mourad, Pierre D et al. "Ultrasound Accelerates Functional Recovery after Peripheral Nerve Damage." *Neurosurgery* 48.5 (2001): n. pag.
- Nam, Kweon-Ho et al. "Acoustic Droplet Vaporization, Cavitation, and Therapeutic Properties of Copolymer-Stabilized Perfluorocarbon Nanoemulsions." *AIP Conf. Proc.* 1113. Copyright (C) 2011 American Chemical Society (ACS). All Rights Reserved. (2009): 124-128.
- Nielsen, Torsten O, Forrest D Hsu, et al. "Immunohistochemical and clinical characterization of the basal-like subtype of invasive breast carcinoma." *Clinical cancer research : an official journal of the American Association for Cancer Research* 10.16 (2004): 5367-74. Web. 21 July 2011.
- Nielsen, Ulrik B, Dmitri B Kirpotin, et al. "Therapeutic efficacy of anti-ErbB2 immunoliposomes targeted by a phage antibody selected for cellular endocytosis." *Biochimica et Biophysica Acta (BBA) - Molecular Cell Research* 1591.1-3 (2002): 109-118. Web. 26 Feb. 2012.

- Nikoobakht, B, and M A El-Sayed. "Preparation and growth mechanism of gold nanorods (NRs) using seed-mediated growth method." *Chemistry of Materials* 15.10 (2003): 1957-1962. Print.
- Nikoobakht, Babak, and Mostafa A El-Sayed. "Preparation and Growth Mechanism of Gold Nanorods (NRs) Using Seed-Mediated Growth Method." *Chemistry of Materials* 15.10 (2003): 1957-1962.
- Nishihara, Masamichi, Kenji Imai, and Masayuki Yokoyama. "Preparation of perfluorocarbon/fluoroalkyl polymer nanodroplets for cancer-targeted ultrasound contrast agents." *Chem. Lett.* 38. Copyright (C) 2011 American Chemical Society (ACS). All Rights Reserved. (2009): 556-557.
- Oraevsky, A A, R O Esenaliev, et al. "Lateral and z-axial resolution in laser optoacoustic imaging with ultrasonic transducers." *Proc. SPIE*. Vol. 2389. 1995. 198-208. Print.
- Oraevsky, A A, S L Jacques, et al. "Time-Resolved Optoacoustic Imaging in Layered Biological Tissues." *Advances in Optical Imaging and Photon Migration*. Ed. Robert R Alfano. Vol. 21. New York: Academic Press, 1994. 161-165. Print.
- Oraevsky, A A, S L Jacques, and F K Tittel. "Determination of tissue optical properties by time-resolved detection of laser-induced stress waves." *Proc. SPIE*. Vol. 1882. 1993. 86-101. Print.
- Oraevsky, A A, A A Karabutov, and E V Savateeva. "Enhancement of optoacoustic tissue contrast with absorbing nanoparticles." *European Conference on Biomedical Optics, Proc. SPIE*. Vol. 4434. 2001. 60-69. Print.
- Oraevsky, AA, and AA Karabutov. "Optoacoustic tomography." 2003 : n. pag. Print.
- Owens III, Donald E, and Nicholas A Peppas. "Opsonization, biodistribution, and pharmacokinetics of polymeric nanoparticles." *International Journal of Pharmaceutics* 307.1 (2006): 93-102.
- Pan, Xing Q., Huaqing Wang, and Robert J. Lee. *Antitumor Activity of Folate Receptor-Targeted Liposomal Doxorubicin in a KB Oral Carcinoma Murine Xenograft Model*. Vol. 20. Springer Netherlands, 2003. Web. 26 Feb. 2012.
- Park, John W et al. "Anti-HER2 Immunoliposomes ." *Clinical Cancer Research* 8 .4 (2002): 1172-1181.
- Perkins, A C et al. "Human biodistribution of an ultrasound contrast agent (Quantison) by radiolabelling and gamma scintigraphy." *The British journal of radiology* 70.834 (1997): 603-11. Web. 3 Mar. 2012.
- Phillips, Margaret A, Martin L Gran, and Nicholas A Peppas. "Targeted nanodelivery of drugs and diagnostics." *Nano Today* 5.2 143-159.
- Pisani, E, N Tsapis, J Paris, V Nicolas, L Cattel, and E Fattal. "Polymeric Nano/Microcapsules of Liquid Perfluorocarbons for Ultrasonic Imaging: Physical

- Characterization.” *Langmuir* 22. Copyright (C) 2011 American Chemical Society (ACS). All Rights Reserved. (2006): 4397-4402.
- Pitsillides, C M et al. “Selective cell targeting with light-absorbing microparticles and nanoparticles.” *Biophys J* 84.6 (2003): 4023-4032.
- Plesset, M S, and A Prosperetti. “Bubble Dynamics and Cavitation.” *Annual Review of Fluid Mechanics* 9.1 (1977): 145-185.
- Porter, T R et al. “Targeted vascular delivery of antisense molecules using intravenous microbubbles.” *Cardiovasc Resusc Med* 7.1 (2006): 25-33.
- Prokop, Adrian F et al. “Polyacrylamide gel as an acoustic coupling medium for focused ultrasound therapy.” *Ultrasound in Medicine & Biology* 29.9 (2003): 1351-1358. Web. 6 Jan. 2012.
- Rapoport, N Y et al. “Microbubble Generation in Phase-Shift Nanoemulsions used as Anticancer Drug Carriers.” *Bubble Sci Eng Technol* 1.1-2 (2009): 31-39.
- Rapoport, Natalya, Zhonggao Gao, and Anne Kennedy. “Multifunctional nanoparticles for combining ultrasonic tumor imaging and targeted chemotherapy.” *J. Natl. Cancer Inst.* 99. Copyright (C) 2011 American Chemical Society (ACS). All Rights Reserved. (2007): 1095-1106.
- Rapoport, Natalya, and Zhonggao Gao. “Echogenic polymeric nanoparticles for tumor imaging and therapy.” *Polym. Prepr. (Am. Chem. Soc., Div. Polym. Chem.)* 47. Copyright (C) 2011 American Chemical Society (ACS). All Rights Reserved. (2006): 49-50. Print.
- Rayford, Cleveland Eugene, George Shuford, and G C Schatz. “Optical Properties of Gold Nanospheres.” *Nanoscape* 2.1 (2005): 27-33. Print.
- Razansky, Daniel et al. “Multispectral opto-acoustic tomography of deep-seated fluorescent proteins in vivo.” *Nat Photon* 3.7 (2009): 412-417.
- Roobottom, C A, G Mitchell, and G Morgan-Hughes. “Radiation-reduction strategies in cardiac computed tomographic angiography.” *Clinical Radiology* 65.11 (2010): 859-867.
- Rosen, Milton J. *Surfactants and Interfacial Phenomena*. John Wiley & Sons, Inc., 2004.
- Rowinsky, E K et al. “Clinical toxicities encountered with paclitaxel (Taxol).” *Seminars in oncology* 20.4 Suppl 3 (1993): 1-15.
- Rowinsky, E K, and R C Donehower. “Paclitaxel (taxol).” *N Engl J Med* 332.15 (1995): 1004-1014.
- Ryan, L K, and F S Foster. “Tissue equivalent vessel phantoms for intravascular ultrasound.” *Ultrasound in medicine & biology* 23.2 (1997): 261-73. Web. 6 Jan. 2012.

- Schnitzer, J E. "gp60 is an albumin-binding glycoprotein expressed by continuous endothelium involved in albumin transcytosis ." *American Journal of Physiology - Heart and Circulatory Physiology* 262 .1 (1992): H246-H254.
- Shah, J et al. "Photoacoustic imaging and temperature measurement for photothermal cancer therapy." *J Biomed Opt* 13.3 (2008): 34024.
- Sharma, R I et al. "Albumin-derived nanocarriers: substrates for enhanced cell adhesive ligand display and cell motility." *Biomaterials* 27.19 (2006): 3589-3598.
- Sheeran, Paul S et al. "Formulation and Acoustic Studies of a New Phase-Shift Agent for Diagnostic and Therapeutic Ultrasound." *Langmuir* 27. Copyright (C) 2011 American Chemical Society (ACS). All Rights Reserved. (2011): 10412-10420.
- Shive, M S, and J M Anderson. "Biodegradation and biocompatibility of PLA and PLGA microspheres." *Adv Drug Deliv Rev* 28.1 (1997): 5-24.
- Sigrist, Markus W. "Laser generation of acoustic waves in liquids and gases." *Journal of Applied Physics* 60.7 (1986): R83-R122.
- Slamon, D. et al. "Studies of the HER-2/neu proto-oncogene in human breast and ovarian cancer." *Science* 244.4905 (1989): 707-712. Web. 26 Feb. 2012.
- Soga, Osamu et al. "Thermosensitive and biodegradable polymeric micelles for paclitaxel delivery." *Journal of Controlled Release* 103.2 (2005): 341-353.
- Soman, N R et al. "New mechanisms for non-porative ultrasound stimulation of cargo delivery to cell cytosol with targeted perfluorocarbon nanoparticles." *Nanotechnology* 19. Copyright (C) 2011 American Chemical Society (ACS). All Rights Reserved. (2008): 185102/1-185102/7.
- Stephens, R B, G S Cieloszyk, and G L Salinger. "Thermal conductivity and specific heat of non-crystalline solids: Polystyrene and polymethyl methacrylate." *Physics Letters A* 38.3 (1972): 215-217.
- Straub, J A et al. "Porous PLGA microparticles: AI-700, an intravenously administered ultrasound contrast agent for use in echocardiography." *J Control Release* 108.1 (2005): 21-32.
- Stride, E P, and C C Coussios. "Cavitation and contrast: the use of bubbles in ultrasound imaging and therapy." *Proc Inst Mech Eng H* 224. Copyright (C) 2011 U.S. National Library of Medicine. (2010): 171-191. Print.
- Suzuki, Ryo et al. "Cancer gene therapy by IL-12 gene delivery using liposomal bubbles and tumoral ultrasound exposure." *J. Controlled Release* 142. Copyright (C) 2011 American Chemical Society (ACS). All Rights Reserved. (2010): 245-250.
- Ta, Terence et al. "Thermosensitive Liposomes Modified with Poly(N-isopropylacrylamide-co-propylacrylic acid) Copolymers for Triggered Release of

- Doxorubicin.” *Biomacromolecules* 11. Copyright (C) 2011 American Chemical Society (ACS). All Rights Reserved. (2010): 1915-1920.
- Tartis, Michaelann Shortencarier et al. “Therapeutic effects of paclitaxel-containing ultrasound contrast agents.” *Ultrasound Med Biol* 32. Copyright (C) 2011 U.S. National Library of Medicine. (2006): 1771-1780. Print.
- Textbook of human histology*. Jaypee Brothers, 2006.
- Thierry, B et al. “A robust procedure for the functionalization of gold nanorods and noble metal nanoparticles.” *Chem Commun (Camb)* 13 (2009): 1724-1726.
- Tiruppathi, C, A Finnegan, and A B Malik. “Isolation and characterization of a cell surface albumin-binding protein from vascular endothelial cells .” *Proceedings of the National Academy of Sciences* 93 .1 (1996): 250-254.
- Torchilin, Vladimir. “Tumor delivery of macromolecular drugs based on the EPR effect.” *Adv. Drug Delivery Rev.* 63. Copyright (C) 2011 American Chemical Society (ACS). All Rights Reserved. (2011): 131-135.
- Travis, James, and Ralph Pannell. “Selective removal of albumin from plasma by affinity chromatography.” *Clinica Chimica Acta* 49.1 (1973): 49-52. Web. 6 Mar. 2012.
- Tsai, Kun-Che et al. “Differences in gene expression between sonoporation in tumor and in muscle.” *J. Gene Med.* 11. Copyright (C) 2011 American Chemical Society (ACS). All Rights Reserved. (2009): 933-940.
- Unger, E C et al. “Gene delivery using ultrasound contrast agents.” *Echocardiography* 18.4 (2001): 355-361.
- Unger, Evan, and Terry O Matsunaga. “Lipid coated microbubbles and nanodroplets as tools for biomedical nanotechnology.” *Pan Stanford Ser. Biomed. Nanotechnol.* 1. Copyright (C) 2011 American Chemical Society (ACS). All Rights Reserved. (2011): 749-786. Print.
- Wall, Monroe E, and Mansukh C Wani. “Camptothecin and Taxol: Discovery to Clinic—Thirteenth Bruce F. Cain Memorial Award Lecture .” *Cancer Research* 55 .4 (1995): 753-760.
- Wang, Bo, E Yantsen, T Larson, et al. “Plasmonic intravascular photoacoustic imaging for detection of macrophages in atherosclerotic plaques.” *Nano Letters* 9.6 (2009): 2212–2217. Print.
- Wang, Lihong V., Hsin-I Wu, and Barry R. Masters. “Biomedical Optics, Principles and Imaging.” *Journal of Biomedical Optics* 2008 : 049902.
- Wang, Y W, X Y Xie, et al. “Photoacoustic tomography of a nanoshell contrast agent in the in vivo rat brain.” *Nano Letters* 4.9 (2004): 1689-1692.
- Wang, Y et al. “Photoacoustic Tomography of a Nanoshell Contrast Agent in the in Vivo Rat Brain.” *Nano Letters* 4.9 (2004): 1689-1692. Print.

- Waters, Emily A et al. "Detection of targeted perfluorocarbon nanoparticle binding using 19F diffusion weighted MR spectroscopy." *Magn. Reson. Med.* 60. Copyright (C) 2011 American Chemical Society (ACS). All Rights Reserved. (2008): 1232-1236.
- Wells, Dominic J. "Electroporation and ultrasound enhanced non-viral gene delivery in vitro and in vivo." *Cell Biol. Toxicol.* 26. Copyright (C) 2011 American Chemical Society (ACS). All Rights Reserved. (2010): 21-28.
- Wheatley, M A et al. "Comparison of in vitro and in vivo acoustic response of a novel 50:50 PLGA contrast agent." *Ultrasonics* 44.4 (2006): 360-367.
- Wickline, Samuel A. "Perfluorocarbon nanoemulsions for molecular imaging and therapy." American Chemical Society, 2007. FLUO-019. Print.
- Wickline, Samuel A, and Gregory M Lanza. "Molecular imaging, targeted therapeutics, and nanoscience." *Journal of cellular biochemistry. Supplement* 39 (2002): 90-7. Web. 6 Sept. 2011.
- Wickline, Samuel A, and Gregory M Lanza. "Nanotechnology for molecular imaging and targeted therapy." *Circulation* 107. Copyright (C) 2011 U.S. National Library of Medicine. (2003): 1092-1095. Print.
- Wilson, Katheryne, Kimberly Homan, and Stanislav Emelianov. "Biomedical photoacoustics beyond thermal expansion using triggered nanodroplet vaporization for contrast-enhanced imaging." *Nature Communications* 3 (2012): 618. Web. 10 Jan. 2012.
- Wilson, Katheryne, Kimberly Homan, and Stanislav Emelianov. "Photoacoustic and ultrasound imaging contrast enhancement using a dual contrast agent." *SPIE Photonics West*. Ed. A Oraevsky Alexander & V Wang Lihong. Vol. 7564. San Francisco, CA: SPIE, 2010. 75642P.
- Wilson, Katheryne, Kimberly Homan, and Stanislav Emelianov. "Synthesis of a dual contrast agent for ultrasound and photoacoustic imaging." *Photonics West*. Ed. Achilefu Samuel & Raghavachari Ramesh. Vol. 7576. San Francisco, CA: SPIE, 2010. 75760M.
- Winter, Patrick M et al. "Endothelial alpha(v)beta3 integrin-targeted fumagillin nanoparticles inhibit angiogenesis in atherosclerosis." *Arteriosclerosis, thrombosis, and vascular biology* 26.9 (2006): 2103-9. Web. 10 June 2011.
- Xiaohua, Huang, Neretina Svetlana, and A El-Sayed Mostafa. "Gold Nanorods: From Synthesis and Properties to Biological and Biomedical Applications." *Advanced Materials* 21.48 (2009): 4880-4910.
- Xie, Wenyue et al. "Ultrasound microbubbles enhance recombinant adeno-associated virus vector delivery to retinal ganglion cells in vivo." *Academic radiology* 17.10 (2010): 1242-8. Web. 1 Mar. 2012.

- Xu, Jeff S et al. "Synthesizing and binding dual-mode poly (lactic-co-glycolic acid) (PLGA) nanobubbles for cancer targeting and imaging." *Biomaterials* 31. Copyright (C) 2011 American Chemical Society (ACS). All Rights Reserved. (2010): 1716-1722.
- Xu, Minghua, and Lihong V Wang. "Photoacoustic imaging in biomedicine." *Review of Scientific Instruments* 77 (2006): 41101. Print.
- Yamamoto, Tadashi et al. "High Incidence of Amplification of the Epidermal Growth Factor Receptor Gene in Human Squamous Carcinoma Cell Lines." *Cancer Res.* 46.1 (1986): 414-416. Web. 11 Feb. 2012.
- Yang, X M, S E Skrabalak, et al. "Photoacoustic tomography of a rat cerebral cortex in vivo with au nanocages as an optical contrast agent." *Nano Letters* 7.12 (2007): 3798-3802.
- Yang, X, S E Skrabalak, et al. "Photoacoustic tomography of a rat cerebral cortex in vivo with Au nanocages as an optical contrast agent." *Nano Lett* 7.12 (2007): 3798-3802. Print.
- Yao, J et al. "Evans blue dye-enhanced capillary-resolution photoacoustic microscopy in vivo." *Journal of Biomedical Optics* 14.5 (2009): 54049.
- Yokoyama, Masayuki, and Masamichi Nishihara. "Perfluorocarbon emulsions and ultrasonic contrast agents containing the same." 2010 : 13pp. Print.
- Yoon, Chang S, and Jeong H Park. "Ultrasound-mediated gene delivery." *Expert Opin. Drug Delivery* 7. Copyright (C) 2011 American Chemical Society (ACS). All Rights Reserved. (2010): 321-330.
- Youtie, Jan, Philip Shapira, and Alan L. Porter. "Nanotechnology publications and citations by leading countries and blocs." *Journal of Nanoparticle Research* 10.6 (2008): 981-986. Web. 6 July 2011.
- Yuan, Fan et al. "Vascular Permeability in a Human Tumor Xenograft: Molecular Size Dependence and Cutoff Size." *Cancer Research* 55.17 (1995): 3752-3756.
- Zell, K et al. "Acoustical properties of selected tissue phantom materials for ultrasound imaging." *Physics in medicine and biology* 52.20 (2007): N475-84. Web. 6 Jan. 2012.
- Zhao, Z., Glod, S. & Poulidakos, D. Pressure and power generation during explosive vaporization on a thin-film microheater. *International Journal of Heat and Mass Transfer* 43, 281-296 (2000)
- Zhu, Jia-an et al. "Low-frequency and high-intensity ultrasonic may play a better role in Ultrasound Contrast Agent drug delivery system in vivo." *Med. Hypotheses* 73. Copyright (C) 2011 American Chemical Society (ACS). All Rights Reserved. (2009): 211-212.

Zou, X et al. "An approach for synthesizing nanometer-to micrometer-sized silver nanoplates." *Colloids and Surfaces A: Physicochemical and Engineering Aspects* 303.3 (2007): 226-234. Print.

## Vita

Katheryne (Katie) Wilson was born in 1986 in Tacoma, Washington to her parents, Beth and Dave. After attending Puyallup Senior High School ('04) in Puyallup, Washington, she went to The University of Washington in Seattle, Washington where she graduated in 2008 with a bachelor's of science in bioengineering. During her undergraduate education, Katie focused on development of tissue mimicking phantoms for ultrasound and HIFU therapy. Katie then attended The University of Texas at Austin where she received her master's degree in 2010. She continued with her project, the development of a dual contrast agent for combined ultrasound and photoacoustic imaging, as a doctoral student. The results of her work were presented in several peer-reviewed journals and conference proceedings, most notably including *Nature Communications*. During her graduate career, Katie received several fellowships and awards, including the World Molecular Imaging Society's Young Investigator Award in 2011 in San Diego, California. After her graduation, Katie will join Stanford University as a postdoctoral fellow to focus on research involving clinically translatable, molecular imaging.

Permanent email: [katheryne.wilson@gmail.com](mailto:katheryne.wilson@gmail.com)

This dissertation was typed by Katheryne Wilson.